Deformation of a face-centered cubic FeCoCrMnNi high entropy alloy

A Dissertation Presented for the

Doctor of Philosophy

Degree

The University of Tennessee, Knoxville

Chao Zhu

August 2014

Copyright @ 2014 by Chao Zhu

All rights reserved

Dedication

This dissertation is dedicated to my grandmother and my late grandfather. They brought me up with hard labor and unfailing love however unfavorable what the life has thrown to them. Their toughness in adversity has been inspiring me and will be for the rest of my life to be a just, upright human.

Acknowledgement

First and foremost, my gratitude goes wholeheartedly to my advisor, Dr. Nieh, for the opportunity to study under his guidance in this five-year life journey. He is kind, intelligent and a world-recognized professional diligent in renewing and expanding the expertise in this field many years as a day for what I have known. Without his devotional help and endless patience, this work along with any other accomplishment during my Ph. D study wouldn't be possible. Not only so, he also served as a mentor generously sharing his life stories and lessons. He is a sharp observer and a good communicator. I have been gaining from his full of wisdom and thought provoking life experience and had many moments of laughter along the way.

My gratitude also extends to Mrs. Nieh, amiable and edifying. She always encourages me and never fails to show her empathy during my hard times. It happened like yesterday that in the first semester upon my arrival in America, she and Dr. Nieh decided children's English-learning books are more appropriate for me to get started with and took the trouble themselves borrowing them for me. Today, this moment still touches me. They have given me too much I can pay back and cultivated me into an upright man with their integrity, which is essentially way more important than getting a degree.

I am also very thankful to my committee members. Thanks to Professor Gao for his insightful critique on my proposal and for his kind encouragements: "Don't view this as a burden but an opportunity to reflect on your work and sharpen your thinking." Thanks to Professor Penumadu for squeezing time out of the already tight schedule as the department head of civil and environmental engineering along with his valuable, incisive advice: " you are the toughest judge of yourself, not only so in your work but more in your life." Thanks to Professor Liaw for being patient and not minding me as a student every time I go over your calendar just to find a time fit for my defense."

My appreciation also goes to the MSE department where I spend most of the time. Firstly to the two department heads, the former head Professor Pharr and the current head Professor Kurt, for their efforts in advancing our department nationally and for their emphasis in teaching to have us graduate students well educated and prepared. Thanks to

the administration staff Ms. Carla, Ms. Susan and Ms. Martha for their numerous help. Thanks to the Professor George and Professor Ramki for having me as their TA which is a great learning experience and special thanks to Professor Ramki who kindly nominated me as the best teaching assistant for his class. Thanks to Professor Morris for fruitful academic discussions with him and his fun, beneficial class on thermodynamics.

Also special thanks go to Professor George for allowing me using his group facility in ORNL and Mr. Cecil's help with training. Thanks to Dr. An at ORNL for sincerely sharing his view on research and encouraging me who was then just getting my PhD started. Thanks to Professor Wang at ORNL to endorse me as a user in VULCAN beam line. Thanks to Professor Wang at Ag campus for granting me permission to use the nanoindenter at his lab on weekends and to Ms. Yujie and Dr. Omid in his group for their help. Assistance on experimental work from Ms Jifang Zeng and Professor Yang Yong at the City University of Hong Kong is also greatly appreciated.

I also want to thank my colleagues and friends very much who help to make my life here easier. Thanks to group members Drs. S.X. Song, C.L. Wang, L. Wang, and Mr. D. Wu for their numerous technical help and discussions. Thanks to my friends Mr. Qingming Feng, Mr. Zhenggang Wu, Mr. Yang Tong, Mr. Wei Guo and many others whose names are saved in my heart, your presence in my life is a delight. You are all remembered and appreciated.

Lastly but not the least, my tributes go to my family who have been supporting me financially and spiritually at every stage of my life.

Financial support for this work from the National Science Foundation under Contract DMR-0905979 is gratefully acknowledged. The Tennessee Agricultural Experiment Station and UT College of Engineering that jointly funded the Instrumentation for the nanoindentation work are also appreciated.

Abstract

A polycrystalline, face-centered cubic high entropy alloy (HEA) FeCoCrMnNi was investigated by nanoindentation and stress relaxation. A literature review on HEAs was presented in Chapter 1 and a description of methodology was followed in Chapter 2.

In Chapter 3, the nature of incipient plasticity was characterized with instrumented indentations over various loading rates and temperatures. The maximum shear stress for initiating the incipient plasticity attained the theoretical strength and was relatively insensitive to grain orientation. However, it strongly depended upon the temperature, indicating a thermally activated nucleation process. The estimated activation energy and volume signify that the nucleation is mediated by point defect.

Chapter 4 deals with the time dependence of the incipient plasticity. By holding the sample at a constant stress lower than that prompting instantaneous pop-in, pop-in is observed after a period of delay during which creep occurred. The creep suggested that the dislocation loop in equilibrium with the holding load expanded to the critical radius by vacancy-controlled dislocation climb due to the chemical potential gradient of the vacancy from beneath the stressed region to the free surface.

Chapter 5 discusses the size dependence of the pop-in. Six tip radii were selected to perform the nanoindentation: 50, 200, 233, 467, 638, 743 and 2013nm [nanometer]. At small tip radius, the pop-in size is linearly proportional. However, it disappeared with a 50nm tip and approached a constant when the tip radius exceeds 638nm. A model on the basis of the competition between image force and volume dependence on radius was proposed to explain these features.

Chapter 6 turns to mechanistic investigation of the global deformation using stress relaxation from 293 to 1073K [Kelvin]. The alloy retains work hardening capability up to 1073K and the stress reduction decreases with the increasing temperature. The activation volume increases from $12b^3$ [Burges Vector cubed] at 873K to $62b^3$ at 1073K and the activation enthalpy from 0.2eV [electronic volt] at 673K and 0.9eV at 1073K. These values plus the Portevin-Le Chatelier effect within the testing temperatures indicate that the impurity may play an important role during high-temperature deformation.

Table of Contents

1 Introduction 1

1.1 Alloy thermodynamics 2

1.2 Microstructure of HEAs 3

1.2.1 Morphology variation with thermo-mechanical treatment and composition ... 3

1.2.2 Recrystallization behavior 7

1.3 Mechanical properties of HEA 10

1.3.1 Hardness, specific strength, thermal stability 11

1.3.2 Mechanical properties of single FCC-phased FeCoCrMnNi 13

1.3.2.1 Grain size dependence 13

1.3.2.2 Deformation mechanism 15

1.4 Proposed research plan 17

2 Methodology 19

2.1 Introduction: nanoindentation for the study of incipient plasticity 19

2.2 Statistical model determining the activation volume and energy for the onset of plasticity 20

2.3 Phenomenological model to determine activation volume and energy for stress relaxation 22

2.4 Experimental facility 24

2.4.1 Nanoindenter 24

2.4.2 High temperature testing 26

3 Incipient plasticity and dislocation nucleation studied using nanoindentation technique 28

3.1 Sample preparation and microstructure characterization 28

3.2 Experimental results 29

3.2.1 Nanoindentation tests at room temperature 29
3.2.2 Nanoindentation tests at elevated temperatures 35
3.3 Analysis and modeling 38
3.3.1 Effect of surface oxide 38
3.3.2 Homogenous dislocation nucleation 39
3.3.3 Vacancy-mediated heterogeneous dislocation nucleation 42
3.4 Conclusion 44
4 Time Dependence of Incipient Plasticity 46
4.1 Introduction 46
4.2 Experimental setup for delayed incipient plasticity study 48
4.3 Results: P-h curve and waiting time distribution 50
4.4 Discussion 56
4.4.1 Origin of time dependence-transition state theory 56
4.4.2 Dislocation loop expansion under constant load in HEA 58
4.4.3 Expansion mode in single crystal Ni - burst with the assistance of thermal fluctuation 61
4.5 Conclusion 63
5 Effect of tip radius on pop-in size 65
5.1 Introduction and Experimental 65
5.2 Results: p-h curves at various tip radius 66
5.3 Discussion 69
5.3.1 Pop-in size linearly scaling with tip radius between 200-700nm 69
5.3.2 The vanish of pop-in at extremely small radius below 100nm 70
5.3.3 Pop-in size saturating for tip radius above 700nm 74
5.4 Conclusion 77

6 Deformation mechanism at elevated temperatures investigated using stress relaxation 78

6.1 Introduction and experimental setup 78

6.2 Activation volume and activation energy 79

6.3 Discussion and conlcusion 84

7 Future perspectives 86

References 88

Vita 93

List of Tables

Table 1 The microstructure and parameters δ, ΔH_{mix}, ΔS_{mix}, T_m and Ω for multi-component alloys reported in literature[28] 4

Table 2 Compositions of dendrite regions obtained by EDS analysis (in at. %)[35] 5

Table 3 Compositions of interdendrite regions obtained by EDS analysis (in at. %)[35].. 5

Table 4 Grain sizes of the FeCoCrMnNi samples annealed at 850, 900, 925 and 950 °C for different annealing times[14]..... 8

Table 5 Specifications of Triboindenter and Nano Indenter XP..... 26

Table 6 Comparison between statistically fitting constant a_1 as graphically shown in Figure 22 and a_2 obtained from individual fitting as shown in Figure 21(b) for 11 different grains..... 33

Table 7 Incubation time (s) for (a) load at 320 μN at RT and (b) load at 280μN..... 53

Table 8 Incubation time (s) at 50˚C for (a) load at 300 μN, (b) for load at 275 μN, (c) for load at 250 μN and (d) for load at 225 μN 53

Table 9 Incubation time (s) at 100˚C for (a) load at 275 μN (b) load at 250 μN and (c) load at 225 μN 54

List of Figures

Figure 1The relationship between parameters δ, Ω and possible structures for multi-component alloys ("Solid Solutions" indicates the alloy contains only solid solution; "Intermetallics" indicates the alloy mainly contains intermetallic compound and other ordered phases; "S + I" indicates the solid solution with ordered compounds precipitated within; and "BMGs" indicates the alloy can form amorphous phase)[28] 2

Figure 2 Schematic representation of phase segregation observed during solidification of AlCoCrCuFeNi HEA by two different processing conditions: splat quenching (cooling rate 10^6-10^7 K s^{-1}) and casting (cooling rate 10-20 K s^{-1})[21] 4

Figure 3 X-ray analysis of samples in four different states[35]..... 4

Figure 4 Microstructures in the (a) as-cast, (b) as-forged, (c) as-homogenized-WQ, and (d) as-homogenized-FC states. Dendritic morphology is persistent under all conditions[35]..... 5

Figure 5 X-ray diffraction patterns of the six alloys investigated in the present study after three-day anneals at 1123 K (spectrum b) and 1273 K [30]..... 6

Figure 6 Backscatter electron micrographs of the annealed microstructures of the six multi-component alloys investigated: (a) CoCrFeMnNi; (b) CoCrFeMnCu; (c) CoMoFeMnCu; (d)TiCrFeMnNi; (e)CoVFeMnNi; and (f) CoCrVMnNi. The small, dispersed dark spots in (a) are oxide particles (containing mainly Cr and Mn) resulting from trace levels of oxygen present in the raw materials and possibly also from contamination during arc melting[30] 7

Figure 7 Microstructures of the FeCoNiCrMn alloy specimens annealed at 850 °C (A–C) and 925 °C (D–F). The annealing time periods were 1 h for (A) and (D), 2 h for (B) and (E), 6 h for (C) and 3.5 h for (F)[14] 9

Figure 8 Grain size as a function of the annealing time for the FeCoNiCrMn alloy specimens heat treated at 850, 900, 925 and 950 °C. A linear relation between the cube of the grain size and time is observed[14] 10

Figure 9 Wide range of hardness for HEAs, compared with 17-4 PH stainless steel, Hastelloy, and 316 stainless steel [7] 11

Figure 10 Yield strength σ_y versus density ρ. HEAs (dark dashed circle) compared with other materials, particularly structural alloys. Grey dashed contours (arrow indication) label the specific strength, σ_y/ρ from low (right bottom) to high (left top). HEAs are among the materials with highest strength and specific strength [7]..... 12

Figure 11 Temperature dependence of yield strength of NbMoTaW, VNbMoTaW, Inconel 718, and Haynes 230 alloys[49] 13

Figure 12 Hardness as a function of grain size in the FeCoNiCrMn alloy[14] 14

Figure 13 Temperature and grain size dependence of 0.2% offset yield stress[12] 14

Figure 14 Representative TEM BF micrographs from the gauge sections of interrupted tensile test specimens of the coarse-grained CoCrFeMnNi alloy (grain size 155 μm) after relatively small tensile strains: (a) 1.7% at 873 K, (b) 2.4% at 77 K and (c) 2.1% at 293 K pile up is clearly seen in all three temperatures[12] 15

Figure 15 Representative engineering stress–strain curves of the CoCrFeMnNi alloy at the six testing temperatures for the (a) fine-grained (grain size 4.4 μm) and (b) coarse-grained (grain size 155 μm) materials. The inset in (a) shows a small load drop after yielding for a fine-grained sample that was tested at 473 K[12] 16

Figure 16 TEM micrographs characterizing deformation twinning in the fine-grained CoCrFeMnNi alloy (grain size 4.4 μm) after a strain of 20.2% at 77 K. (a) Overview of the twinned microstructure acquired in the HAADF mode. (b) High-resolution TEM image of twins denoted “1” and “2”, with the

corresponding FFT inset. (c) FFT-filtered image of the area outlined by the white square in (b) showing the corresponding twinning elements. The inset in the lower left corner of (c) shows the fully indexed intensity maxima in reciprocal space[12]..... 16

Figure 17 The Triboindenter system..... 25

Figure 18 The detailed image for the testing workspace 25

Figure 19 (a) schematic illustration of the stress relaxation testing system for high temperatures and (b) the back view of the furnace in (a) which has three thermal couples connected and (c) the temperature controller and monitor that controls the designated temperature and receives another end of the three thermal couples to monitor the furnace temperature 27

Figure 20 (a) Optical microstructure of the annealed FeCoCrNiMn sample with an average grain size about 30~50μm and (b) XRD pattern indicates a single FCC structure. 28

Figure 21 (a) Typical load-displacement (*P-h*) curves from 3 different grains. Curves are offset from the origin for clear viewing. The pop-in events are marked by the black arrows and (b) Hertzian fitting by equation (3.1)for one of *P-h* curves from (a) yields a fitting coefficient 3.65 and a reduced modulus of 179GPa. ... 31

Figure 22 Statistics of 120 $P\text{-}h^{3/2}$ pairs at pop-in. The fitting yields a fitting coefficient 3.70 and a reduced modulus of 182GPa. 32

Figure 23 (a) The plot of cumulative probability of pop-in versus normalized shear stress shows that the shear stress for onset of yielding is in the range of 1/14~1/11μ, where μ is the shear modulus of the sample, and (b) A similar plot for all grains shows little difference and the normalized shear stress ranges within 1/15~1/10μ. 34

Figure 24 Extracting the activation volume from experimental data using equation(3.5). Experimental data are obtained from 120 datum points for each loading rate at 22˚C. The solid lines in red are the best linear fits. 36

Figure 25(a) Typical *P-h* curves at temperatures of 22, 50, 100 and 150˚C. The average load at pop-in drops nearly one third as the temperature increases from 22 to 150˚C, and (b) Hertzian fitting curves for the four temperatures are shown. 37

Figure 26 Graphical demonstration of equation (3.7) to extract the activation enthalpy for the pop-in. The three fitted lines converged at T=0K to a common y intercept ($0.101\pm0.001N^{1/3}$), which is scaled with enthalpy *H* via equation(3.7) 38

Figure 27 The variation of maximum shear stress versus temperature, giving an intercept with vertical axis at 8GPa (extrapolation), which is the strength of the alloy at 0K at the onset of plasticity. 41

Figure 28 Time dependence of pop-in during indentation on single crystal Ni_3Al. The holding time prior to pop-in decreases with increasing loading, until above 600 μN pop-in occurred spontaneously. At the largest holding load, i.e. 700 μN in this figure, pop-in occurs spontaneously before reaching the holding load. (Error bars show the scatter of typically five measurements.)[98] 47

Figure 29 The mean values of the waiting time before pop-in as a function of applied constant load in single crystal Fe-3%Si. After 600 s at a constant load of 125 mN, no pop-in occurred[111] 48

Figure 30 Schematic illustration of loading function in studying the delayed plasticity.. 49

Figure 31 Load-depth profile for RT at holding load (a) 320μN, (b) 280μN (c) 240μN . 50

Figure 32 Load-depth profile for 50˚C at holding load (a) 300μN, (b) 275 μN, (c) 250 μN (d) 200 μN 51

Figure 33 Load-depth profile for 100˚C at holding load (a) 275μN, (b) 250 μN (c) 225 μN and (d) 175 μN 52

Figure 34 The waiting time histogram for those present with delayed pop-in at holding load (a) 125μN, (b) 150μN, (c) 175uN and (d) load 175uN 55

Figure 35 Natural logarithmic of incubation time versus $P^{1/3}$ according to equation(4.5). The slope can be used to calculate the activation volume which can be further compared to that derived at Chapter 3..... 57

Figure 36 Equi-chemical potential contours (dotted lines). Diffusional flow occurs perpendicular to these contours (solid lines)[114] 59

Figure 37(a) Load depth profile under elastic load at RT, and (b) the corresponding load-time relation..... 61

Figure 38 Displacement as a function of time in the stage as indicated by the black circle in Figure 37a prior to pop-in. stepwise proceeding is indicative of the random walk of vacancy motion..... 61

Figure 39 Load-displacement curves for single crystal Ni during holding. No trace of creep was observed after holding began..... 62

Figure 40 The histogram of waiting time for Ni at RT, which is similar to the pattern observed in FeCoCrMnNi 62

Figure 41 Load depth profile for a pop-in occurring after 25s delay. No creep is observed before pop-in 63

Figure 42 Representative load-displacement curves at (a) R=200nm, (b). R=233nm, (c) R=467nm, (d) R=638nm, (e) R=743nm and (f) R=2013nm 67

Figure 43 The pop-in size shows two different trending as indicated by Region I and Region II. In Region I, the size increases linearly with tip radius, while in Region II, the size approaches a plateau. 68

Figure 44 the indentation response under a sharp tip with a nominal radius of 50nm 69

Figure 45 Schematic illustration of the size of the highly stress zone (~90% τ_{max}) for the 50nm tip, which is smaller than the critical radius, r_c(~6b=15nm), corresponding to the maximum shear stress..... 72

Figure 46 Maximum shear stress (τ_{max}) contours of equal stress for spherical indenter calculated for Poisson's ratio v = 0.26. Distances r and z normalized to the contact radius, a, and stress expressed in terms of the mean contact pressure p_m[143]..... 73

Figure 47(a) The impression of micro-hardness testing for HEA at (a) magnification 100 and (b) magnification 400. The V shape slip bands are clearly seen in both micrographs 74

Figure 48the graphical illustration of comparison between two competing length scales- the working distance of image force versus the nucleating volume proportional to the tip radius 76

Figure 49 The microstructure annealed at 900C for 2hrs revealed a homogenous and equiaxed structure with grain size around 60μm..... 79

Figure 50 An overview of stress relaxation at different stages of plastic deformation over tested temperatures. The stress reduction increased with temperature and decreased with plastic deformation 80

Figure 51 Percentage of reduction in stress as a function of time for 600, 700 and 800˚C 81

Figure 52 ln(-dσ/dt) versus stress σ plot for the first cycle of relaxation curves at 600, 700 and 800˚C. The excellent linear fits evidenced the logarithmic nature of the relaxation curves. And the increasing fitted slopes also indicate by equation (6.5) an increasing activation volume with rising temperature..... 83

1 Introduction

Symbolizing a new strategy of alloy design, high entropy alloys (HEAs), consisting of multiple equimolar metallic elements in contrast to those developed from conventional strategy which are based on one or two main elements, are attracting much attention worldwide[1-11]. It was first referred by Cantor[1] as multi-component alloys and then defined by Yeh[5, 6] as "HEAs" based on the hypothesis that the contribution of enormously high configurational entropy of alloys with multiple elements would overwhelm the enthalpies of compound formation and thus thermodynamically favors a simple solid solution instead of intermetallics as expected from physical metallurgy intuition by reducing the Gibbs free energy dramatically. Due to the high configurational entropy, the multiple-component alloys have been given the name-high entropy alloys.

As a new class of alloys, HEAs call for new knowledge to understanding them. As nicely put by Cantor[1]: "Conventional alloy development strategy leads to an enormous amount of knowledge about alloys based on one component, but to very little or no knowledge about alloys containing several main components in approximately equal proportions. Theories for the occurrence, structure and properties of crystalline phases are similarly restricted to alloys based on one or two main components. Information and understanding is highly developed about alloys close to the apexes and edges of the phase diagram, with much less known about alloys in the centre of the diagram. This imbalance becomes rapidly much more pronounced as the number of components increases. For quaternary, quinary and higher order systems, information about alloys in the centre of the phase diagram is virtually non-existent. Since most of the possible alloy compositions are based on more than one component, it is clear that conventional alloy development strategy has been very restrictive in exploring the full range of possible alloys." The exciting statement about the multicompent system as a breakthrough over tradition draws the material community with enthusiasm in decoding HEAs and is also a main motivation for us to engage with this study.

To make simple solid solution HEAs, two general principles should be obeyed as a rule. On the one hand, the elements selected are usually those closely located in the

periodic table as they are similar in electronegativity, atomic radius, and etc. The selection ensures two purposes: to minimize the probability to form ordering compound and to be in accord with Hume-Rothery rules. On the other hand, to leverage the high entropy effect, five or more elements in equiatomic percentage have to be present. These principles explain why HEAs reported in literature are composed in such a way as FeCoCrMnNi[12-16], AlFeCoCrCuNi[17-23], to name a few.

Unlike traditional solid solutions, HEAs are very special. Firstly, considering there are many metallic elements in the periodic table, the theoretical HEA combinations are huge. They enrich current material varieties greatly and provide us enormous potentials to meet the ever-increasing need for materials with high performance. Secondly, HEA solid solutions are uncommon with traditional ones because there is not a predominant element in HEA serving as solute. Each species can be taken as "solute". Thirdly, the dislocation line, normally composed of the same kind atom, needs re-evaluation in HEAs that consists of multiple principal elements. These characteristics make this new alloy an interesting, intelligent topic to study. In what follows we offer a literature review for HEAs from the perspective of alloy thermodynamics, microstructure, mechanical properties and other miscellaneous properties.

1.1 Alloy thermodynamics

In this part, a detailed theoretical understanding of the underlying thermodynamic principles is laid out as to why HEAs tend to form simple solid solution instead of intermetallic compounds or amorphous alloys.

When an alloy is solidified, the equilibrium solid state (be it solid solution, intermetallic or amorphous) will be the one that has the maximum Gibbs free energy change, ΔG, from the liquid to solid. For a multi-component system, it is hard to calculate ΔG directly. However, the ΔG was assumed to be proportional to Gibbs free energy of mixing, ΔG_{mix}, which has been proven to be a good indicator in predicting the formability of bulk metallic glasses (BMGs), another multi-component system. To study the thermodynamics, HEAs are treated the same way.

The free energy of mixing ΔG_{mix} is defined as:

$$\Delta G_{mix} = \Delta H_{mix} - T\Delta S_{mix} \tag{1.1}$$

where ΔH_{mix} is mixing enthalpy, ΔS_{mix} is the configuration entropy of randomly mixing N elements. The ΔS_{mix} is defined by the following equation:

$$\Delta S_{mix} = -R\sum_{i=1}^{N} x_i \ln x_i \tag{1.2}$$

where R is the gas constant, x_i is the mole fraction of element i in the alloy system and $\sum_{i=1}^{N} x_i = 1$. ΔS_{mix} attains the maximum when each element has equal molar fraction as is the case in most HEAs[5]. So equation(1.2) is rewritten as:

$$\Delta S_{mix} = R\ln N \tag{1.3}$$

As can be seen, ΔS_{mix} increases rapidly with N. For example, ΔS for equimolar alloys with *3, 5, 6, 9* and *13* elements are *1.10R, 1.61R, 1.79R, 2.20R* and *2.57R*, respectively, whereas the entropy change associated with fusion of most metals is only around R. This tremendous ΔS_{mix} will be dominating the direction of ΔG_{mix} as temperature rises. Actually, the mixing temperature is at least at the melting point, T_m. So equation (1.1) should be rewritten as:

$$\Delta G_{mix} = \Delta H_{mix} - T_m\Delta S_{mix} \tag{1.4}$$

Although the absolute value of ΔH_{mix} is on the order of KJ/mol, the product $T_m\Delta S_{mix}$ can be even larger.

There are quite a few sophisticated models [24-29] taking into more parameters into account than ΔH_{mix} $T_m\Delta S_{mix}$ in predicting the formability of solid solution for multi-component systems. As in one proposed by Zhang *et al*[28, 29], they defined two terms, Ω as the ratio of $T_m\Delta S_{mix}$ to $|\Delta H_{mix}|$ representing the competitive nature between enthalpy and entropy, and δ the atomic size difference between elements which is defined as:

$$\delta = \sqrt{\sum_{i=1}^{N} c_i r_i (1 - \frac{r_i}{\bar{r}})^2} \tag{1.5}$$

where c_i and r_i are the concentration and atomic radius of ith element, and $\overline{r} = \sum_{i=1}^{N} c_i r_i$ is the average radius. By examining more than one hundred multi-component alloys (as listed in Table 1) reported in the literature, they summarized the finding in Figure 1 and proposed that when $\Omega \geq 1.1$ and $\delta \leq 6.6\%$, multi-component systems would form solid solution.

Table 1 The microstructure and parameters δ, ΔH_{mix}, ΔS_{mix}, T_m and Ω for multi-component alloys reported in literature[28]

Alloys	Structure	δ (%)	$\Delta Hmix$(kJ mol^{-1})	$\Delta Smix$ (J K^{-1} mol^{-1})	Tm (K)	Ω
CoCrFeNiAl	BCC	5.25	−12.32	13.38	1675.10	1.83
CoCrFeNiCu	FCC	1.07	3.20	13.38	1760.00	7.36
$CoCrFeNiCuAl_{0.3}$	FCC	3.15	1.56	14.43	1713.22	15.85
$CoCrFeNiCuAl_{0.5}$	FCC	3.82	−1.52	14.70	1684.86	16.29
$CoCrFeNiCuAl_{0.8}$	BCC + FCC	4.49	−3.61	14.87	1646.00	6.78
CoCrFeNiCuAl	BCC + FCC	4.82	−4.78	14.90	1622.25	5.06
$CoCrFeNiCuAl_{1.3}$	BCC + FCC	5.19	−6.24	14.85	1589.45	3.78
$CoCrFeNiCuAl_{1.5}$	BCC + FCC	5.38	−7.04	14.78	1569.27	3.30
$CoCrFeNiCuAl_{1.8}$	BCC + FCC	5.54	−8.08	14.65	1541.22	2.79
$CoCrFeNiCuAl_2$	BCC + FCC	5.71	−8.65	14.53	1523.86	2.56
$CoCrFeNiCuAl_{2.3}$	BCC	5.84	−9.38	14.35	1499.60	2.29
$CoCrFeNiCuAl_{2.5}$	BCC	5.91	−9.78	14.21	1484.50	2.15
$CoCrFeNiCuAl_{2.8}$	BCC	5.99	−10.28	14.01	1463.31	1.99
$CoCrFeNiCuAl_3$	BCC	6.09	−10.56	13.86	1450.06	1.90
CoCrFeNiCuAlSi	BCC + FCC	4.51	−18.86	16.18	1631.50	1.40
MnCrFeNiCuAl	BCC	4.73	−5.11	14.90	1580.58	4.62
CoCrFeNiMnGe	BCC + FCC	3.25	−15.17	14.90	1695.50	1.67
CoCrFeNiMn	FCC	0.92	−4.16	13.38	1792.40	5.77
CoCrFeNiMnCu	FCC	0.99	1.44	14.90	1720.00	17.80
$CoCrNiCu_{0.5}Al$	BCC	5.74	−10.17	13.15	1609.67	2.08
TiCoCrFeNiCuAlV	BCC + FCC	5.87	−13.94	17.29	1735.19	2.15
$CoCrFeNiCu_{0.5}$	FCC	1.06	0.49	13.15	1804.67	48.44
CoCrNiCuAl	BCC + FCC	5.19	−6.56	13.38	1584.50	3.23
CoCuNiAl	BCC + FCC	5.77	−8.00	11.52	1447.40	2.08
CuNiAl	BCC + FCC	6.20	−8.44	9.13	1339.80	1.45
CuNi	FCC	1.63	4.00	5.76	1543.00	2.22
$Co_{0.5}CrFeNiCuAl$	BCC + FCC	4.91	−4.50	14.70	1608.82	5.26
$CoCr_{0.5}FeNiCuAl$	BCC + FCC	5.02	−5.02	14.70	1572.82	4.61
$CoCrFe_{0.5}NiCuAl$	BCC + FCC	5.00	−5.55	14.70	1605.09	4.25
$CoCrFeNi_{0.5}CuAl$	BCC + FCC	4.91	−3.90	14.70	1612.64	6.08
$CoCrFeNiCu_{0.5}Al$	BCC	5.02	−7.93	14.70	1646.27	3.05
$Ti_{0.5}CoCrFeNiCu$	FCC	4.46	−3.70	14.70	1776.91	7.05
$Ti_{0.5}CoCrFeNiAl$	BCC1 + BCC2	6.11	−17.92	14.70	1699.73	1.39
TiCoCrFeNiAl	BCC1 + BCC2	6.58	−21.56	14.90	1720.25	1.19

Table 1. Continued

Alloys	Structure	δ (%)	$\Delta Hmix$(kJ mol^{-1})	$\Delta Smix$ (J K^{-1} mol^{-1})	Tm (K)	Ω
$Al_{11.1}(TiCoCrFeNiCuVMn)_{88.9}$	BCC + FCC	5.75	−12.74	18.27	1711.28	2.45
$Al_{20}(TiCoCrFeNiCuVMn)_{80}$	BCC	6.01	−15.44	17.99	1633.50	1.91
$TiCr_{0.5}FeNiCuAl$	BCC + FCC	6.45	−15.40	14.70	1640.55	1.56
TiCrFeNiCuAl	BCC + FCC	6.29	−13.67	14.90	1681.58	1.83
$TiCr_{1.5}FeNiCuAl$	BCC + FCC	6.14	−12.26	14.78	1716.31	2.08
$TiCr_2FeNiCuAl$	BCC + FCC	5.99	−11.10	14.53	1746.07	2.29
$TiCr_3FeNiCuAl$	BCC + FCC	5.72	−9.31	13.86	1794.44	2.67
TiCoCrFeNiCuAl	BCC1 + BCC2 + FCC	6.23	−13.80	16.18	1668.50	1.95
CoCrFeNiCuAlV	BCC + FCC	4.69	−7.76	16.18	1705.07	3.56
$Ti_{0.5}Co_{1.5}CrFeNiAl$	BCC + FCC	6.02	−17.17	14.54	1705.58	1.45
$Ti_{0.5}Co_2CrFeNiAl$	BCC + FCC	5.91	−16.43	14.23	1710.54	1.49
$Ti_{0.5}Co_3CrFeNiAl$	BCC + FCC	5.69	−14.93	13.49	1718.47	1.55
$Ti_{0.5}CoCrFeNiCu_{0.75}Al_{0.25}$	FCC	5.03	−7.28	15.55	1757.61	3.76
$Ti_{0.5}CoCeFeNiCu_{0.5}Al_{0.5}$	BCC + FCC	5.25	−10.84	15.75	1738.32	2.52
$Ti_{0.5}CoCrFeNiCu_{0.25}Al_{0.75}$	BCC1 + BCC2	5.83	−15.26	15.55	1719.02	1.75
$CoCrFeNiCu_{0.25}Al$	BCC	5.13	−9.94	14.34	1660.00	2.39
CoFeNiCuV	FCC	2.63	−1.78	14.90	1833.67	15.35
$CoCrFeNiCu_{0.75}Al_{0.25}$	FCC	3.00	−0.71	14.32	1738.78	35.07
$CoCrFeNiCu_{0.5}Al_{0.5}$	FCC	4.00	−4.60	14.54	1717.55	5.43
$CoCrFeNiCu_{0.25}Al_{0.75}$	BCC + FCC	4.71	−8.47	14.32	1696.33	2.87
$Ti_{0.5}CoCrFeNiCu_{0.25}Al$	BCC1 + BCC2	6.01	−15.50	15.54	1684.87	1.68
$Ti_{0.5}CoCrFeNiCu_{0.5}Al$	BCC1 + BCC2	5.90	−13.42	15.86	1671.25	1.97
CoCrFeNi	FCC	1.06	−3.75	11.53	1860.50	5.71
$CoCrFeNiAl_{0.25}$	FCC	3.25	−6.75	12.71	1805.97	3.40
$CoCrFeNiAl_{0.375}$	FCC	3.80	−7.99	12.97	1781.04	2.89
$CoCrFeNiAl_{0.5}$	BCC + FCC	4.22	−9.09	13.15	1757.50	2.55
$CoCrFeNiAl_{0.75}$	BCC + FCC	4.83	−10.90	13.33	1714.13	2.09
$CoCrFeNiAl_{0.875}$	BCC + FCC	5.06	−11.66	13.37	1694.12	1.95
$CoCrFeNiAl_{1.25}$	BCC	5.55	−13.42	13.34	1639.79	1.62
$CoCrFeNiAl_{1.5}$	BCC	5.77	−14.28	13.25	1607.68	1.50
$CoCrFeNiAl_2$	BCC	6.04	−15.44	12.98	1551.50	1.30
$CoCrFeNiAl_{2.5}$	BCC	6.19	−16.09	12.63	1503.96	1.17
$CoCrFeNiAl_3$	BCC	6.26	−16.41	12.26	1463.21	1.10
$MnCrFe_{1.5}Ni_{0.5}Al_{0.3}$	BCC	3.32	−5.51	12.31	1747.34	3.90
$MnCrFe_{1.5}Ni_{0.5}Al_{0.5}$	BCC	4.03	−6.77	12.67	1711.17	3.20
MoCrFeNiCu	FCC	2.92	4.64	13.38	1985.00	5.72
$Ti_{0.5}Co_{1.5}CrFeNi_{1.5}$	FCC	4.60	−10.74	12.86	1848.00	2.22
$Ti_{0.5}Co_{1.5}CrFeNi_{1.5}Mo_{0.1}$	FCC	4.72	−10.64	13.38	1866.70	2.35
$CoCrFeNiCuAl_{0.5}V_{0.2}$	FCC	3.87	−2.50	15.44	1703.01	10.52
$CoCrFeNiCuAl_{0.5}V_{0.4}$	BCC + FCC	3.80	−3.34	15.76	1719.92	8.12
$CoCrFeNiCuAl_{0.5}V_{1.2}$	BCC + FCC	3.99	−5.73	15.98	1777.49	4.96
$CoCrFeNiCuAl_{0.5}V_{1.4}$	BCC + FCC	4.00	−6.14	15.91	1789.79	4.64
$CoCrFeNiCuAl_{0.5}V_{1.6}$	BCC + FCC	4.00	−6.50	15.82	1801.40	4.38
$CoCrFeNiCuAl_{0.5}V_{1.8}$	BCC + FCC	4.00	−6.81	15.72	1812.38	4.19
$CoCrFeNiCuAl_{0.5}V_2$	BCC + FCC	3.99	−7.08	15.60	1822.77	4.01
MnCrFeNiCu	BCC + FCC	0.92	2.72	13.38	1710.00	8.41
$Mn_2CrFeNi_2Cu$	FCC	0.99	0.44	12.98	1713.00	50.53
$MnCr_2Fe_2NiCu$	BCC + FCC	0.84	2.61	12.89	1784.86	8.82
$Mn_2Cr_2Fe_2Ni_2Cu$	FCC	0.91	0.10	13.14	1749.11	229.8
$Mn_2CrFe_2NiCu_2$	BCC + FCC	0.83	4.69	12.97	1654.88	4.58
$MnCrFe_2Ni_2Cu_2$	FCC	0.95	3.88	12.97	1680.88	5.61

Table 1. Continued

Alloys	Structure	δ (%)	$\Delta Hmix$(kJ mol^{-1})	$\Delta Smix$ (J K^{-1} mol^{-1})	Tm (K)	Ω
$Mn_2Cr_2FeNi_2Cu_2$	BCC + FCC	0.97	2.37	13.14	1697.00	9.40
$MnCr_2Fe_2Ni_2Cu_2$	BCC + FCC	0.94	3.56	13.14	1729.33	6.38
$W_{27.3}Nb_{22.7}Mo_{25.6}Ta_{24.4}$	BCC	2.27	−6.49	11.50	3177.60	5.62
$W_{21.1}Nb_{20.6}Mo_{21.7}Ta_{15.6}V_{21}$	BCC	3.18	−4.54	13.33	2950.49	8.67
$Ti_{0.3}CoCrFeNi$	FCC + HCP	4.06	−8.89	12.83	1866.47	2.69
$Ti_{0.1}CoCrFeNiAl_{0.3}$	FCC	4.06	−8.93	13.47	1799.24	2.72
TiCoNiCuAlZn	BCC	6.43	−17.89	14.90	1680.12	1.39
$CoCrFeNiMo_{0.3}$	FCC	2.92	−4.15	12.83	1932.67	5.97
$CoCrFeNiAl_{0.3}Mo_{0.1}$	FCC	3.74	−7.26	13.44	1820.81	3.37
$CoCrFeNiCuAlMo_{0.2}$	BCC + FCC	4.95	−4.47	15.60	1633.31	5.70
$Ti_{0.8}CoCrFeNiCu$	FCC + Laves phase	5.26	−6.75	14.89	1785.66	3.95
TiCoCrFeNiCu	FCC + Laves phase	5.65	−8.44	14.90	1791.00	3.17
$Ti_{1.5}CoCrFeNiAl$	BCC1 + BCC2 + Laves phase	6.93	−23.91	14.78	1737.62	1.08
CoCrFeNiCuAlMn	BCC + FCC + unknow n phase	4.57	−5.63	16.18	1607.64	4.61
CrFeNiCuZr	BCC + compounds	9.91	−14.40	13.38	1831.60	1.70
$Ti_{0.5}Co_{1.5}CrFeNi_{1.5}Mo_{0.5}$	FCC + σ phase	5.09	−10.25	14.17	1935.25	2.67
$Ti_{0.5}Co_{1.5}CrFeNi_{1.5}Mo_{0.8}$	FCC + σ phase	5.28	−9.96	14.21	1980.95	2.83
TiCoCrNiCuAl	BCC + Cu + Cr	6.50	−16.67	14.58	1644.75	1.43
$CoCrFeNiCuAl_{0.5}V_{0.6}$	BCC + FCC + σ phase	3.94	−4.07	15.92	1735.73	6.79
$CoCrFeNiCuAl_{0.5}V_{0.8}$	BCC + FCC + σ phase	3.97	−4.71	16.00	1750.53	5.95
$CoCrFeNiCuAl_{0.5}V$	BCC + FCC + σ phase	3.98	−5.25	16.01	1764.42	5.38
$CoCrFeNiCuAl_{0.5}B_{0.2}$	FCC + boride	5.77	−4.00	15.44	1708.73	6.60
$CoCrFeNiCuAl_{0.5}B_{0.6}$	FCC + boride	8.07	−8.01	15.92	1751.76	3.48
$CoCrFeNiCuAl_{0.5}B$	FCC + ordered FCC + boride	9.52	−11.03	16.01	1789.50	2.60
TiCoCrFeNiCuVMn	FCC + BCC + σ phase + unknown phase	5.19	−8.13	17.29	1808.50	3.85
$Al_{40}(TiCoCrFeNiCuVMn)_{60}$	BCC + Al_3Ti + unknow n phase	6.09	−18.29	15.97	1458.50	1.27
CoCrFeNiCuAlMn	BCC + FCC + unknow n phase	4.57	−5.63	16.18	1607.64	4.61
$CoCrFe_{0.6}NiAlMo_{0.5}$	BCC + σ phase	5.61	−12.32	14.61	1784.04	2.12
$CoCrFeNiAlMo_{0.5}$	BCC + σ phase	5.47	−11.44	14.70	1786.00	2.29
$CoCrFe_{1.5}NiAlMo_{0.5}$	BCC + σ phase	5.30	−10.50	14.53	1788.08	2.47
$CoCrFe_2NiAlMo_{0.5}$	BCC + σ phase	5.15	−9.70	14.23	1789.85	2.63
$Co_{0.5}CrFeNiAlMo_{0.5}$	BCC + σ phase	5.54	−11.72	14.53	1787.60	2.22
$Co_{1.5}CrFeNiAlMo_{0.5}$	BCC + σ phase	5.39	−11.08	14.53	1784.67	2.34
$Co_2CrFeNiAlMo_{0.5}$	BCC + FCC + σ phase	5.29	−10.70	14.23	1783.54	2.37
TiCoCrNiCuAl	BCC + Cu + Cr	6.50	−16.67	14.90	1946.58	1.73
CoCrNiCuAlAu	FCC + AuCu	6.14	−6.45	14.90	1543.42	3.57
$CoCrFeNiCuAlMo_{0.4}$	BCC + α phase	5.05	−4.20	15.91	1701.80	6.45
$CoCrFeNiCuAlMo_{0.6}$	BCC + α phase	5.13	−3.95	16.08	1737.95	7.07
$CoCrFeNiCuAlMo_{0.8}$	BCC + α phase	5.20	−3.72	16.16	1771.99	7.69
CoCrFeNiCuAlMo	BCC + α phase	5.25	−3.51	16.18	1804.07	8.32
ZrHfTiCuFe	Compounds	9.84	−15.84	13.38	1949.40	1.64
ZrHfTiCuCo	Compounds	10.21	−23.52	13.38	1941.20	1.11
AlCrMoSiTi	Ordered BCC + Mo_5Si_3	4.91	−34.08	13.38	1918.90	0.75
$Ti_2CoCrFeNiCu$	Compounds	6.69	−14.04	14.53	1813.14	1.87
AlTiVYZr	Conpounds	10.35	−14.88	13.38	1802.10	1.62
ZrTiVCuNiBe	Compounds	11.09	−24.89	14.90	1820.67	1.09
$TiCoCrNiCuAlY_{0.5}$	Cu_2Y + $AlNi_2Ti$ + Cu +Cr	7.53	−18.32	16.00	1935.38	1.68

Table 1. Continued

Alloys	Structure	δ (%)	$\Delta Hmix$(kJ mol^{-1})	$\Delta Smix$ (J K^{-1} mol^{-1})	Tm (K)	Ω
$TiCoCrNiCuAlY_{0.8}$	Cu_2Y + $AlNi_2Ti$ + Cu + Cr	12.73	−19.00	16.16	1929.45	1.64
TiCoCrNiCuAlY	Cu_2Y + $AlNi_2Ti$ + Cu + Cr + unknown phase	13.45	−19.37	16.18	1925.79	1.62
$Zr_{57}Ti_5Al_{10}Cu_{20}Ni_8$	BMG	9.69	−31.50	10.18	1813.45	0.59
$Zr_{38.5}Ti_{16.5}Cu_{15.25}Ni_{9.75}Be_{20}$	BMG	13.36	−33.20	12.47	1828.35	0.69
$Zr_{39.88}Ti_{15.12}Cu_{13.77}Ni_{9.98}Be_{21.25}$	BMG	13.59	−34.27	12.34	1834.26	0.66
$Zr_{42.63}Ti_{12.37}Cu_{11.25}Ni_{10}Be_{23.75}$	BMG	14.05	−36.90	11.97	1844.44	0.60
$Zr_{41.2}Ti_{13.8}Cu_{12.5}Ni_{10}Be_{22.5}$	BMG	13.82	−36.72	12.18	1839.28	0.61
$Zr_{44}Ti_{11}Cu_{10}Ni_{10}Be_{25}$	BMG	14.27	−37.07	11.73	1849.48	0.59
$Zr_{45.38}Ti_{9.62}Cu_{8.75}Ni_{10}Be_{26.25}$	BMG	14.49	−37.23	11.46	1845.09	0.57
$Zr_{46.75}Ti_{8.25}Cu_{7.5}Ni_{10}Be_{27.5}$	BMG	14.70	−37.03	11.16	1848.95	0.56
$La_{55}Al_{25}Ni_5Cu_{10}Co_5$	BMG	16.19	−32.31	10.02	1200.78	0.37
$Nd_{60}Al_{15}Ni_{10}Cu_{10}Fe_5$	BMG	17.11	−27.37	9.99	1313.18	0.48
$Nd_{61}Al_{11}Ni_8Co_5Cu_{15}$	BMG	17.46	−27.43	9.82	1307.13	0.47
$Cu_{47}Ti_{33}Zr_{11}Si_1Ni_8$	BMG	8.46	−17.56	10.07	1669.63	0.96
$Cu_{47}Ti_{33}Zr_{11}Si_1Ni_6Sn_2$	BMG	8.36	−17.02	10.45	1645.17	1.01
$Fe_{61}B_{15}Mo_7Zr_8Co_7Y_2$	BMG	13.20	−30.13	10.30	1992.27	0.68
$Fe_{61}B_{15}Mo_7Zr_8Co_6Y_2Al_1$	BMG	13.24	−30.30	10.54	1983.91	0.69
$Fe_{61}B_{15}Mo_7Zr_8Co_5Y_2Cr_2$	BMG	13.20	−29.97	10.65	1999.53	0.71
$Au_{49}Ag_{5.5}Pd_{2.3}Cu_{26.9}Si_{16.3}$	BMG	5.30	−29.39	10.35	1377.64	0.49
$Dy_{46}Al_{24}Co_{18}Fe_2Y_{10}$	BMG	13.71	−33.26	10.95	1533.60	0.50
$Ti_{40}Zr_{25}Ni_3Cu_{12}Be_{20}$	BMG	12.03	−25.88	11.60	2010.40	0.90
$Ti_{40}Zr_{25}Cu_9Ni_8Be_{18}$	BMG	12.31	−28.26	11.98	1852.02	0.79
$Ti_{45}Cu_{25}Ni_{15}Sn_3Be_7Zr_5$	BMG	9.08	−21.22	11.90	1705.29	0.96
$Ti_{50}Ni_{24}Cu_{20}B_1Si_2Sn_3$	BMG	7.89	−27.87	10.31	1731.86	0.64
$Ti_{50}Zr_{15}Cu_9Ni_8Be_{18}$	BMG	11.64	−26.37	11.30	1833.82	0.79
$Ti_{55}Zr_{10}Cu_9Ni_8Be_{18}$	BMG	11.18	−25.43	10.70	1824.72	0.77
$Ti_{53}Cu_{15}Ni_{18.5}Al_7Hf_3Si_3B_{0.5}$	BMG	7.28	−32.23	11.28	1757.66	0.62
$Ti_{53}Cu_{15}Ni_{18.5}Al_7Sc_3Si_3B_{0.5}$	BMG	7.54	−31.75	11.28	1697.36	0.60
$Ti^{53}Cu^{15}Ni^{18.5}Al^7Ta^3Si^3B^{0.5}$	BMG	6.96	−31.28	11.28	1781.33	0.64
$Ti^{53}Cu^{15}Ni^{18.5}Al^7Nb^3Si^3B^{0.5}$	BMG	6.96	−31.22	11.28	1765.04	0.64
ZrHfTiCuNi	BMG	10.21	−27.36	13.38	1932.80	0.95
$Mg_{65}Cu_{20}Zn_5Y_{10}$	BMG	12.70	−5.98	8.16	1085.64	1.48
$Mg_{65}Cu_{15}Ag_5Pd_5Y_{10}$	BMG	9.27	−13.24	9.10	1074.86	0.74
$Mg_{65}Cu_{15}Ag_5Pd_5Gd_{10}$	BMG	9.27	−13.24	9.10	1053.49	0.72
$Mg_{65}Cu_{7.5}Ni_{7.5}Zn_5Ag_5Y_{10}$	BMG	9.53	-7.35	9.96	1107.24	1.50

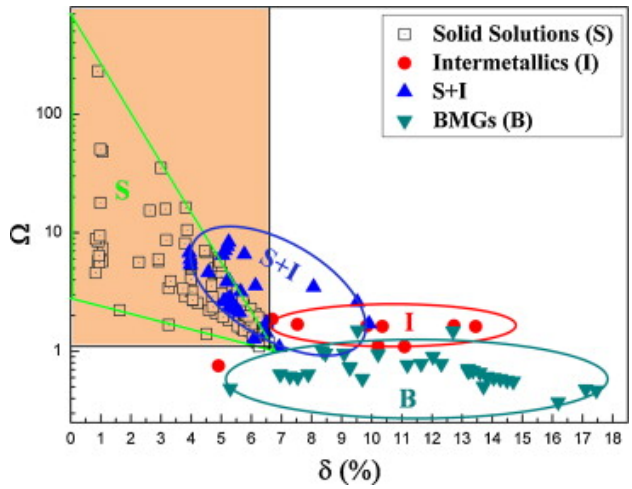

Figure 1The relationship between parameters δ, Ω and possible structures for multi-component alloys ("Solid Solutions" indicates the alloy contains only solid solution; "Intermetallics" indicates the alloy mainly contains intermetallic compound and other ordered phases; "S + I" indicates the solid solution with ordered compounds precipitated within; and "BMGs" indicates the alloy can form amorphous phase)[28]

Although high configurationally entropy has been hypothesized above as a solid solution stabilizer for equimolar, multi-component alloy (HEAs), its importance has been challenged by the well-designed experimental work of F Otto *et al*[30]. They used the alloy CrCoFeMnNi first reported by Cantor *et al*[1] with a single FCC phase as a base alloy and replaced one at a time Ti for Co, Mo or V for Cr, V for Fe and Cu for Ni. The replacement had the same room temperature crystal structure and comparable size/electronegativity as the elements being replaced to maximize solid solubility consistent with the Hume–Rothery rules.

They found that all the new alloys are no longer single phase but forms the second or interetallic phase. On the basis of such findings, they argued that with the total number of elements constant, the configuration entropy should be the same and therefore the new alloys should be just like the base alloy, and be single-phased. They further carried out thermodynamic calculations and concluded that phase formation in five-component (and possibly more components) alloys is consistent with a minimization of the total Gibbs

free energy, including both enthalpy and entropy contributions, and not just a maximization of the configuration entropy.

1.2 Microstructure of HEAs

Consistent with overwhelming configurational entropy, some HEAs are reported to be single-phased FCC[1, 31] or BCC[32, 33] solid solution. However, most of them contain secondary phase and even intermetallic precipitates depending on the composition and the history of thermo-mechanical treatment [21, 34-36]. In what follows, we will introduce the typical microstructure morphologies and how they evolve with different processing and with composition tuning. Also included is the recrystallization behavior of single phased HEAs used to control grain size.

1.2.1 Morphology variation with thermo-mechanical treatment and composition

Take the well-studied composition AlxCoCrCuFeNi[21, 35, 37, 38] with x=0.5 [35]for example, the microstructure morphology varies with different processing procedures: as-cast in arc melting, as-forged at 900˚C for 15mins by a 40% thickness reduction, water quenched(WQ)after homogenized at 1100˚C for 24h and furnace cooled (FC) after the same homogenizing condition. The XRD pattern for four different conditioned samples is displayed in

Figure 3 and corresponding morphology is presented in Figure 4 where dendrite region (marked as matrix FCC) and inter-dendrite region (Cu-rich FCC) are persistent among all processing conditions, which is typical for HEAs. The formation of the dendrite and inter-dendrite is heavily dependent on the cooling rate as shown in Figure 2[21]. From EDS (energy-dispersive spectroscopy) analysis, the two regions show segregation with particular elements (the composition for each region is shown in Table 2 and Table 3, respectively), which is another classic characteristics related to HEAs.

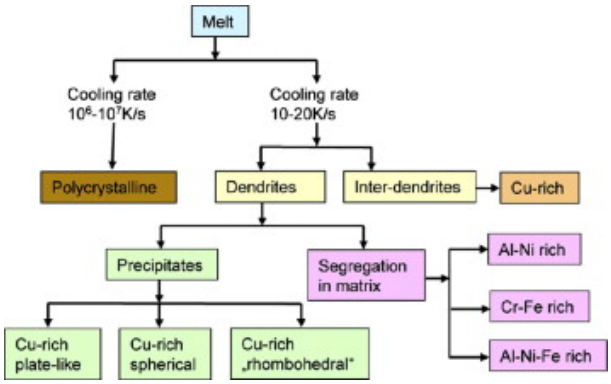

Figure 2 Schematic representation of phase segregation observed during solidification of AlCoCrCuFeNi HEA by two different processing conditions: splat quenching (cooling rate 10^6-10^7 K s ^{1}) and casting (cooling rate 10-20 K s ^{1})[21]

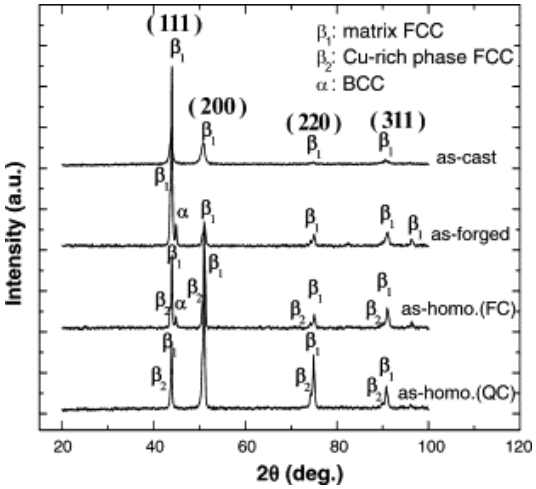

Figure 3 X-ray analysis of samples in four different states[35]

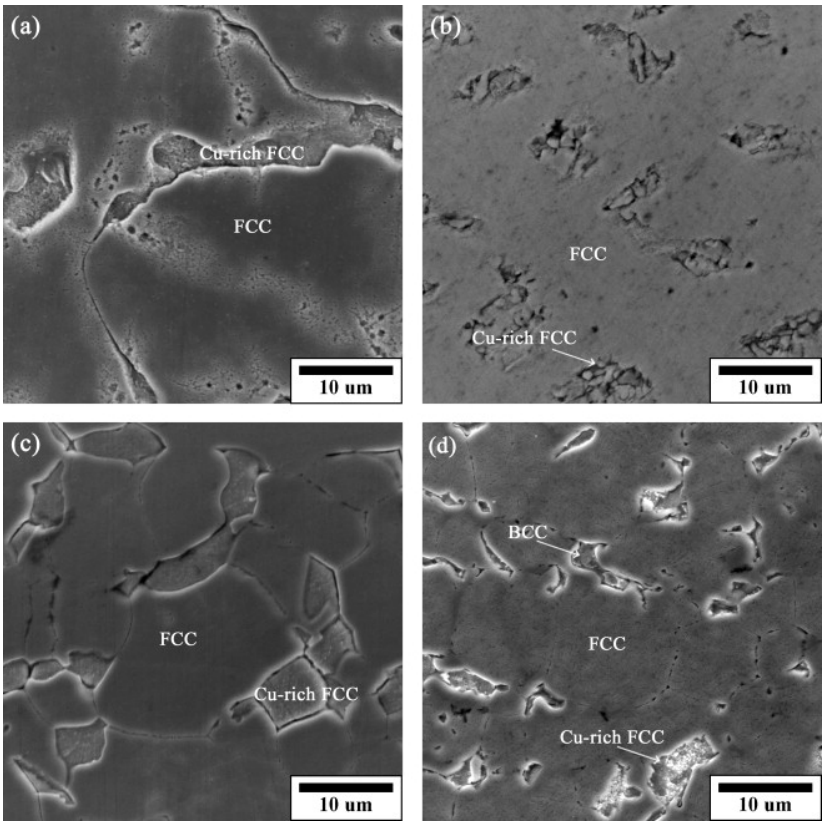

Figure 4 Microstructures in the (a) as-cast, (b) as-forged, (c) as-homogenized-WQ, and (d) as-homogenized-FC states. Dendritic morphology is persistent under all conditions[35].

Table 2 Compositions of dendrite regions obtained by EDS analysis (in at. %)[35]

State	Al	Co	Cr	Cu	Fe	Ni
As-cast	9	19	21	11	20	20
As-forged	7	21	22	10	21	19
As-homogenized-FC	7	21	22	11	21	18
As-homogenized-WQ	7	20	21	11	22	18

Table 3 Compositions of interdendrite regions obtained by EDS analysis (in at. %)[35]

State	Al	Co	Cr	Cu	Fe	Ni
As-cast	12	5	4	61	5	13
As-forged	7	10	10	50	10	14
As-homogenized-FC	7	3	2	75	3	11
As-homogenized-WQ	10	5	4	59	6	15

The phase component can also be adjusted by a particular element [38-43], Al, as in the above case[38]. With the addition of Al from *x=0* to *x=3*, the phase changed from FCC (*x=0-0.5*) to mixed FCC plus BCC (*x=1.0-2.0*) and to BCC (*x=2.3-3.0*). Another way to examine the element effect is through substitution. F Otto *et al*[30] started with a base HEA CoCrFeMnNi and then replaced the elements Co, Cr, Fe and Ni one at a time by 3*d* and 4*d* transition metals having the same room temperature crystal structure and closest electronegativity and atomic radius. Five new alloys have thus been resulted, in which the substitutional element is italicized for ease of identification: CoCrFeMn*Cu*, *Ti*CrFeMnNi, CoMoFeMnNi, CoVFeMnNi and CoCrVMnNi. All the new substitutional alloys exhibited multi-phase microstructures containing intermetallic compounds and, in one case, two fcc solid solution phases.

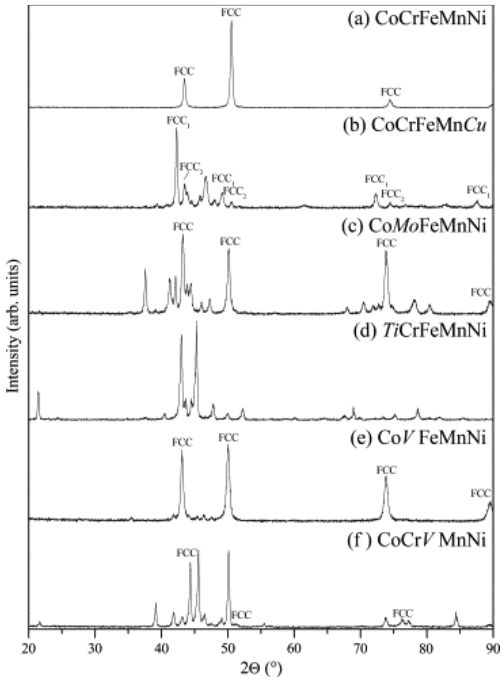

Figure 5 X-ray diffraction patterns of the six alloys investigated in the present study after three-day anneals at 1123 K (spectrum b) and 1273 K [30]

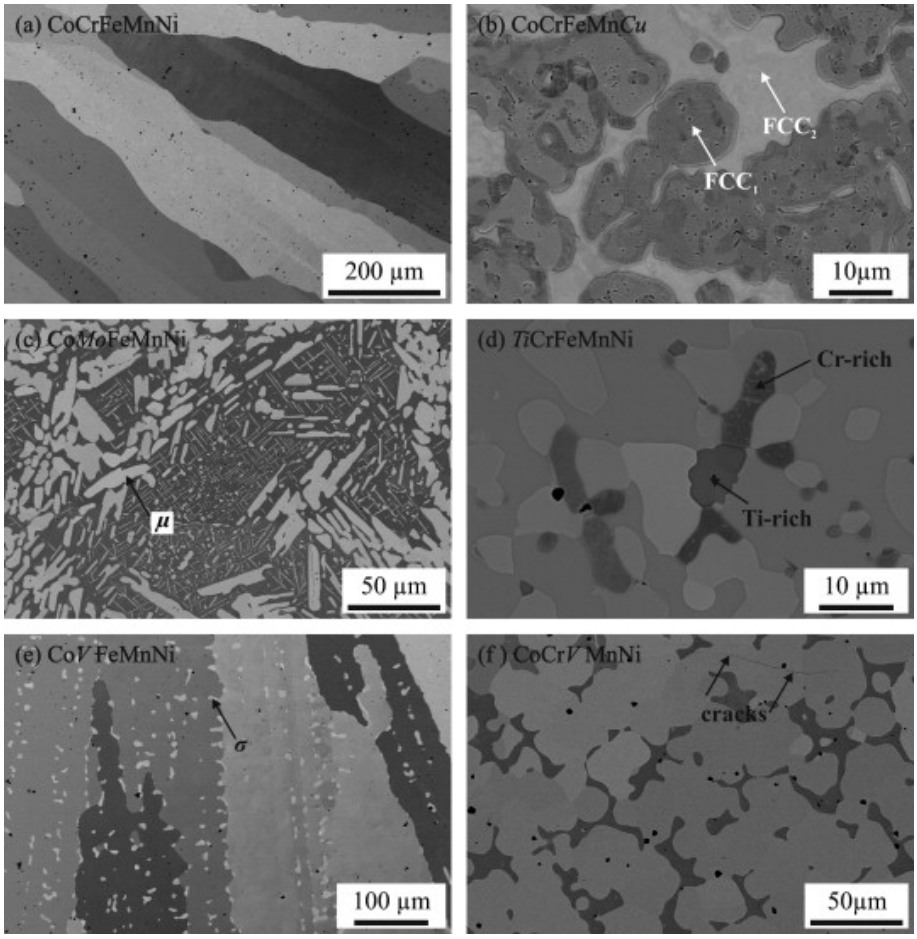

Figure 6 Backscatter electron micrographs of the annealed microstructures of the six multi-component alloys investigated: (a) CoCrFeMnNi; (b) CoCrFeMnCu; (c) CoMoFeMnCu; (d)TiCrFeMnNi; (e)CoVFeMnNi; and (f) CoCrVMnNi. The small, dispersed dark spots in (a) are oxide particles (containing mainly Cr and Mn) resulting from trace levels of oxygen present in the raw materials and possibly also from contamination during arc melting[30]

1.2.2 Recrystallization behavior

As grain size refinement is very effective in strengthening traditional polycrystalline materials [44-47], it is of great importance that the recrystallization behavior in HEAs be understood. Up to date, one system (single phase FCC high entropy alloy FeCoCrMnNi)

has been systematically studied by Liu WH *et al*[14] and the main findings will be introduced here.

The samples were first cold rolled by 70% and then polished and sealed in a vacuumed quartz tube. The sealed samples were then annealed at 850, 900, 925 and 950˚C for different times to obtain various grain sizes. The annealing results are shown in Table 4 and selected representative microstructures are displayed in Figure 7.

Table 4 Grain sizes of the FeCoCrMnNi samples annealed at 850, 900, 925 and 950 °C for different annealing times[14]

T (˚C)	Time (h)	Grain size (μm)	T (˚C)	Time (h)	Grain size (μm)	T (˚C)	Time (h)	Grain size (μm)	T (˚C)	Time (h)	Grain size (μm)
850	1	3.9	900	0.5	5.2	925	1	14.4	950	1	16.5
	1.25	5.7		1	6.9		2	18.1		2.5	22.4
	1.5	6.5		1.25	9.0		3	20.7		4	26.2
	1.75	7.2		1.5	11.4		3.5	21.8			
	2	8.4		2	12.7						
	2.5	9.0		3	14.3						
	4	10.6		10	21.5						
	6	12.1									

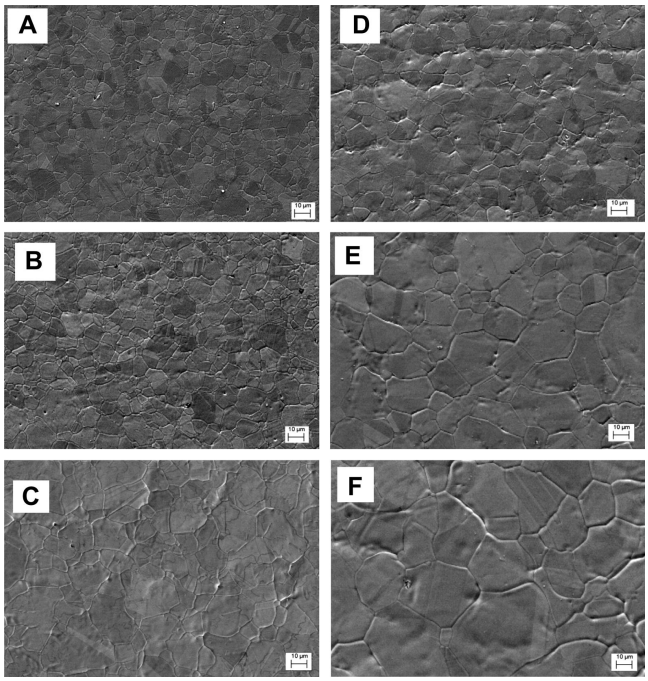

Figure 7 Microstructures of the FeCoNiCrMn alloy specimens annealed at 850 °C (A–C) and 925 °C (D–F). The annealing time periods were 1 h for (A) and (D), 2 h for (B) and (E), 6 h for (C) and 3.5 h for (F)[14]

They found the grain size and time relation best described with $n=3$ and $D_0=1\mu m$ by classical theory for grain growth[48]:

$$D^3 - D_0^{\ 3} = Ct \tag{1.6}$$

where D is the instantaneous grain size, D_0 is the initial grain size, t is time. The n value determines the mechanism and C determines the diffusion processes. This relationship is schematically shown in Figure 8 according to equation(1.6).

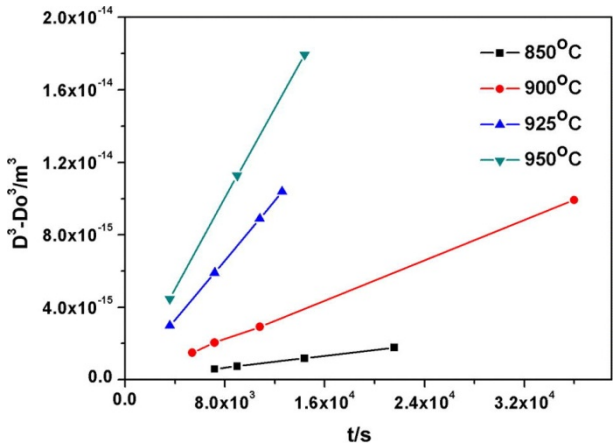

Figure 8 Grain size as a function of the annealing time for the FeCoNiCrMn alloy specimens heat treated at 850, 900, 925 and 950 °C. A linear relation between the cube of the grain size and time is observed[14]

The kinetics constant C in equation (1.6) has an Arrhenius form:

$$C = A_0 \exp(-Q / RT) \tag{1.7}$$

By plotting lnC, which is $\ln[(D^3 - D_0^{\,3}) / t]$ by equation (1.6), against the reciprocal temperature 1/T, they found the activation energy to be 321.7 kJ mol^{-1}, much higher than that of AISI 304LN stainless steels, 150 kJ mol^{-1}, and concluded that sluggish diffusion indeed occurred during the annealing of the current HEAs as a result of the lack of a major diffusion element and the necessity for the cooperative diffusion of the constituent atoms in order to have proper composition partitioning.

1.3 Mechanical properties of HEA

Expanding the current materials pool vastly, HEAs has demonstrated its potential as candidates for structural applications by being strong, ductile, and temperature-resistant[5]. Furthermore, the feature that no dominant constituent serve as a solute may present us a fundamentally different picture of deformation mechanism in HEAs compared to that of conventional materials. The understanding of the deformation mechanism may afford us new means to improve HEAs.

1.3.1 Hardness, specific strength, thermal stability

The hardness of typical HEAs as reported in literature is shown in Figure 9 along with that of typical steels [7]. As can been seen, HEAs exhibit a wide range of hardness (which is good, meaning a wide choice in terms of industry application) depending on the crystal structure of dominant phase. Normally HEAs with BCC is harder while HEAs with FCC is softer, resembling traditional alloys. For example, MoTiVFeNiZrCoCr (refractory BCC phase HEA) attains an extremely high hardness over 800 HV while CoCrFeNiCu (FCC) is less than 200 HV.

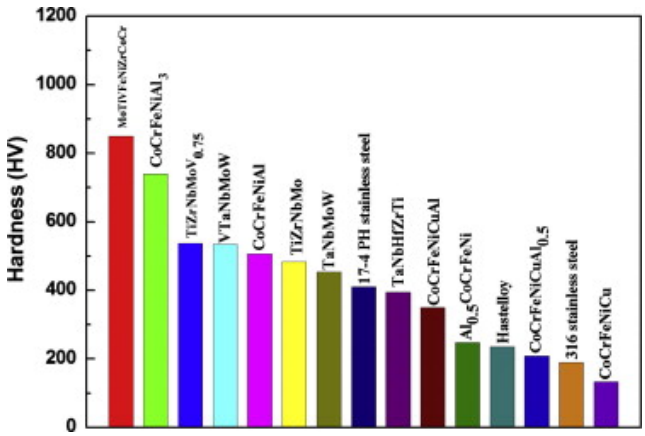

Figure 9 Wide range of hardness for HEAs, compared with 17-4 PH stainless steel, Hastelloy, and 316 stainless steel [7]

In addition to hardness, specific strength (defined as yield strength versus density) for HEAs (as shown in Figure 10) in comparison with BMGs, conventional alloys, polymers and foam materials, also stand among the highest.

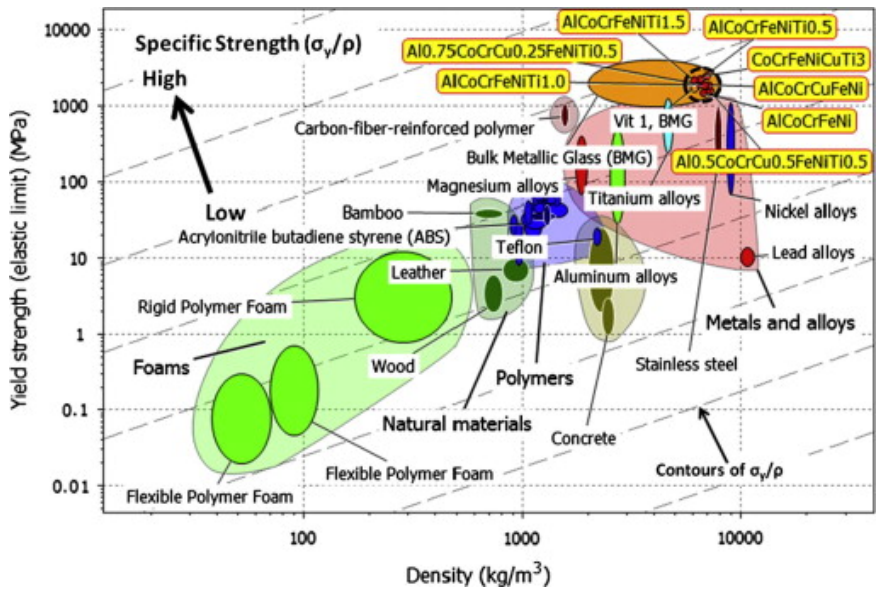

Figure 10 Yield strength σ_y versus density ρ. HEAs (dark dashed circle) compared with other materials, particularly structural alloys. Grey dashed contours (arrow indication) label the specific strength, σ_y/ρ from low (right bottom) to high (left top). HEAs are among the materials with highest strength and specific strength [7]

HEAs can also possess excellent temperature-resistant mechanical properties compared to that of conventional super-alloy such as Inconel 718. Figure 11 shows the temperature-dependence of yield strength for two refractory HEAs, NbMoTaW and VNbMoTaW, which were investigated by Senkov *et al*[33]. Both alloys are superior to Inconel 718 at temperatures from 600˚C above.

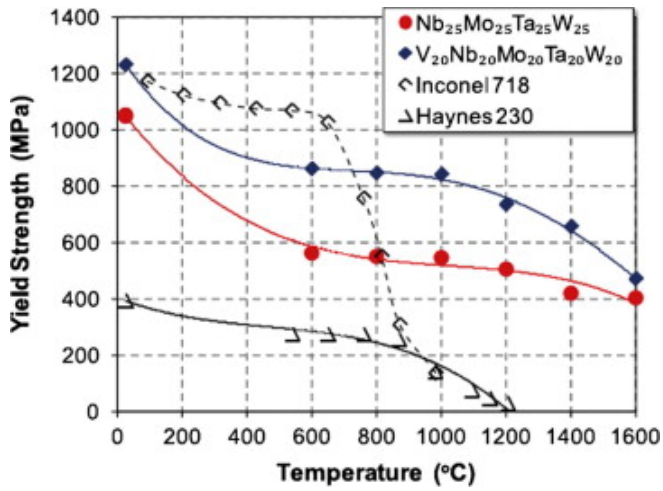

Figure 11 Temperature dependence of yield strength of NbMoTaW, VNbMoTaW, Inconel 718, and Haynes 230 alloys[49]

1.3.2 Mechanical properties of single FCC-phased FeCoCrMnNi

As shown in the microstructure section, HEAs can be very complicated containing secondary phase and ordered and disordered precipitates. Although hardness, yield strength, and elongation can be easily obtainable for complex HEAs, the correlation between properties and the structure would be difficult, as there are four effects as referred to high entropy effect, sluggish diffusion effect, severe lattice distortion effect and cocktail effect[3] at playing even without the multi-phases making it more complicated. Therefore, our introduction here will be directed to FeCoCrMnNi, a single FCC phase HEA.

1.3.2.1 Grain size dependence

Grain size variation (from several microns to more than hundred) was achieved by cold rolling and then recrystallization at different temperatures and/or for different times as in Liu WH *et al*[14] and F Otto *et al* [12]. Liu *et al*[14] measured the room temperature hardness, correlated it with corresponding grain size and found the correlation follows the Hall-Petch relation as shown in Figure 12. Otto F *et al* [12]examined the yield strength as a function of grain size not only at room temperature but also for high temperatures up to 1073K, they again illustrated that the Hall-Petch

relation was well obeyed (Figure 13). To further validate the Hall-Petch observation, they also show the microstructure evidence (Figure 14) of dislocation pile-up for sample deformed at 873K.

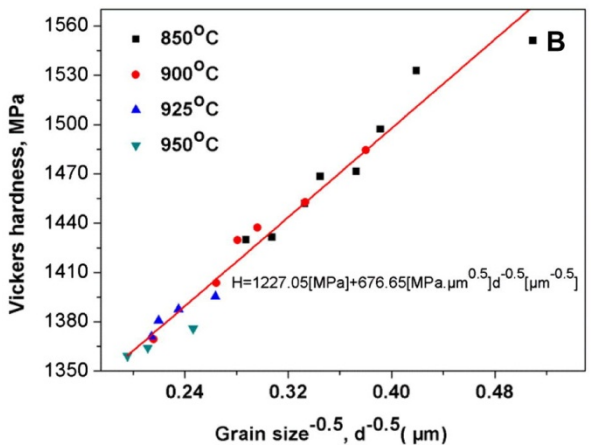

Figure 12 Hardness as a function of grain size in the FeCoNiCrMn alloy[14]

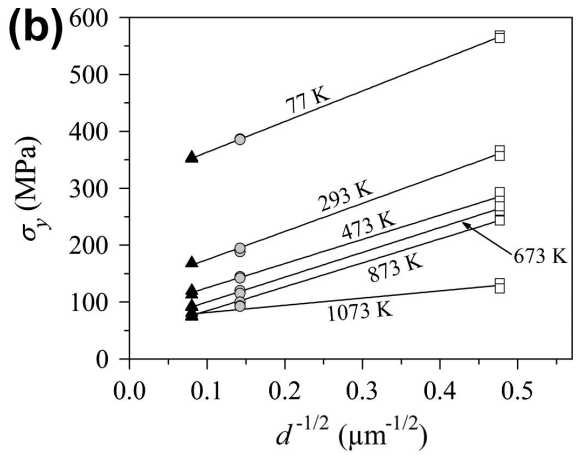

Figure 13 Temperature and grain size dependence of 0.2% offset yield stress[12]

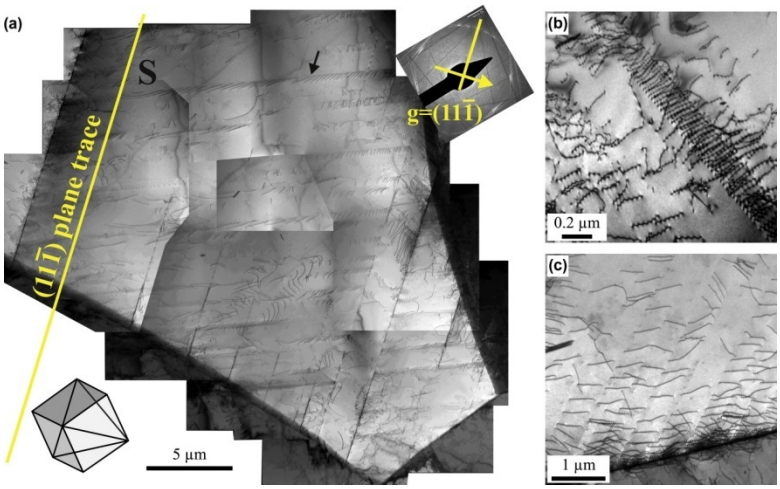

Figure 14 Representative TEM BF micrographs from the gauge sections of interrupted tensile test specimens of the coarse-grained CoCrFeMnNi alloy (grain size 155 μm) after relatively small tensile strains: (a) 1.7% at 873 K, (b) 2.4% at 77 K and (c) 2.1% at 293 K pile up is clearly seen in all three temperatures[12]

1.3.2.2 Deformation mechanism

During the tensile tests of FeCoCrMnNi, Otto F *et al*[12] discovered two features: the strength and ductility are both improved drastically as the test temperature decreased; and for deformation at 673K and above (the result is shown in Figure 15) the Portevin-Le Chatelier (PLC) effect (serrated flow) was observed. The reason leading to the latter feature hasn't been addressed but it has been clarified for the first feature.

The first feature was ascribed to a mechanism transition from conventional dislocation glide to deformation twinning. They discovered extensive twinning at a plastic strain of 20.2% at 77K for fine-grained FeCoCrMnNi. A lower magnification overview of the twinned microstructure is presented in Figure 16a.The high-resolution TEM image in Figure 16b focuses on a region in which two deformation twins with a thickness of about 2.5 nm cross the field of observation. Figure 16c represents the region outlined by a white square in Figure 16b after additional FFT filtering and they can be described by twinning element just like in traditional FCC.

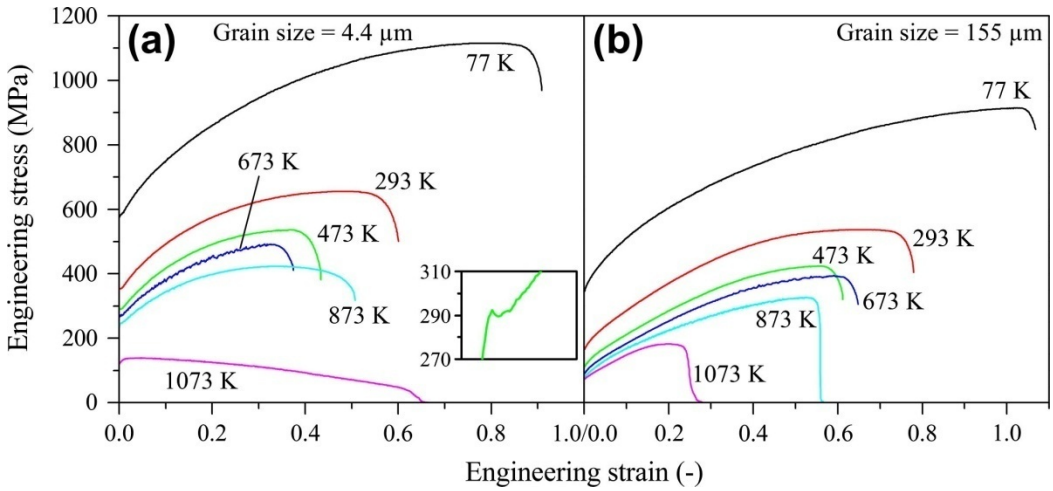

Figure 15 Representative engineering stress–strain curves of the CoCrFeMnNi alloy at the six testing temperatures for the (a) fine-grained (grain size 4.4 μm) and (b) coarse-grained (grain size 155 μm) materials. The inset in (a) shows a small load drop after yielding for a fine-grained sample that was tested at 473 K[12]

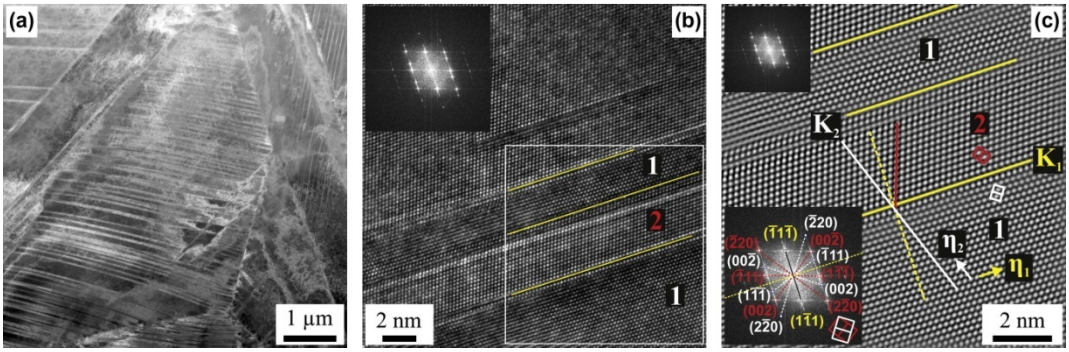

Figure 16 TEM micrographs characterizing deformation twinning in the fine-grained CoCrFeMnNi alloy (grain size 4.4 μm) after a strain of 20.2% at 77 K. (a) Overview of the twinned microstructure acquired in the HAADF mode. (b) High-resolution TEM image of twins denoted “1” and “2”, with the corresponding FFT inset. (c) FFT-filtered image of the area outlined by the white square in (b) showing the corresponding twinning elements. The inset in the lower left corner of (c) shows the fully indexed intensity maxima in reciprocal space[12]

1.4 Proposed research plan

Over one hundred HEAs have been reported and some were tested to obtain strength and related mechanical properties. However, the correlation between properties and structures has little been explored fundamentally and quantitatively[12], such as the nucleation, multiplication and propagation of dislocation, the structure of dislocation line, the deformation mechanism as a function of temperature, strain rate and grain size, strengthening mechanism and etc.

Our current work aims to uncover the deformation mechanism of HEAs in two circumstances: localized deformation in single crystal with low dislocation density and global deformation (i.e., tension) at high temperatures with the same sample condition. For the reason already mentioned, we choose FeCoCrMnNi with a single FCC phase. In particular, first, we will investigate the dislocation nucleation mechanism through nanoindentation on a single grain (very low dislocation density) of annealed polycrystalline FeCoCrMnNi with a grain size of microns. As a single grain after annealing can be treated like single crystal and the mean space of dislocation is wide, we expect, during load-controlled nanoindentation, the indenter with a small tip radius (less than 1μm) will be unlikely to encounter any pre-existing dislocation and trigger pop-in or displacement burst as the load approaching a critical value. Pop-in, also termed as incipient plasticity, has long been associated with dislocation nucleation. Therefore, the study of pop-in (the model will be introduced in Methodology) will help answer many fundamental questions: how dislocations are generated in a dislocation-free volume, homogenous or heterogeneous? Will the critical stress required to nucleate the dislocation achieve the theoretical strength as in a perfect crystal? Is the nucleation process temperature dependent? Also, we would examine other related issues associated with the nucleation process.

With the localized deformation covered, efforts will also be made to characterize mechanism in global deformation as in tension. The technique used is stress relaxation at different strains and at various temperatures, which enables extracting the signatory parameters of deformation mechanism, the activation volume and activation energy. Furthermore, by carrying out relaxation at different strains along the stress strain curve,

an understanding can also be obtained of how the relaxation behavior evolves with the strain or structure.

Since the deformation mechanism has been clarified for many traditional FCC polycrystalline materials, the experimental results under two deformation modes, local and global, can be used to examine the similarities and differences between deformation behavior of HEAs and of conventional materials. The comparison would offer us insights on the mechanical deformation of HEAs.

2 Methodology

2.1 Introduction: nanoindentation for the study of incipient plasticity

Nanoindentation is a versatile technique. As stated by Schuh[50]: "the most common use of nanoindentation is for the measurement of hardness and elastic modulus, and there has been considerable progress in the measurement of other mechanical parameters as well, including hardening exponents, creep parameters, and residual stresses Such measurements have broad application across the physical sciences, and there are several recent reviews on the use of nanoindentation for property extraction. However, nanoindentation also lends itself to more fundamental inquiries in materials science. New capabilities in *in-situ* and *ex-situ* imaging, acoustic emission detection, and high-temperature testing are now being used to probe nanoscale phenomena such as defect nucleation and dynamics, mechanical instabilities or strain localization, and phase transformations."

In this work, we will employ its capability to probe material volume on nanoscale which has been extensively used to investigate the origin of incipient plasticity for crystal deformation [51-60]. When a tip with proper radius (on the order of submicron) is brought to press a well annealed sample, the indented volume is small (~nm) enough to include none preexisting dislocation and as stress associated with the applied load reaching a critical level, a displacement burst (or pop-in) will be seen on the load-displacement curve [61]. The pop-in event is, therefore, attributable to the nucleation of dislocations in the crystal [53, 62-69] and is directly observed in the in-situ TEM nanoindentaton on Al[70, 71]. Structural defects leading to dislocation nucleation have been discussed by Mason *et al*[55] and they proposed a statistical model to analyze dislocation nucleation in Pt and successfully extracted activation energy and volume for the incipient plasticity during nanoindentation. In this work, their model will be adopted and outlined below.

2.2 Statistical model determining the activation volume and energy for the onset of plasticity

From the nanoindentation on single crystal Pt[55], they found higher temperatures and lower rates promote the first displacement burst and related this to a stress-biased, thermally activated yielding mechanism. They assume that there is a single local, kinetically limiting process that takes place under the indenter, for example, the nucleation of a dislocation, which requires an activation enthalpy. This energy barrier can be reduced through the combination of mechanical work and thermal fluctuation. Statistically the process may be described by a rate equation in Arrhenius form:

$$\dot{n} = \eta \exp\left(-\frac{H - \sigma V}{kT}\right) \tag{2.1}$$

where $\dot{n}$ is the local rate at which the critical event occurs per unit volume of material, H is the activation enthalpy, V is the activation volume, $H - \tau V$ is the activation energy for the reaction, kT is the average available thermal energy, and η is pre-exponential frequency factor. Separating $H - \tau V$ into separate items, equation (2.1) has a new form:

$$\dot{n} = \eta \exp(-\frac{H}{kT}) \exp(\frac{\sigma V}{kT}) \tag{2.2}$$

Where the first exponential term gives the probability per attempt of a yield event in a perfect, stress-free crystal, and the second shows the dependence of the rate of displacement bursts on applied shear stress.

The global rate for displacement burst would be found by integrating over the volume of the indented material near the contact region (Ω)

$$\dot{N} = \eta \exp(-\frac{H}{kT}) \iiint_{\Omega} \exp(\frac{\sigma V}{kT}) d\Omega \tag{2.3}$$

As the stress field under the indenter is quite a complicated function of position, to integrate the above term analytically would be impossible, it is sensible to assume, if the

volume Ω is selected properly, the stress is a constant equal to the maximum shear stress calculated within Hertzian contact framework[72, 73]:

$$\sigma \equiv \tau_{\max} = \frac{0.47}{\pi} \cdot \left(\frac{4E_R}{3R} \right)^{2/3} P^{1/3} \tag{2.4}$$

where E_R is the reduced modulus of sample and indenter, R is the tip radius and P the load. The volume Ω is assumed to scale with contact radius, a

$$\Omega = \pi a^3 = \pi \left(\frac{3PR}{4E_R} \right) \tag{2.5}$$

Using simple statistics, the rate of the change of *F(t)* (the cumulative fraction function for first pop-in) is proportional to the number of unyielding samples remaining, and to the rate at which one of those remaining samples displays the onset of plasticity

$$\dot{F}(t) = [1 - F(t)]\dot{N}(t) \tag{2.6}$$

By a series of mathematical deduction (refer to for detailed information and meaning of each parameter), they came to two important equations, equations (2.7) and (2.8) to extract the activation volume, V

$$\ln[\frac{1}{\ln(1-F)}] = \alpha P^{1/3} + \beta \tag{2.7}$$

$$V = \frac{\pi}{0.47} (\frac{3R}{4E_r})^{2/3} kT \cdot \alpha \tag{2.8}$$

Then by changing the nanoindentation temperature and recording the pop-in load statistics at different temperatures, they developed the equation (2.9) to obtain activation energy:

$$P^{1/3} = \gamma kT + \frac{\pi}{0.47} (\frac{3R}{4E_r})^{2/3} \frac{H}{V} \tag{2.9}$$

On the basis of activation volume, V and activation energy, H, the physical picture of dislocation nucleation mechanism can be drawn.

2.3 Phenomenological model to determine activation volume and energy for stress relaxation

Stress relaxation technique has been extensively used to characterize dislocation mechanisms in a variety of materials over a range of materials [74-78]. In a stress relaxation tests, the machine cross-head is stopped. The sample is maintained at a constant total displacement or strain, while the stress is observed to decrease as time proceeds.

The total displacement, l, is composed of three parts: the elastic displacement of the sample, l_e, the elastic displacement of machine l_m and the plastic displacement l_p of the sample[75, 77]:

$$l_e + l_p + l_m = l \tag{2.10}$$

l is constant during relaxation, $\dot{l} = 0$

$$\dot{l}_e + \dot{l}_p + \dot{l}_m = 0 \tag{2.11}$$

l_m is related to the stiffness of the testing machine given by:

$$l_m = \frac{dP}{s} \tag{2.12}$$

which is practically constant in the small range of load P involved in stress relaxation. Then converting the displacement rate to strain rate equation (2.11) can be written:

$$\dot{\varepsilon}_e + \dot{\varepsilon}_p = -\frac{A_0}{l_0 s}\dot{\sigma} \tag{2.13}$$

where A_0 and l_0 are the cross section area and the displacement of specimen at the time t=0. While $\dot{\varepsilon}_e = \frac{\dot{\sigma}}{E}$, the relation between plastic strain rate and stress rate then takes the form:

$$\dot{\varepsilon}_p = -\dot{\sigma} / M \tag{2.14}$$

where $M = \frac{A_0}{l_0 s} + \frac{1}{E}$, the activation volume V is defined as[79, 80]:

$$V = \sqrt{3} kT \partial \ln \dot{\varepsilon} / \partial \sigma \tag{2.15}$$

Combining equation(2.14), equation (2.15) can be rewritten as:

$$V = \sqrt{3} kT \frac{\partial \ln(-\dot{\sigma})}{\partial \sigma} \tag{2.16}$$

So by plotting $\ln(-\dot{\sigma})$ against σ, we can obtain activation volume.

The activation enthalpy, on the other hand, is defined as [79, 81, 82]:

$$H = -TV \left(\frac{\partial \tau}{\partial T} \right)_{\dot{\varepsilon}} \tag{2.17}$$

The term $\left(\frac{\partial \tau}{\partial T} \right)_{\dot{\varepsilon}}$ can be obtained from a slope of a stress-temperature plot determined using a different specimen for each temperature. The Gibbs free activation energy, ΔG, is then expressed as:

$$\Delta G = H - \tau V \tag{2.18}$$

With parameters H or G and V available, we can identify the rate-controlling mechanism by comparing them with the characteristic values of a particular model such as Periels stress, dislocation-intersection, cross-slip and etc.

2.4 Experimental facility

2.4.1 Nanoindenter

Nanoindenter is conceptually an extension of micro-hardness tester. But the recent progress in nanoindenter development has made the nanoindentation that otherwise is impossible to capture very sensitive events occurred during deformation such as pop-in. The resolution in load and displacement has attained nanoscale and also remarkable is the acquisition rate. These highly desirable characteristics promote the nanoindenter to be a unique tool in probing materials proeperties.

For the system (Triboindenter, Hysitron) used in our study, the resolution reaches 0.04nm in displacement and 1nN in load and the acquisition rate can go to thousands and even more per second depending on testing needs. The real system is shown in Figure 17. It is computer controlled and equipped with a high temperature stage that can run up to a maximum high of 200˚C and a minimum low of -20˚C (The latest system can even reach to 600˚C which covers up to intermediate high temperature for a wide range of materials and which is also a great breakthrough to testing possibilities).

The testing workplace is very delicate which is detailed in Figure 18. It consists of a motorized sample stage that enables moving in X and Y direction on the horizontal plane, a microscope to locate, image and designate the indentation position on the sample, a transducer to which the indenter tip (often made of diamond) is attached and to control the tip movement along Z axis and exert a load on it up to 10mN and a thermal shield that protects the transducer from being heated by the hot sample at high temperature testing (this part is unnecessary for testing at ambient temperature). Of course, if a high load transducer is used, a maximum load up to 1N can be achieved. Table 5 also lists detailed specifications of the Triboindenter along with that of Nanoindenter XP system, a rival and another popular system.

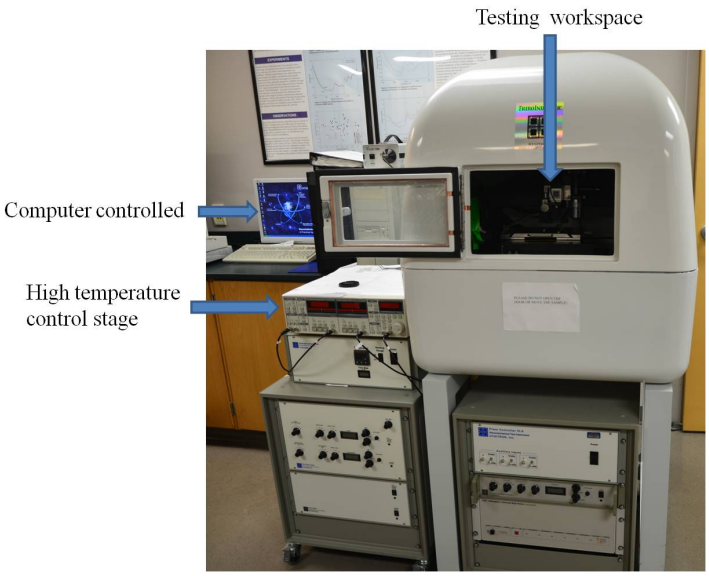

Figure 17 The Triboindenter system

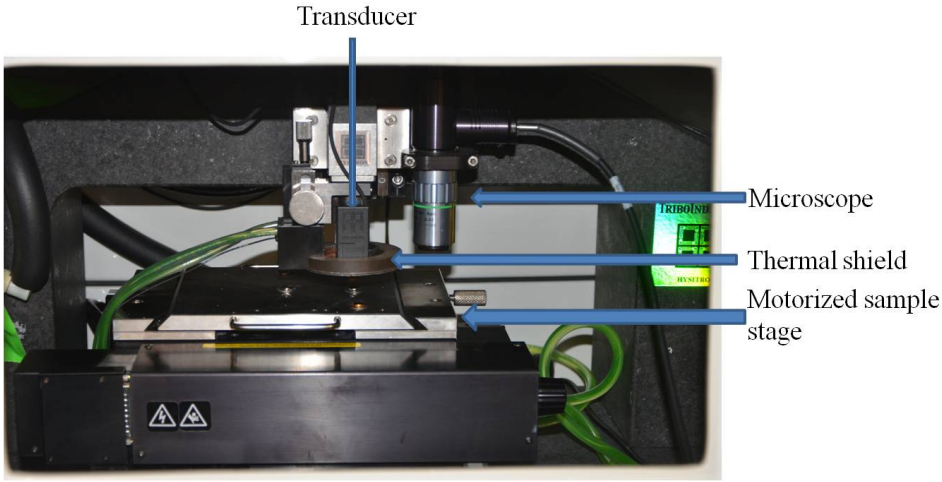

Figure 18 The detailed image for the testing workspace

Table 5 Specifications of Triboindenter and Nano Indenter XP

	Triboindenter	Nano Indenter XP
Load application	Static electric force	Electric magnetic force
Displacement measurement	Capacitance gauge	Capacitance gauge
Mass of indenter tip	236 mg	6 g
Maximum force	10 mN	500 mN
Load resolution	1 nN	50 nN
Load noise floor	100 nN	1 μN
Spring stiffness	116 N/m	100 N/m
Maximum displacement	5 μm	500 μm
Displacement resolution	0.04 nm	0.01 nm
Displacement noise floor	0.2 nm	0.1 nm
Thermal drift	< 0.05 nm/sec	< 0.05 nm/sec
Feedback rate	78 kHz	500 Hz
Data acquisition rate	30 kHz*	5 Hz
Mechanical bandwidth	200 Hz	12 – 15 Hz

2.4.2 High temperature testing

For the stress relaxation carried out at high temperatures. An Instron 5566 tensile machine coupled with a furnace is used. The schematic is shown in

Figure 19. The furnace has three thermal couples, on the upper, middle and lower side, connected to the temperature controller and monitor, which has three digital windows to display the temperature for the three thermal couples. The temperature is able to reach one thousand degrees (which is about $2/3T_m$ (T_m: melting point) of FeCoCrMnNi).

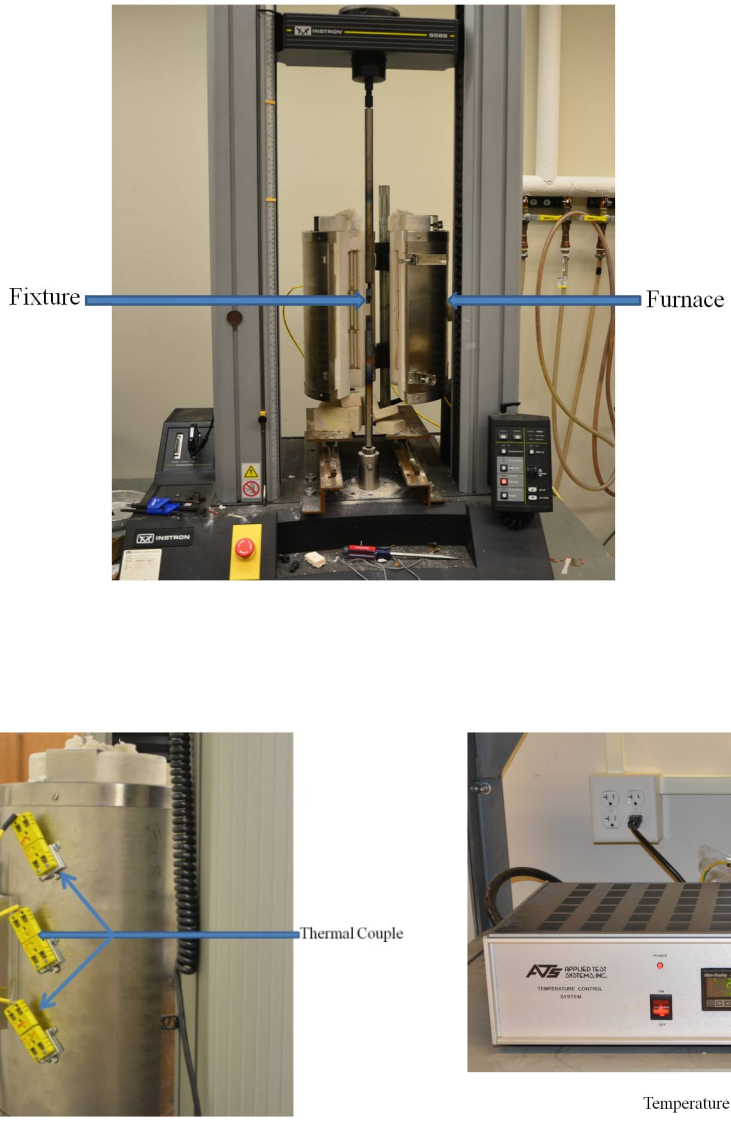

Figure 19 (a) schematic illustration of the stress relaxation testing system for high temperatures and (b) the back view of the furnace in (a) which has three thermal couples connected and (c) the temperature controller and monitor that controls the designated temperature and receives another end of the three thermal couples to monitor the furnace temperature

3 Incipient plasticity and dislocation nucleation studied using nanoindentation technique

3.1 Sample preparation and microstructure characterization

The material used in this study was prepared by arc-melting a mixture of constituent metals (purity > 99wt. %) with a nominal composition $Fe_{20}Co_{20}Cr_{20}Ni_{20}Mn_{20}$ (in atomic percentage) in a Ti-guttered high purity Argon atmosphere. The ingot was re-melted at least four times to ensure homogeneity before it was drop-cast into a mold. The as-cast ingot was further rolled by 70% reduction in thickness.

Rectangular samples were sliced from the rolled plate, grounded, and polished to a mirror finish of 0.01μm. It is, then, annealed in vacuum at 900˚C for 10h to induce recrystallization and grain growth, and to remove any surface stress resulted from the mechanical polishing[83]. An optical micrograph of the sample after the above processes is shown in

Figure 20(a), grain size ranging about 30-50μm. The crystal structure is identified by XRD pattern in

Figure 20(b) to be a single FCC phase as reported[1, 12, 14, 15].

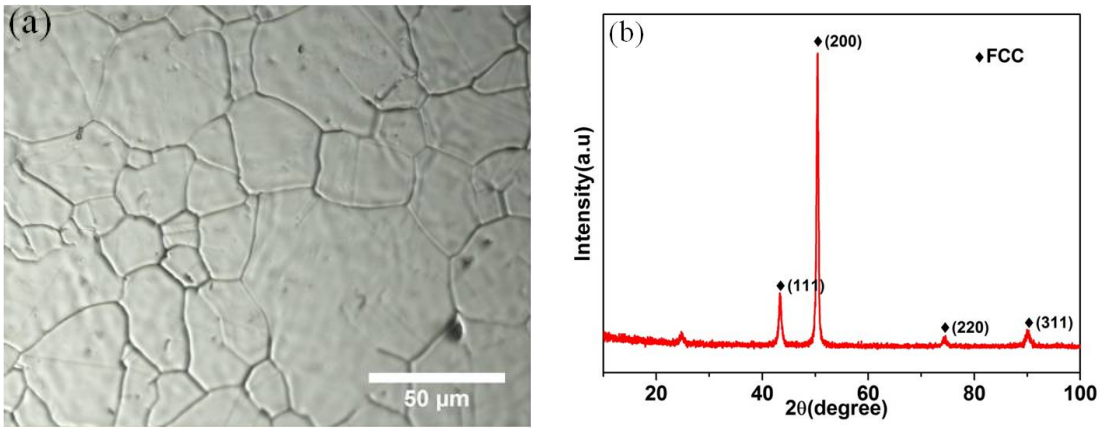

Figure 20 (a) Optical microstructure of the annealed FeCoCrNiMn sample with an average grain size about 30~50μm and (b) XRD pattern indicates a single FCC structure.

Instrumented nanoindentation experiments at room temperature were performed using a Hysitron Triboindenter (Hysitron, Inc. Minneapolis, MN), with a Berkovich diamond tip of effective tip radius of 233nm determined using standard method[84-86]. Indentations were made at 4μm apart from each other, with a constant load of 200μN and loading segment of 5s, and the indentation depth was typically about 30nm. The 4μm was chosen to avoid the overlap of plastic zones created by neighboring indentations yet to accommodate as many indentations as possible on a single grain. Eleven grains were randomly selected and 120 indentations on each grain were carried out; there are total 1320 indentations.

Nanoindentation tests at elevated temperatures were conducted with an attached heating stage[87]. A blunt high temperature Berkovich tip was selected with a radius of 638nm, producing essentially spherical surface contacts with the depth being probed in the present study. At least 16 indents at each temperature were conducted at temperatures of 22, 50, 100 and 150˚C. The loading function remained unchanged throughout the test. The temperature was monitored and controlled using a J-type thermocouple in direct contact with the specimen surface. The test system was allowed about one hour to thermally stabilize at the desired test temperature. For successive indentations at a fixed temperature, the tip was maintained in contact with sample surface to ensure thermal stability in transition from one indentation to the next at a set-point load of 2μN. The temperature variation during the entire test was within ±0.2K.

3.2 Experimental results

3.2.1 Nanoindentation tests at room temperature

Typical load-displacement (*P-h*) curves at shallow indentation are presented in Figure 21(a). Each curve is displaced along the *x*-axis and only the loading portions are shown for clarity. The *P-h* curves are from three different grains and they represent the general trend that is observed for all other grains. These *P-h* curves are noted to exhibit a displacement burst (or pop-in) at nearly constant load. The deformation before pop-in is elastic, as confirmed by a reversible loading-unloading behavior slightly below the pop-in

load, and can be described by Hertzian elastic theory[88]. According to the theory, the elastic response from the sample surface by a spherical contact follows the relationship:

$$P = \frac{4}{3} E_r R^{1/2} h^{3/2} \tag{3.1}$$

where P is the applied indenting load, R the tip radius of the indenter, h the penetration depth measured from the sample free surface up to the bottom of the contact and E_r, the reduced modulus of indenter-sample combination, which is derived from the equation[89]:

$$\frac{1}{E_r} = \frac{1-\nu_i^2}{E_i} + \frac{1-\nu_s^2}{E_s} \tag{3.2}$$

Here ν_i (= 0.07) and E_i (= 1,141GPa) are the Young's modulus and Poisson ratio of the diamond indenter, ν_s, E_s are the Poisson ratio and Young's modulus of the alloy sample, respectively. The Hertzian fitting in equation(3.1) for one of the representative curves in Figure 21(a) is shown in Figure 21(b) which gives a fitting coefficient of 3.65 and a corresponding reduced modulus of 179GPa.

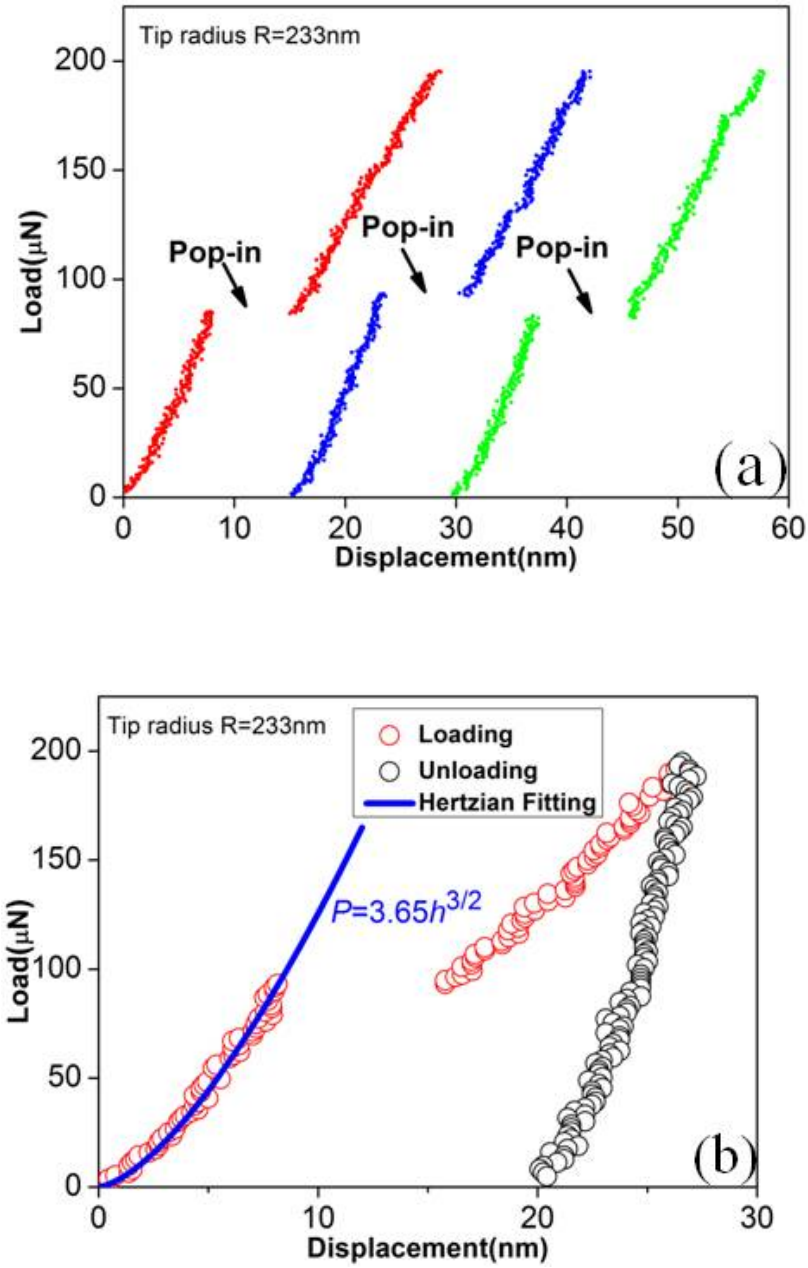

Figure 21 (a) Typical load-displacement (*P-h*) curves from 3 different grains. Curves are offset from the origin for clear viewing. The pop-in events are marked by the black arrows and (b) Hertzian fitting by equation (3.1)for one of *P-h* curves from (a) yields a fitting coefficient 3.65 and a reduced modulus of 179GPa.

An alternative method to obtain the reduced modulus is through statistical fitting. In this case, a collection of *P-h* pairs at the pop-in of 120 indentations from a single grain

(grain # 10) are compiled in a P-$h^{3/2}$ plot, according to equation(3.1), as shown in Figure 22. As indicated in the figure, the pop-in load ranges within 50-110μN and pop-in depth within 6.2-9.6nm. The slope of the red curve in Figure 22 yields a fitting constant of 3.70. Given the radius R, the reduced modulus was readily calculated through equation (3.1) as 182GPa, which is quite consistent with the value of 179GPa estimated from the individual curve in Figure 21(b). Similar procedures were also carried out on other 10 grains we randomly selected for nanoindentation measurements and the resultant fitting constants are listed in Table 6. A comparison between the statistical fitting constant, a_1, and the average constant from the 120 individual fittings, a_2, for each grain is shown in Table 6; the two methods essentially produce consistent results.

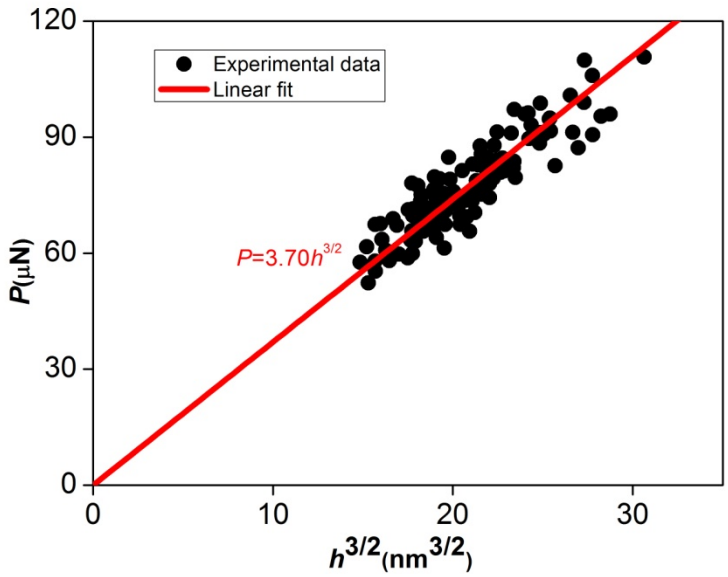

Figure 22 Statistics of 120 P-$h^{3/2}$ pairs at pop-in. The fitting yields a fitting coefficient 3.70 and a reduced modulus of 182GPa.

Table 6 Comparison between statistically fitting constant a_1 as graphically shown in Figure 22 and a_2 obtained from individual fitting as shown in Figure 21(b) for 11 different grains.

Grain#	1	2	3	4	5	6	7	8	9	10	11	Ave.
a_1	3.13	3.22	3.12	3.01	3.14	3.46	3.64	3.72	3.45	3.70	3.50	3.36
a_2	3.19	3.31	3.26	3.15	3.24	3.48	3.72	3.71	3.50	3.73	3.53	3.44

With the reduced modulus obtained from each grain, the maximum shear stress can be subsequently calculated using equations[90]:

$$p_m = \left(\frac{6PE_r^{\,2}}{\pi^3 R^2} \right)^{1/3} \tag{3.3}$$

$$\tau_{\max} = 0.31 p_m \tag{3.4}$$

Here p_m is the mean pressure at the pop-in and τ_{max} is the maximum shear stress that is located directly beneath the bottom of the contact at a depth of 0.48 of the contact radius. The maximum shear stress (τ_{max}) at the pop-in in Figure 21b was thus calculated as 5.6GPa, which corresponds to 0.075μ, where μ is the shear modulus of the alloy (~74GPa). (Note: μ is not available for the FeCoCrMnNi alloy and we estimate it from the Young's modulus and a Poisson ratio of 0.3, an isotropic solid being assumed.)

Performing the above procedure over the remaining 119 indentations on grain #10, the cumulative probability of pop-in events as a function of normalized shear stress is plotted in

Figure 23(a); the maximum shear stress is in the range of 1/14~1/11μ. Extending experiments and the analysis to other grains, a plot of cumulative probability of pop-ins for all 11 grains is presented in

Figure 23(b).

Figure 23 shows that there is little difference from grain to grain and the normalized shear stress for the onset of plasticity ranges within 1/15~1/10μ. Given that all test conditions are identical, the result suggests that there is only slight crystalline anisotropy in the current alloy.

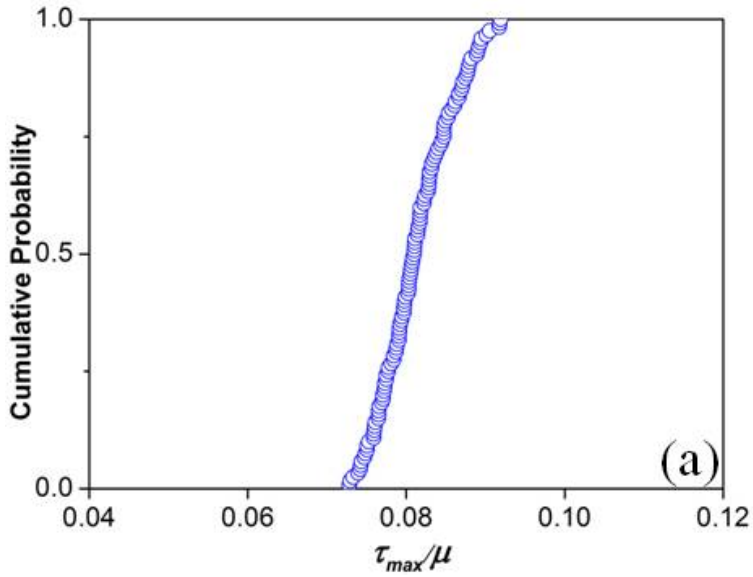

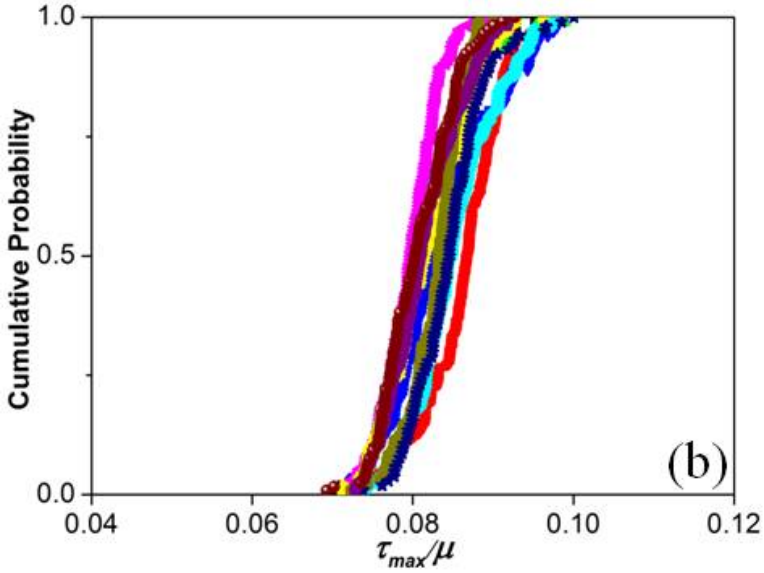

Figure 23 (a) The plot of cumulative probability of pop-in versus normalized shear stress shows that the shear stress for onset of yielding is in the range of 1/14~1/11μ,

where μ is the shear modulus of the sample, and (b) A similar plot for all grains shows little difference and the normalized shear stress ranges within 1/15~1/10μ.

3.2.2 Nanoindentation tests at elevated temperatures

Prior to high temperature testing, we conducted a series of experiments at room temperature to evaluate the rate dependence on pop-in load at loading rates from 25 to 2500 μN/s. The data was then analyzed following the methodology proposed by Schuh *et al*[55, 56]. In the analysis, the cumulative probability, *F(P)*, is correlated with the indentation pop-in load, *P*, via an equation:

$$\ln[-\ln(1-F)] = \alpha P^{1/3} + \beta \tag{3.5}$$

where the parameter β is a weak function of the pop-in load *P* as compared to the first term on the right-hand side in the equation. The parameter α in the above equation is correlated with the activation volume *V* through:

$$V = \frac{\pi}{0.47}\left(\frac{3R}{4E_r}\right)^{2/3} kT \cdot \alpha \tag{3.6}$$

By plotting $\ln[-\ln(1-F)]$ versus $P^{1/3}$, as shown in Figure 24, experimental data are found to fall onto approximately linear lines for datum sets acquired at three different loading rates. The slope of the fitted curve determines α, from which the activation volume value of 34±7 Å^3 is deduced following equation(3.6). The current alloy has an FCC-crystal structure with a lattice parameter of 3.61 Å (

Figure 20b), thus, *V* is about 3/4 volume of a unit cell, or, the activation volume contains 3 atoms ($V \approx 0.75a^3 = 3\Omega$, Ω being the atomic volume).

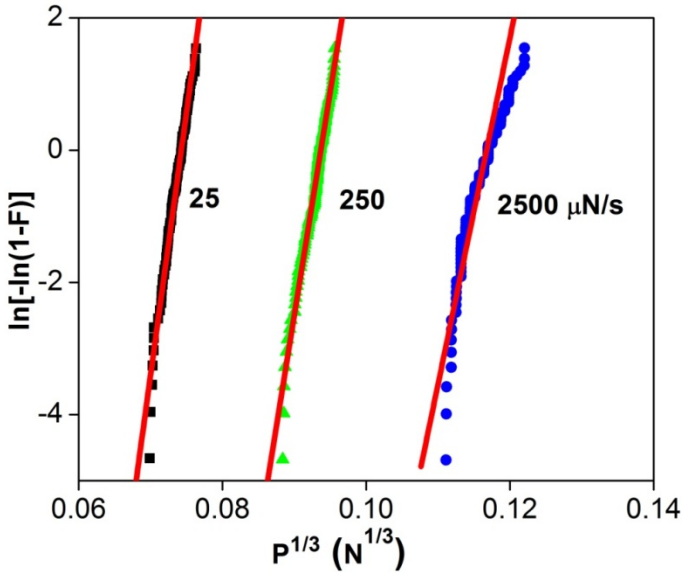

Figure 24 Extracting the activation volume from experimental data using equation(3.5). Experimental data are obtained from 120 datum points for each loading rate at 22˚C. The solid lines in red are the best linear fits.

High-temperature nanoindentation tests were conducted with a blunt Berkovich tip (R = = 638nm). The typical P-h curves obtained at four different temperatures are shown in

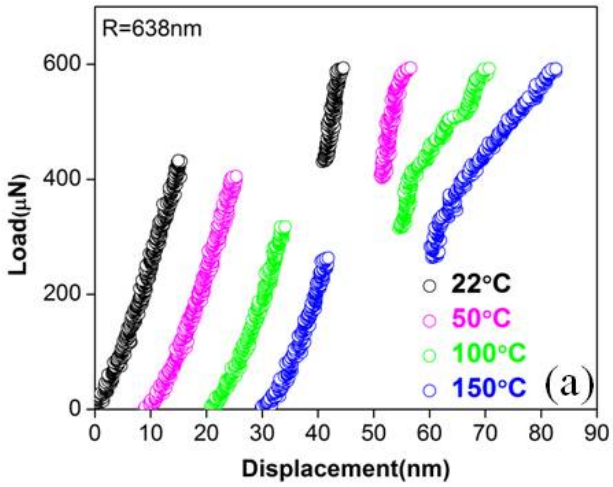

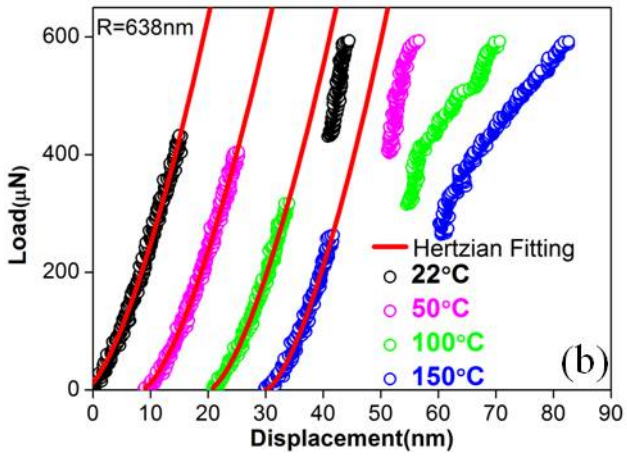

Figure 25a. A significant decrease in pop-in load is observed as the temperature increases from 22 to 150˚C. The average pop-in loads are 423±19, 390±18, 306±18 and 260±25 μN at temperatures of 22, 50, 100 and 150˚C, respectively; the pop-in load drops nearly 30% from 22 to 150˚C. The load-displacement curve prior to pop-in for four temperatures fits well with Hertzian equation and the fittings are depicted in

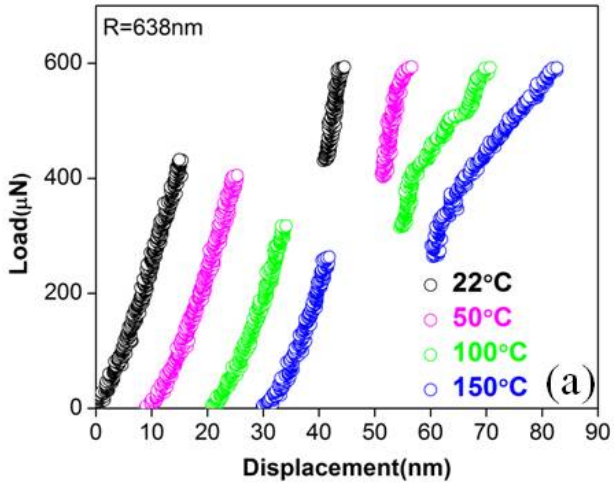

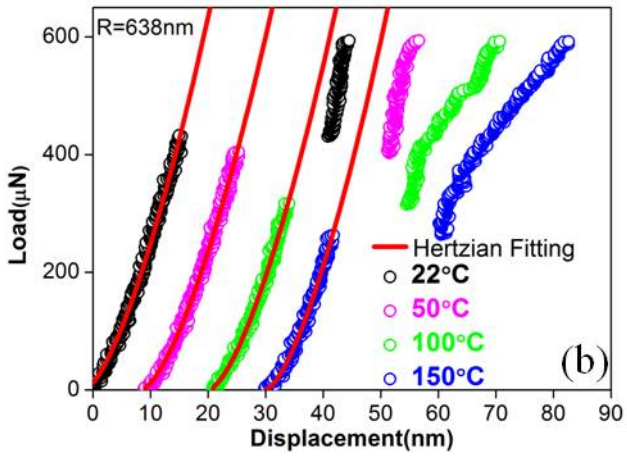

Figure 25b. Based on the fitting, the reduced modulus at 22, 50, 100 and 150˚C are calculated to be 184, 181, 180, and 178GPa, respectively, exhibiting a slight decrease with increasing temperature. These load-temperature data are subsequently used for extracting the activation enthalpy.

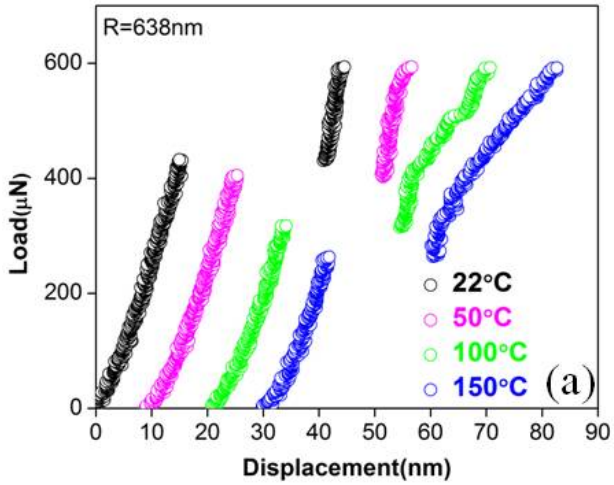

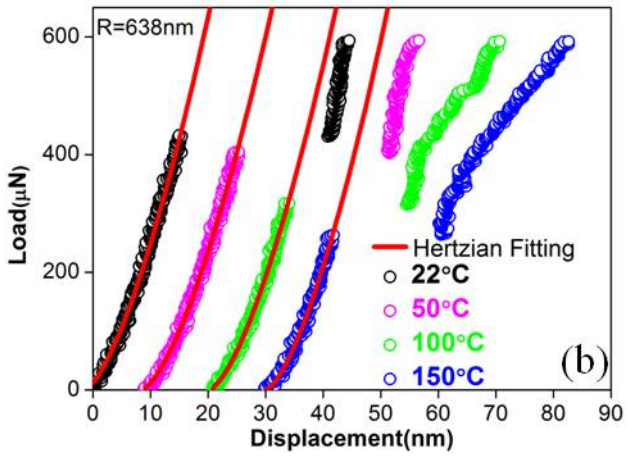

Figure 25(a) Typical *P-h* curves at temperatures of 22, 50, 100 and 150˚C. The average load at pop-in drops nearly one third as the temperature increases from 22 to 150˚C, and (b) Hertzian fitting curves for the four temperatures are shown.

We, again, adopted the method developed by Mason *et al*[55]. Temperature and the pop-in load at a specific *F(P)* are accordingly correlated through an equation:

$$P^{1/3} = \gamma kT + \frac{\pi}{0.47}\left(\frac{3R}{4E_r}\right)^{2/3}\frac{H}{V} \qquad (3.7)$$

where γ is a complex function whose form is not of particular importance and H is the activation enthalpy. The fitting of experimental data is presented in Figure 26 (The detail to construct such a plot is referred to Ref.[55]) whose intercept with the vertical axis determines the ratio of *H/V*. With this intercept and the activation volume V measured from equation(3.6), we now obtain a value of 1.72±0.35eV for the activation energy H.

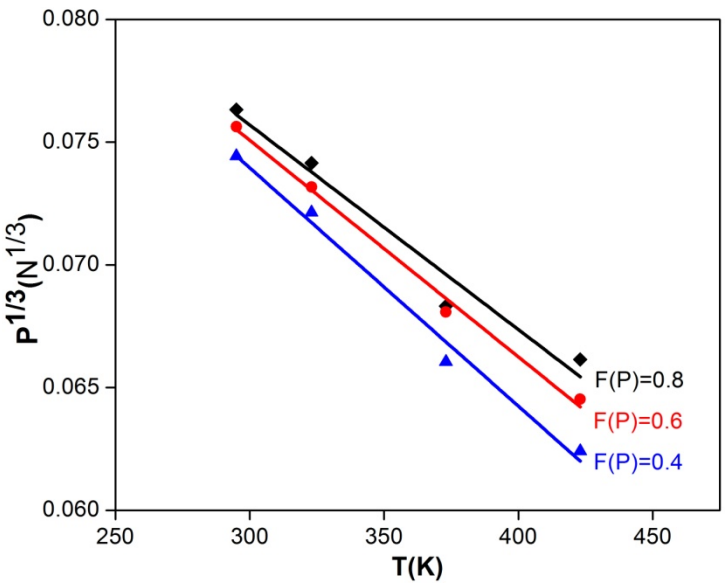

Figure 26 Graphical demonstration of equation (3.7) to extract the activation enthalpy for the pop-in. The three fitted lines converged at T=0K to a common y intercept ($0.101\pm0.001N^{1/3}$), which is scaled with enthalpy *H* via equation(3.7)

3.3 Analysis and modeling

3.3.1 Effect of surface oxide

It has been recognized that pop-in can be triggered by the breakthrough of a passivated passivated thin oxide layer on the sample surface [91-93]. In such a case, the pop-in depth at high temperatures would be larger than that at low temperatures since a higher temperature exposure would enhance more oxidization. In addition, in the current study, samples were held at the test temperature for more than 60 minutes before testing to ensure the thermal equilibrium. However, as indicated in

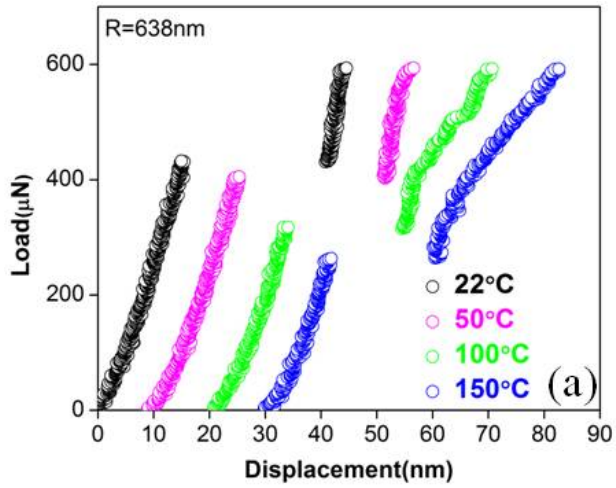

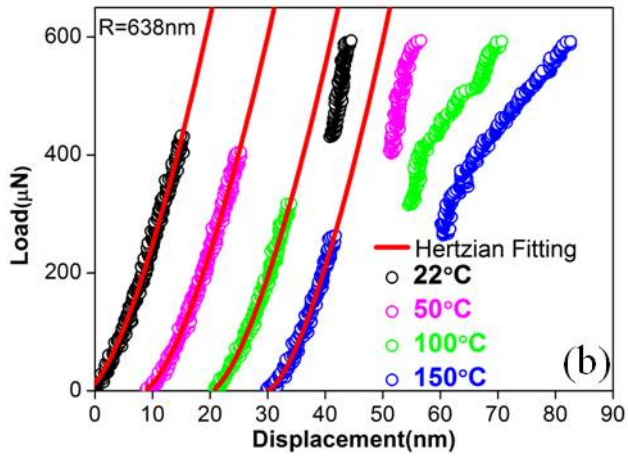

Figure 25, the pop-in depth obviously decreases with increasing temperatures and, specifically, the average pop-in depth at 150˚C is about 3nm shallower than that measured at room temperature. We can, therefore, conclude that our observed pop-in is not caused by the breakthrough of oxide film but an intrinsic behavior of the material.

There are other theories on the nature of incipient plasticity. In the following, we will conduct both qualitative and quantitative assessments of these theories on the basis of our experimental findings, and evaluate their applicability.

3.3.2 Homogenous dislocation nucleation

It has been suggested that the very first pop-in during nanoindentation is associated with the homogenous dislocation nucleation mechanism [54, 62-64, 94-96]. According to

this view, the pop-in would involve a cooperative motion of many atoms to form the critical-sized dislocation loop and, consequently, the activation energy would be on the order of several eV (electronic volt) or even higher [97-100]. A large value of activation energy would minimize the possibility of dislocation nucleation assisted by thermal fluctuation, especially at a temperature as low as 0.2~0.3T_m used in the present study. This seems to contradict to our experimental observation, namely, there is a strong temperature dependence of the pop-in load. To further elucidate this conclusion, we carry out a quantitative evaluation of the homogeneous dislocation nucleation model and compare it with our experimental results.

The homogenous dislocation nucleation model was initially proposed by Hirth and Lothe[101] and recently extended by Michalske *et al*[99]. In the model, Gibbs free energy at 0K for formation of a dislocation loop in the presence of applied shear stress is expressed as:

$$\Delta G = 2\pi r W - \pi r^2 b \tau_a \qquad (3.8)$$

where r, W and b are, respectively, the radius , the line energy and the Burgers vector of the loop, τ_a the applied shear stress acting on the slip plane where the dislocation loop forms. The first term on the right hand side of the equation is the formation energy of a loop and the second term gives the external work done by the applied shear stress τ_a. Here, we exclude the stacking fault energy appearing in the original equation since it is relatively small[99] in comparison with the formation energy. The line energy W, resulting from the lattice strain in the vicinity of dislocation boundary is:

$$W = \frac{2-\nu}{2(1-\nu)} \cdot \frac{\mu b^2}{4\pi} \cdot (\ln \frac{4r}{r_o} - 2) \qquad (3.9)$$

where ν is the Poisson ratio, μ is the shear modulus, r_o is the dislocation core radius approximately equal to Burgers vector b.

To form a loop with the critical radius r_c, two criteria must be met: the formation energy is completely provided by the external work at 0K and the applied shear stress τ_a reaches a critical value τ_c:

$$\tau_c = \frac{\mu b}{2\pi r_c} \tag{3.10}$$

τ_c is the resolved shear stress of τ_{max} on the active slip system and usually taken as half of τ_{max} [98]whose value at 0K can be extrapolated from that of high temperatures (Figure 27). From equation (3.4) and with P as the averaged pop-in load, τ_{max} is computed as 5.85, 5.64, 5.18, and 4.90GPa at 22, 50, 100 and 150˚C, respectively. The variation of τ_{max} with respect to temperature is plotted in Figure 27. The fitted line intercepts with the vertical axis (at 0K) at 8GPa, or 1/9.25μ, which is the ideal shear strength of the alloy at 0K (in the absence of thermal energy) assuming the modulus remains as a constant at low temperatures.

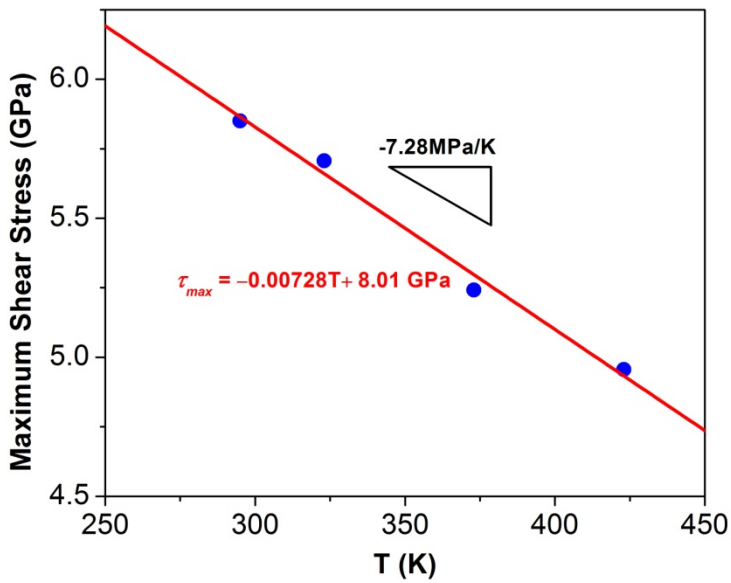

Figure 27 The variation of maximum shear stress versus temperature, giving an intercept with vertical axis at 8GPa (extrapolation), which is the strength of the alloy at 0K at the onset of plasticity.

As $\tau_c \sim 0.5\tau_{max}$, according to equation(3.10) , we obtain $r_c \approx 3b$. After substituting r_c into equations (3.8)and(3.9), the formation energy at 0K in the absence of stress is calculated to be 8.5eV, which substantially exceeds our experimental value of 1.72eV.

The Gibbs free energy at finite temperature, for instance, at RT can be also estimated by equations (3.8),(3.9) and (3.10), given the experimental measured value $\tau_c = \mu/27$. The ΔG is calculated to be 5eV (~196kT), which is well beyond thermal fluctuation and, as a result, temperature within our testing range would essentially had no effect on the pop-in behavior. The above calculation excludes, again, the homogeneous dislocation nucleation as the possible mechanism.

3.3.3 Vacancy-mediated heterogeneous dislocation nucleation

Both activation enthalpy H and activation volume V are indicative of the atomic event. The fact that an activation volume is on the order of 3Ω suggests a vacancy or vacancy cluster related process as the rate limiter for the onset of yielding. Several authors [102-104] have proposed that vacancies, if supersaturated in a solution, might form clusters and then collapse to make dislocation loops. For example, Davis and Hirth[103] applied this theory to Al and found the external stress enhanced the nucleation rate and the stress required must be on the order of magnitude as the theoretical strength ($\mu/2\pi$) in order to produce a discernible nucleation rate. Mason *et al*[55] also discussed the possibility of vacancy-related nucleation in single crystal Pt since the activation volume was measured as small as $0.5b^3$; however, they questioned this view because the experimentally measured activation enthalpy (~0.28eV) was too low compared to the vacancy migration energy (~1.5eV).

According to the transition-state theory[105, 106], the nucleation rate at which the critical event (for example, formation of the critical nucleus) occurs is governed by Gibbs free energy:

$$n_c = n_0 \nu \exp(-\frac{\Delta G}{kT}) \tag{3.11}$$

and

$$\Delta G = H - \tau \cdot V \tag{3.12}$$

where n_0 is available vacancy sites in the stressed volume, ν the pre-exponential attempting frequency factor on the order of Debye frequency, H is the activation enthalpy or activation energy, τ the applied shear stress, V the activation volume. ΔG is also scaled with kT[74] and can be written as:

$$\Delta G = \lambda kT \tag{3.13}$$

with λ as the scaling coefficient. The n_0 in equation (3.11) can be estimated in the following way. The vacancy concentration at thermal equilibrium at room temperature is assumed to be 10^{-6} [107]and the stressed volume is scaled with the contact radius a by Ka^3, where K approximates to be π[55]. The vacancy sites n_0 is, then, expressed as:

$$n_0 = 4 \cdot (\frac{\pi a^3}{a_0^{\ 3}}) \cdot 10^{-6} \tag{3.14}$$

where a_0 is the lattice parameter, 4 represents the number of atoms in a FCC unit cell, and $4(\pi a^3 / a_0^{\ 3})$ includes all atom sites in the stressed volume. According to Hertz theory, the contact radius can be estimated as:

$$a = \sqrt{h \cdot R} \tag{3.15}$$

where h is the pop-in depth and R the tip radius. Combining equations(3.14) and (3.15) , n_0 is estimated on the order of 100 sites in the stressed volume.

Now, let us examine H and V in equation (3.12) in details. Assuming H and V are independent of temperature and stress, it is noted that the value of λ in equation(3.13) must be smaller than 40 for if it is larger than 40 the exp (-40) would be on the order of 10^{-18}, which even by multiplying ν (~10^{13}) would make the nucleation events (i.e., pop-in) unobservable. Setting σ equal to the maximum shear stress at the four temperatures and inserting the measured H and V values into equation(3.12), λ is calculated through equation (3.13) to be 17.5, 17.8, 18.5 and 18 at 22, 50, 100 and 150˚C, respectively. These λ values are reasonable since ΔG, the energy barrier for forming a critical-sized nucleus, is now possible to attain from the thermal fluctuation. Combining equations (3.12) and (3.13), and the stress-temperature correlation can be expressed as:

$$\tau = -\frac{\lambda k}{V}T + \frac{H}{V} \tag{3.16}$$

Substitute the average λ = 18 into equation(3.16), the following equation is readily obtained:

$$\tau = -0.00716T + 7.93\,(\text{GPa}) \tag{3.17}$$

which is in excellent agreement with our experimental data in Figure 27 suggesting the robustness of the measured H and V.

In the case of vacancy-mediated nucleation, the activation energy is the vacancy migration energy F_{m} and the stress bias responsible for migration would be the pressure gradient, $\nabla\sigma_p$ under the indenter, equation (3.11) is therefore transformed to

$$n_c = n_0 v \exp(-\frac{F_m - \left|\nabla\sigma_p\right| bV}{kT}) \tag{3.18}$$

F_m is not available for high-entropy alloys. However, the migration energies for FCC metals such as Cu, Ag, Au, Ni, Pd and Pt are found to be 1.3, 1.1, 0.9, 1.6, 1.4 and 1.5eV, respectively[108]. Our measured F_m = 1.72eV for the current FCC FeCoCrMnNi falls in the right range, except it is slightly larger.

The FCC crystal structure in high-entropy alloys is noted to be somewhat different from that in the conventional FCC alloys[109]. It is distorted because of different sizes as well as chemistry of the constituent atoms. Resulting from the lack of a major diffusing element, vacancy migration in HEAs is expected to involve cooperative motion of several atoms in order to keep proper composition portioning, rather than the conventional one to one atom-vacancy exchange. This collective atomic motion may explain the slightly higher activation enthalpy as compared to that in the conventional FCC metals and an activation volume (~3 atoms) that is larger than a single atomic volume.

3.4 Conclusion

Instrumented nanoindentation experiments were performed on a high-entropy alloy FeCoCrNiMn at different temperatures (22-150ºC) and loading rates (25-2500μN/s) to

examine the nature of incipient yielding. Experimental data were analyzed and further compared with existing models for dislocation nucleation. The following conclusions are drawn.

1. Indentation pop-in, which marks the onset of yielding, is observed at every temperature and loading rate conducted in this study.

2. The observed pop-in phenomenon is not caused by the breakthrough of the oxide layer of the surface but an intrinsic behavior of the material.

3. The maximum shear stress required to induce incipient plasticity is about 1/10~1/15μ, where μ is the shear modulus of the alloy, and appears to have only slight dependence of the grain orientation.

4. The pop-in load decreases with increasing temperature and is a strong function of temperature; it drops about 30% from 22 to 150ºC.

5. The extracted activation energy and volume for the onset of plasticity are 1.72eV and 34±7Å^3, respectively. Both values favor a vacancy or vacancy like mediated heterogeneous dislocation nucleation as the mechanism for the onset of plasticity.

6. The higher activation energy and volume in the current FeCoCrNiMn alloy in comparison with that obtained from conventional FCC metals suggest that vacancy migration in high entropy alloys is not a traditional process of direct atom-vacancy exchange, but involves the cooperative motion of several atoms.

4 Time Dependence of Incipient Plasticity

4.1 Introduction

Following the preceding chapter where we have shown that the vacancy-mediated process seems to dominate the dislocation nucleation during pop-in, this chapter aims to address the issue related to one of central properties of the vacancy: its migration. The vacancy would move under the applied stress even when it is below the critical stress to trigger spontaneous pop-in, which would introduce time effect into the nucleation. The above argument naturally leads to this question: given appropriate waiting time, would pop-in still show up when the sample under indentation is subject to a constant load below the critical level that prompts spontaneous pop-in?

Although there are numerous reports on pop-in as already mentioned, only limited results have been reported of delayed pop-in below the critical load at which instantaneous pop-in occurred [98, 110-112]. Ngan AHW *et al* [98, 110, 112] reported the time dependent incipient plasticity on single crystal Ni_3Al. They found that the waiting time increases with a decreasing load and upon to a level the delayed pop-in wouldn't be observed. The result is shown in Figure 28. They proposed qualitatively that a stable dislocation loop was formed at the below critical load and it expanded through climbing by acting as a sink for absorption of vacancy which is driven by the high compressive hydrostatic pressure imposed by the indenter. They later[113] also elaborated on the climbing quantitatively and established a model based on a creep model proposed by Li *et al*[114].

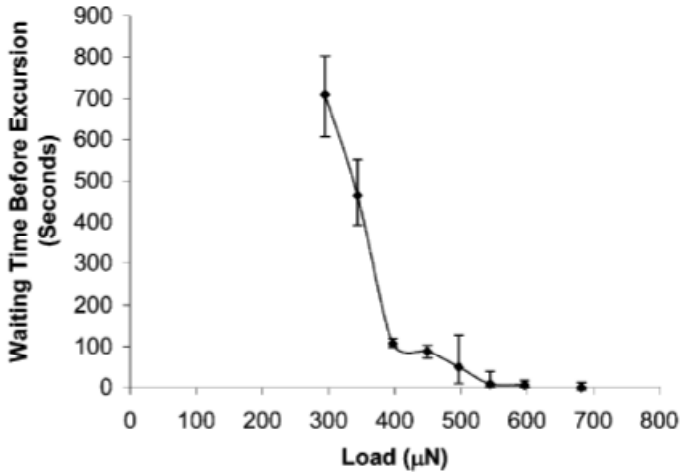

Figure 28 Time dependence of pop-in during indentation on single crystal Ni_3Al. The holding time prior to pop-in decreases with increasing loading, until above 600 μN pop-in occurred spontaneously. At the largest holding load, i.e. 700 μN in this figure, pop-in occurs spontaneously before reaching the holding load. (Error bars show the scatter of typically five measurements.)[98]

Bahr DF [111]also showed that in single crystal Fe-3%Si displacement burst would occur after being hold at an elastic load for certain period of time. The time period between the beginning of the hold segment and the yielding point (i.e., pop-in or displacement excursion) was measured and presented in Figure 29. Same is the observation with that of Ngan AHW[98] that a threshold load is required in order for delayed pop-in to happen. However, the waiting time in Fe-3%Si doesn't obey a trend in Figure 28 of Ni_3Al. The time has a huge variation which is even greater than the mean value itself.

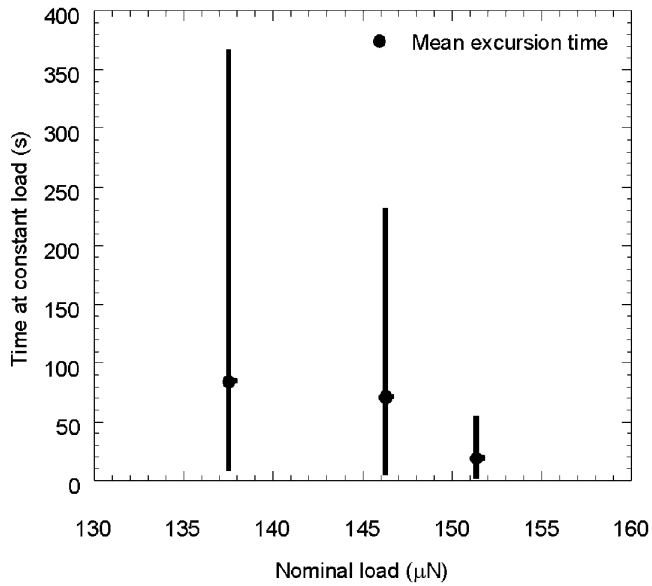

Figure 29 The mean values of the waiting time before pop-in as a function of applied constant load in single crystal Fe-3%Si. After 600 s at a constant load of 125 mN, no pop-in occurred[111]

4.2 Experimental setup for delayed incipient plasticity study

As we were doing nanoindentation at different temperatures to study thermal effect on pop-in in the previous chapter (i.e., RT, 50˚C, 100˚C and 150˚C), we tentatively performed around 10 tests (as each test at above RT usually takes half an hour, that limits our test times each day) at each load for a fixed temperature with a loading profile consisting of loading, holding and unloading, which is schematically shown below:

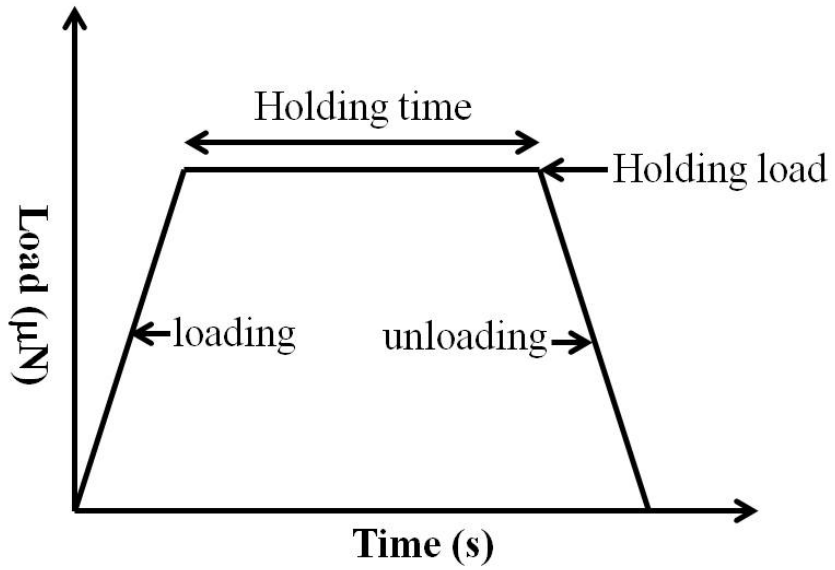

Figure 30 Schematic illustration of loading function in studying the delayed plasticity

The duration of the test is mainly limited by the machine's thermal drift. For Hysitron Triboindenter used in this study, in minimizing the effect of thermal drift, the test is advised to run no more than 60s, so the maximum holding time usually can sustain 50s(loading and unloading normally take 5s each). And to show delayed incipient plasticity, the holding load is somewhere below the mean load for spontaneous pop-in. We select several holding load levels to examine the dependence of waiting time on stress.

For instance, the average load at pop-in at RT for 121 indentations is 420uN, we chose five holding loads: 320, 280, 240,200 and 160 μN. For 8 indents at 320 μN, one exhibited complete reversible loading and unloading and 3 has popped in before holding, and 4 have popped-in amid holding. For 8 indents at 280 μN, 7 out of 8 have shown pop-in during holding and 1 was complete elastic. For 240 μN and below, almost all the load-displacement curve doesn't demonstrate pop-in during holding, indicating that there is a threshold stress in germinating pop-in.

4.3 Results: P-h curve and waiting time distribution

Typical load displacement curves at RT are shown in Figure 31. A similar testing procedure was duplicated on samples tested at 50˚C and 100˚C. The constant loads at 50˚C (average pop-in load is 390 μN) are 300, 275, 250, 225 and 200 μN, respectively; loads at 100˚C (average pop-in load is 310 μN) are 275,250,225,200 and 175 μN. Typical curves at 50˚C and 100˚C are illustrated below (Figure 32 and

Figure 33):

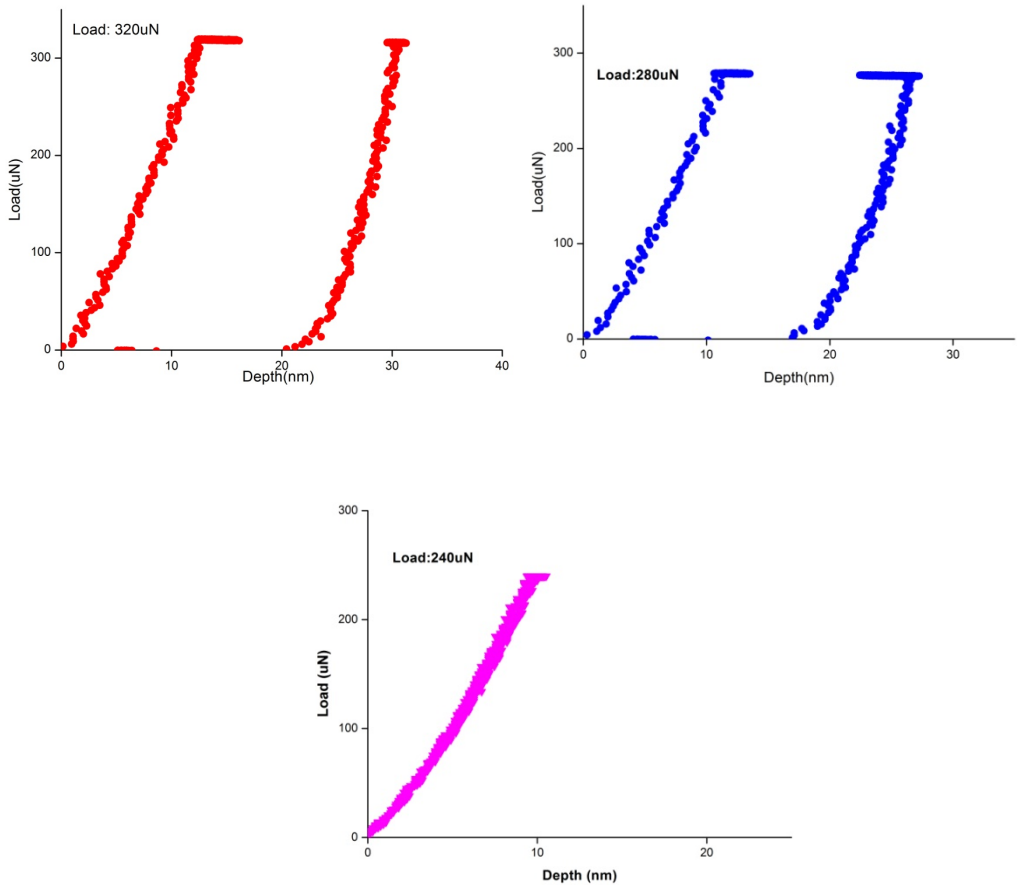

Figure 31 Load-depth profile for RT at holding load (a) 320μN, (b) 280μN (c) 240μN

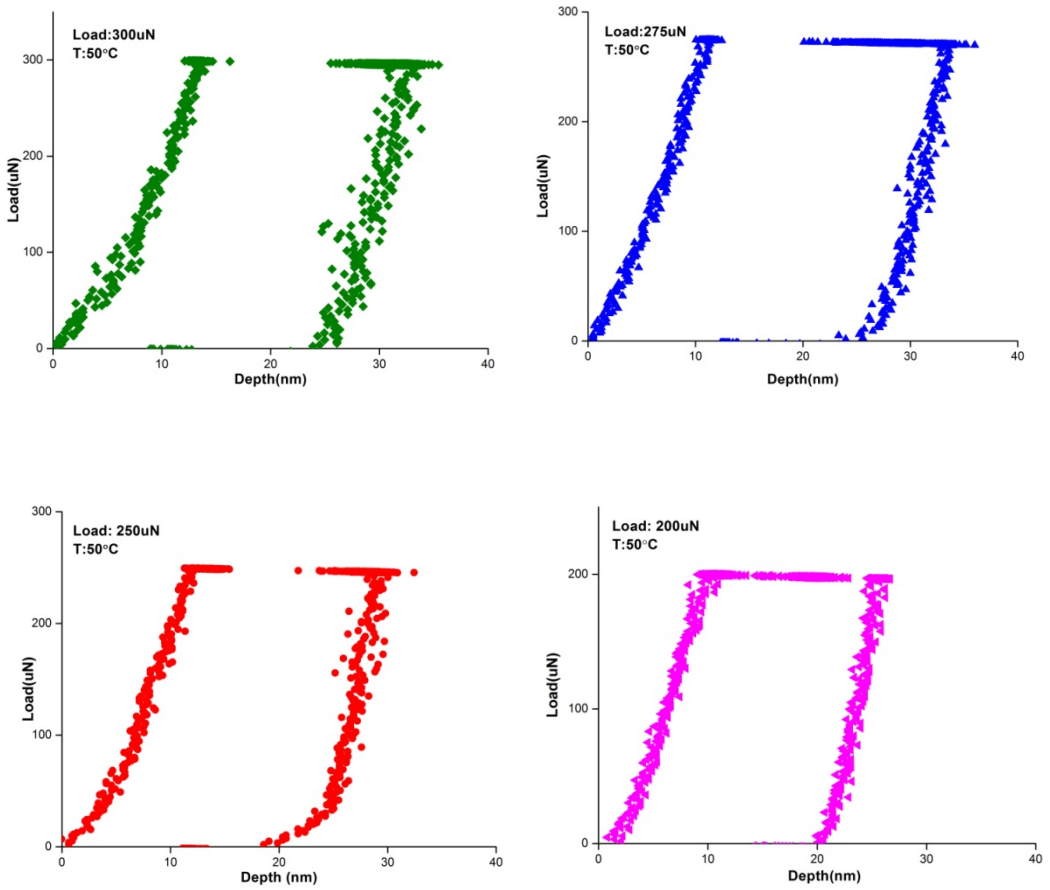

Figure 32 Load-depth profile for 50˚C at holding load (a) 300μN, (b) 275 μN, (c) 250 μN (d) 200 μN

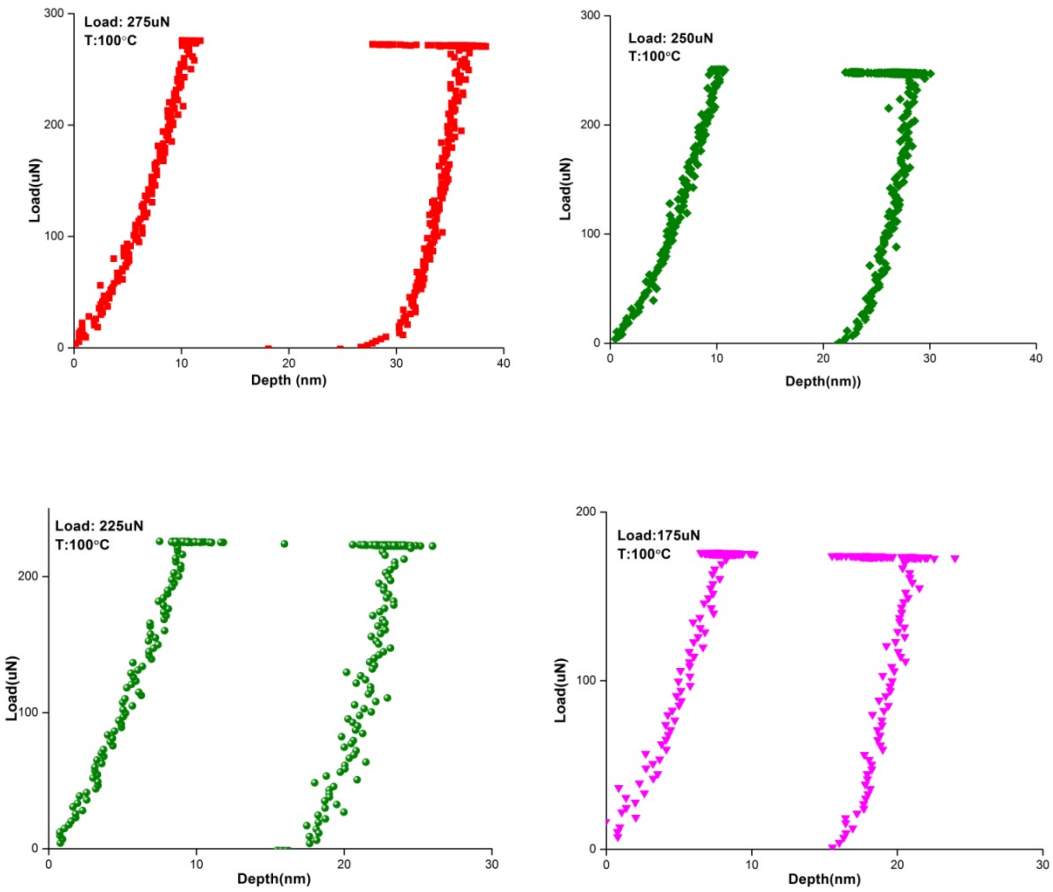

Figure 33 Load-depth profile for 100˚C at holding load (a) 275μN, (b) 250 μN (c) 225 μN and (d) 175 μN

As the pop-in is associated with dislocation nucleation, the waiting time is termed as "incubation time" for critical dislocation loop to form. The incubation time for those which have shown displacement burst at RT is shown in Table 7. The waiting time at 50˚C and 100˚C are also compiled in Table 8 and Table 9, respectively.

Table 7 Incubation time (s) for (a) load at 320 μN at RT and (b) load at 280μN

Time(s)	48.2	11.5	35.8	2.8
Load (μN)	320	320	320	320

Time(s)	33.8	0.14	40.2	8.1	1.9	15.8	0.1
Load(μN)	280	280	280	280	280	280	280

Table 8 Incubation time (s) at 50˚C for (a) load at 300 μN, (b) for load at 275 μN, (c) for load at 250 μN and (d) for load at 225 μN

Time(s)	8.7	2.7	1.6	2.8	5.8	0.5	7.7	1.5	10.4
Load(μN)	300	300	300	300	300	300	300	300	300

Time(s)	1.5	0.6	1.8	7.7	0.3	2.6	23.3	3.3	0.05
Load(μN)	275	275	275	275	275	275	275	275	275

Time(s)	21.5	7.2	3.6	4.2	5.8	10.8	1.6	2.9
Load(μN)	250	250	250	250	250	250	250	250

Time(s)	1.3	2.7	1.95	5.06
Load(μN)	225	225	225	225

Table 9 Incubation time (s) at 100˚C for (a) load at 275 μN (b) load at 250 μN and (c) load at 225 μN

Time(s)	2.08	7	2.27	0.99	7.8	4.3	3.13	0.9
Load(μN)	275	275	275	275	275	275	275	275

Time(s)	6.4	6.06	7.96	1.06	2.23	5.27	5.17
Load(μN)	250	250	250	250	250	250	250

Time(s)	28.95	26.4	8.68	3.0	21.35	7.22	7.4	0.33	9.85	0.4
Load(μN)	225	225	225	225	225	225	225	225	225	225

From the testing results at different loads and temperatures, the incubation time variation didn't show an expected trend: it should decrease with increasing temperature if the ratio of the applied load to the average load is fixed, and with decreasing applied loads at a fixed temperature, or vice versa. The waiting time is crossing over. As the number of testing here is small, it is necessary to conduct a large number of holding experiments to rely on statistics.

As a first step, we carried out a large number of tests at RT with a different tip radius as the testing at high temperature is not reliable as at RT due to thermal drift. 200 indentations were performed for each fixed load (four constant loads are selected with an incremental of 25μN decrease: with a holding time of 50s and only a portion of them show delayed plasticity, the left indentations either popped-in prior to holding or didn't show any plasticity. In the following, Figure 34 shows the statistics (count versus waiting time) for those present with pop-in during holding.

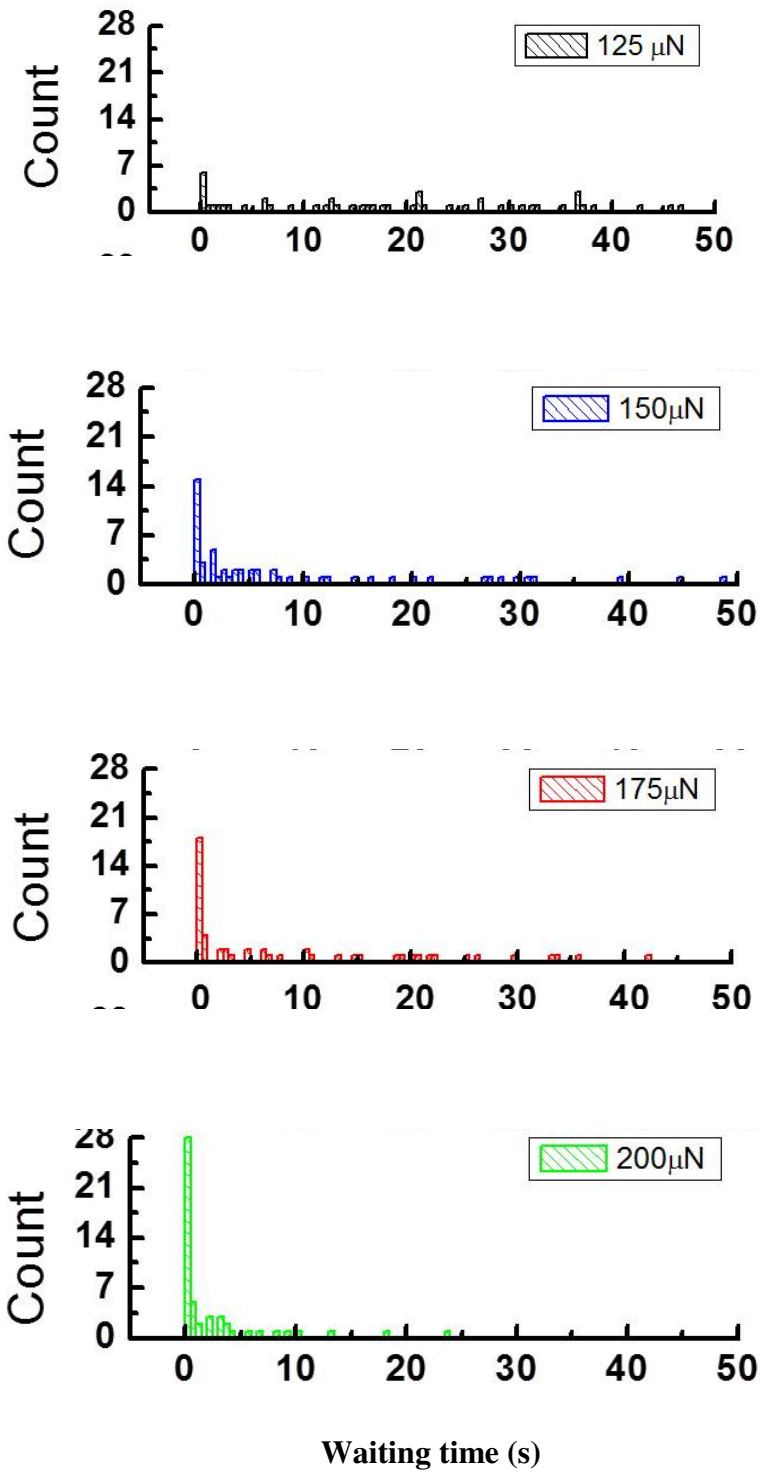

Figure 34 The waiting time histogram for those present with delayed pop-in at holding load (a) 125μN, (b) 150μN, (c) 175uN and (d) load 175uN

4.4 Discussion

4.4.1 Origin of time dependence-transition state theory

According to the transition-state theory[105, 106], the nucleation rate at which the critical event (for example, formation of the critical nucleus) occurs is governed by Gibbs free energy:

$$n_c = n_0 v \exp(-\frac{\Delta G}{kT}) = n_0 v \exp(-\frac{H - \tau \cdot V}{kT}) \quad (4.1)$$

The nucleation time, t_n, is inversely proportional to the nucleation rate

$$t_n \sim \frac{1}{n_c} = n_0 v \exp(\frac{H - \tau \cdot V}{kT}) \quad (4.2)$$

which connects the holding time t_n with stress and temperature, H is taken as the activation enthalpy at 0K (i.e., without the assistance of the thermal fluctuation), then:

$$H = \tau_0 V \quad (4.3)$$

where τ_0 is the maximum shear strength at pop-in at zero temperature which can be extrapolated, as done in Figure 27, from maximum shear strength at different temperatures above 0K. So equation(4.2) changes to

$$t_n = n_0 v \exp(\frac{\tau_0 \cdot V - \tau \cdot V}{kT}) \quad (4.4)$$

where τ is related to pop-in load through equation (3.3) and equation(3.4). Thus equation(4.4) can further be rewritten as:

$$t_n = \frac{1}{n_0 v} \exp\left\{0.31\left(\frac{6E_r^{\,2}}{\pi^3 R^2}\right)^{1/3} \cdot \frac{V}{kT} \cdot (P_0^{1/3} - P^{1/3})\right\} \quad (4.5)$$

Where P is the pop-in load at T and P_0 is the pop-in load at 0K. Therefore, a plot (Figure 35) of natural logarithmic of t_n (the mean waiting time or incubation time) against $P^{1/3}$ could give the value of V, which can be compared with that obtained from nanoindentation tests at Chapter 3.

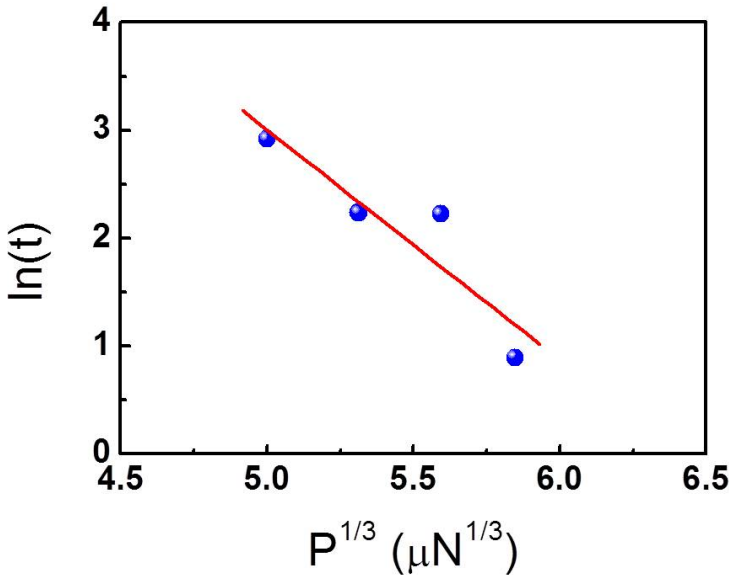

Figure 35 Natural logarithmic of incubation time versus $P^{1/3}$ according to equation(4.5). The slope can be used to calculate the activation volume which can be further compared to that derived at Chapter 3.

However, a closer examination of waiting time reveals the waiting time is so scattering that even within one set of test the maximum sometimes is more than one hundred the minimum one, which is similar to the result reported on Fe-3%Si[111]. There is also too much waiting time crossover under decreasing holding load at a fixed temperature which should be, according to equation(4.5), one to one corresponding between the load and the waiting time. In this case the mean value of waiting time would be too comprehensive an indicator to decisively and quickly determine the undergoing physical process. Many unaccounted, complicated factors may influence the mean value such as the distribution of vacancy population beneath the indenter, vacancy random walk pattern under stress gradient and their variation with the indentation location which is impossible to measure experimentally. We, therefore, put aside the above transition state model that attempted to rationalize the waiting time patterns as shown in Figure 34. Instead, in what follows we will direct our efforts towards other experimental evidence to establish the mechanism the dislocation loop adopted to expand during the elastic holding as a first essential, simple step to approach the time-dependent incipient plasticity.

When a stress lower than that for instantaneous pop-in is applied, a loop will be formed in equilibrium with the applied stress with less than the critical radius (the saddle point configuration) [115]. To reach the saddle point when the loop will grow unstably and release the pop-in, the loop has to expand. Two means exist that a loop can adopt to enlarge with time: by acting as the sink of vacancy flux or by coherently fluctuating with the aid of thermal energy to cause the loop burst. For the vacancy-mediated dislocation loop expansion, there are in the literature numerous reports on the observation of prismatic loops nucleated out of the supersaturated vacancy either resulting from rapid quenching [104, 116-118] or atomic displacements produced by irradiation [119-125]. The loop radius grows continuously with time (Refer to Figure 5 in [122]). For the second loop expansion mechanism, the loop stays at equilibrium configuration for some time until at a moment the loop suddenly bursts. Both mechanisms show time dependence. By drawing an analogy to biology, the former is best described, as "evolution" whereas the latter as "mutation".

4.4.2 Dislocation loop expansion under constant load in HEA

To find out which mechanism is working, it is necessary to generally review the time-dependent activities under indentation. The creep that takes place below the yielding stress essentially resembles the delayed pop-in: time-dependent plasticity under elastic stress. Li *et al*[126] proposed five mechanisms leading to the creep: dislocation glide, power-law creep: climb-plus-glide of dislocations, power-law breakdown: glide-plus-climb of dislocations, indentation creep induced by dislocation climb, and indentation-creep by diffusion. Since the presence of dislocation is prerequisite for dislocation motion, the first four mechanisms wouldn't be applicable as there is no dislocation preexisting before pop-in. The last one becomes the only option, which seems reasonable as it is the only one which has the creep function that varies with the applied load less than yield stress.

In a later paper[114], they elaborated on the last mechanism and proposed that the creep, or increased penetration depth of the indenter under elastic stress, may occur due to chemical potential gradient of the vacancy resulting from the stress fields beneath the indenter. The gradient leads to atoms flowing from the region of high chemical

potential to the surface where the potential is the lowest. The chemical potential contour map beneath the indenter was calculated and the flux of vacancy schematically illustrated in Figure 36:

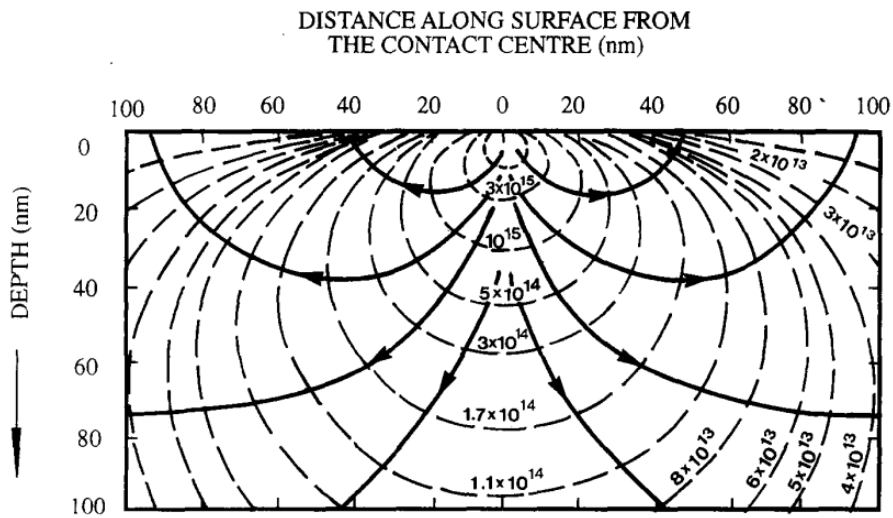

Figure 36 Equi-chemical potential contours (dotted lines). Diffusional flow occurs perpendicular to these contours (solid lines)[114]

They subsequently evaluated the volume (lattice) diffusion and interface (between sample and the indenter) diffusion flowing to the surface and assume the sum of the two completely accountable for the rate of change of the embedded volume of the indenter. The sum diffusion rate (the complete deduction is referred to [114]) is given as:

$$\dot{V} = \dot{V}_v + \dot{V}_i = 2\pi(1+v)\frac{PD_v\Omega}{akT}\left[1+\frac{3\pi}{8}\frac{\delta}{a}\frac{D_i}{D_v}\right] \tag{4.6}$$

Where v is the passion ratio, P is the applied load, D_v and D_i are the volume and interface diffusivity, respectively, a is the contact radius, k is the Boltzmann constant, T is the temperature, Ω is the atomic volume, δ is the thickness of interface. The rate of the change of the embedded volume for a spherical indenter is given by:

$$\dot{V}_e = \pi h(2R-h)\dot{h} \tag{4.7}$$

Equating $\dot{V}_e$ to $\dot{V}$, this yields the creep rate:

$$\dot{h} = \frac{2(1+\nu)}{\pi} \frac{P}{[h(2R-h)]^{3/2}} \frac{D_v \Omega}{kT} \left[1 + \frac{8\delta}{3[h(2R-h)]^{1/2}} \frac{D_i}{D_v} \right] \tag{4.8}$$

which gives the indentation creep at the stage of holding prior to pop-in. They verified the above equation on its applicability to single crystal tungsten creep[127] and found the theoretical prediction from equation (4.8) is in good agreement with the experimental data. One of most important important inferences from equation (4.8) is that if a creep rate is present under purely elastic stress in the period of delay, it will in turn validate the assumption that the dislocation loop growth is controlled by the vacancy diffusion.

Let's examine an example of postponed pop-in in FeCoCrMnNi at RT under elastic load. The load displacement and the corresponding load time profiles are displayed in Figure 37(a) and Figure 37(b), respectively. As indicated by the black circle in Figure 37(a), there is apparent creep showing prior to displacement burst. And the creep displacement time profile in this stage is shown in Figure 38. The displacement was bounded within upper and lower bounds and yet progressed nevertheless in a stair-case pattern. These characteristics are in excellent agreement with the depth-time data in single crystal tungsten.

On the other hand, the parallel and stepwise data stripes in Figure 38 reflect the existence of vacancy motion because the forward and back flow resembles the pattern of the random jump of vacancy under the bias of stress. According to equation(3.10), as the loop expands, the stress needed should increase inversely with the loop curvature, which is not the case here. The stress, as load divided by area, was continuously relaxing as the displacement was increasing. When the displacement is such that the loop finally evolves to the saddle point, and the stress experiences a further sudden drop as indicated by the blue arrow in Figure 37(b). The diminishing applied stress during holding can be rationalized if the line tension of the expanding loop is relieved by the vacancy migrated to the loop with the assistance of stress relieves.

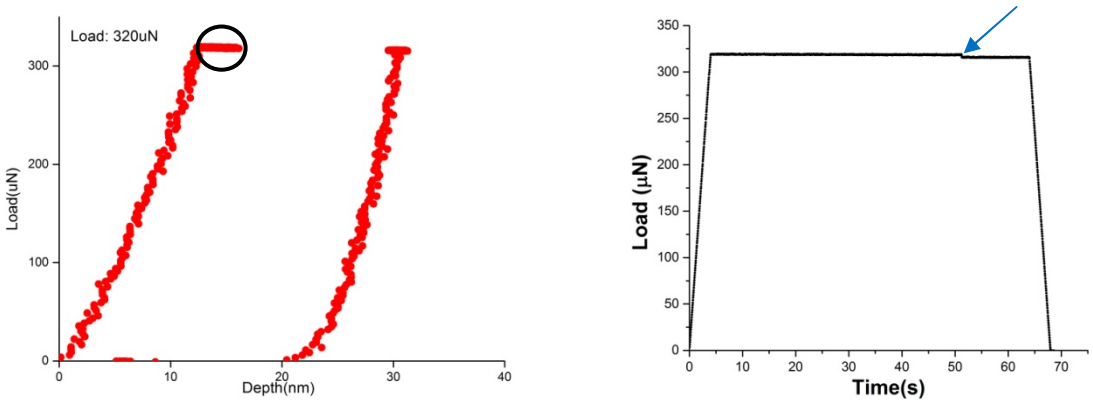

Figure 37(a) Load depth profile under elastic load at RT, and (b) the corresponding load-time relation

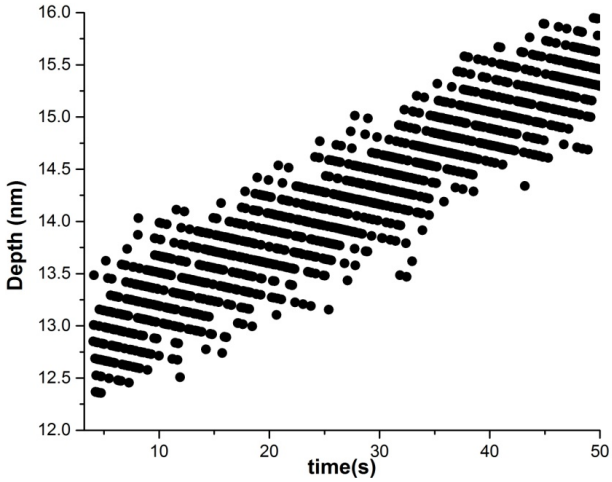

Figure 38 Displacement as a function of time in the stage as indicated by the black circle in Figure 37a prior to pop-in. stepwise proceeding is indicative of the random walk of vacancy motion.

4.4.3 Expansion mode in single crystal Ni - burst with the assistance of thermal fluctuation

For comparison, another FCC metal single crystal Ni was conducted with nanoindentation of the same procedure as on the FeCoCrMnNi. Of 225 nanoindentations, 43 exhibited pop-in during holding, 76 popped-in before holding and 106 showed no pop-in.

Figure 39 represents load-displacement curves of those 43 and Figure 40 shows the waiting time distribution which shows a similar pattern as FeCoCrNiMn. Its origin, however, is different as discussed below.

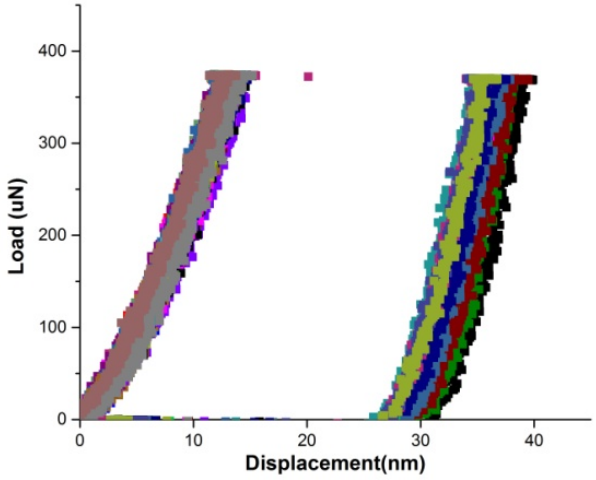

Figure 39 Load-displacement curves for single crystal Ni during holding. No trace of creep was observed after holding began

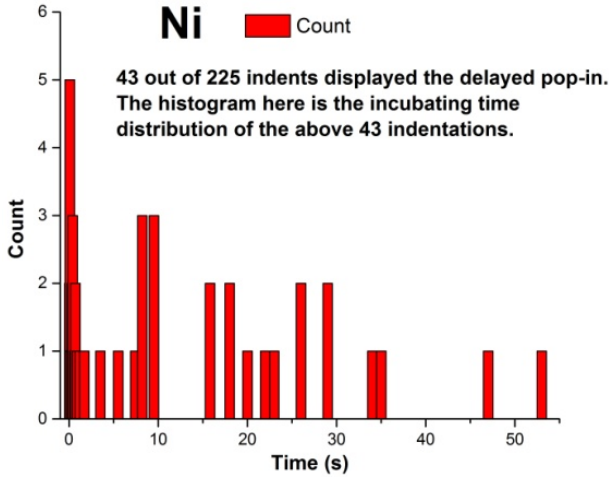

Figure 40 The histogram of waiting time for Ni at RT, which is similar to the pattern observed in FeCoCrMnNi

The displacement curve for Ni in holding stage has no sign of creep which is apparent from the fact that no displacement trail after the commencing of holding is visible as otherwise would be shown as in the black circle in Figure 37. For instance, for a pop-in that occurred after 25s delay, the displacement is still maintained unchanged (

Figure 41). This prompts us to speculate a different picture for loop growth in Ni: the loop may stay still until the moment that the aid of thermal fluctuation is able to surmount the barrier to saddle point and trigger the loop to expand suddenly and coherently

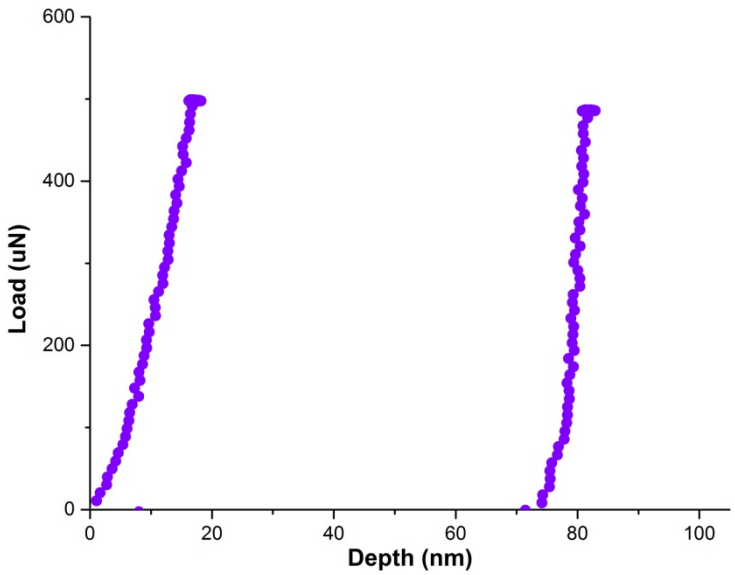

Figure 41 Load depth profile for a pop-in occurring after 25s delay. No creep is observed before pop-in

4.5 Conclusion

Nanoindentation with a loading-holding-unloading profile was employed to study the delayed pop-in in FeCoCrMnNi HEA. Different levels of holding load are selected and we found:

1. The HEA FeCoCrMnNi showed delayed pop-in during holding loads less than the critical level for spontaneous pop-in

2. Observing the delayed pop-in requires a threshold load below which the sample only showed complete elasticity
3. The waiting time didn't follow as-expected trend: the larger the holding load, the less the time needs to wait for the pop-in to come. Instead, the waiting time over crossed and showed two orders of magnitude difference in one set of nanoindentation
4. During holding stage prior to pop-in, creep occurs in FeCoCrMnNi.
5. The creep data is good agreement with the model which proposed the diffusion is responsible for the creep
6. A dislocation loop is instantly formed in equilibrium with the applied stress. In FeCoCrMnNi HEA, it expands by vacancy flowing to the loop.
7. In comparison, delayed pop-in was also observed in single crystal Ni but there is no sign of creep at the holding stage prior to pop-in, which prompts us to speculate that the dislocation loop expands differently: the loop stays at the equilibrium until it bursts over the saddle point with the aid of thermal fluctuation

5 Effect of tip radius on pop-in size

5.1 Introduction and Experimental

Following the Chapter 4, this chapter will deal with another important characteristic associated with the vacancy: its population. We will essentially answer the following question: since vacancy population available beneath the indenter for dislocation nucleation is proportional to the stressed volume, would the pop-in behavior change if the indenter radius changes? By pop-in behavior, we mean if the pop-in size (the magnitude of displacement burst or the number of dislocation nucleated) would vary with tip radius which dictates the stressed volume and in turn the vacancy population contained within. So the question is reduced to: would the pop-in size decrease all the way down to zero as the tip approaches vanishing small and would the pop-in size scale up with the tip radius with no upper limit?

Many previous experimental studies have been focused on the pop-in transition point from elastic to plastic deformation-by studying statistical distribution of load at this point and its dependence on the loading rate[55, 84, 128], orientation[63, 129-132] and temperature[51, 133]. However, the propagation of dislocations after being nucleated, which manifests itself in the displacement burst size, has rarely been discussed. In echo of many reports on the shear stress dependence on tip radius [61, 134, 135], we will explore the tip radius effect (i.e., size effect) on the burst size which is related to the number of dislocation nucleated[136, 137].

In theory, the dislocation loop nuclei can't be smaller than the burgers vector, which impose a lower bound on radius to witness the pop-in. And there is no limit on the upper bound. Therefore, in this line of pursuit, a large variety of radius should be used. We performed Nanoindentation experiments using the same Hysitron Triboindenter (Hysitron, Inc. Minneapolis, MN) and 7 diamond indenter tips across two orders of magnitude with effective radii, R, of, 50, 200, 233, 467, 638, 743 and 2013nm. The tip radius was calibrated using standard procedure. There were at least 25 indentations made for each radius. Each set of indentations (total 6 sets for six radii) were performed in a single grain since grain orientation was demonstrated to have insignificant effect on the pop-in

behavior of this alloy[13]. All the indentations were conducted in load-controlled mode with a constant loading rate.

5.2 Results: p-h curves at various tip radius

Representative P-h curves for various radii are shown in Figure 42 and displacement burst is clearly observed in each curve. The pop-in size, which is defined as Δh in Figure 42, is evidently dependent upon the tip radius-it increases with the tip radius. The average pop-in sizes, in ascending order of the tip radius, are measured to be 2.1±0.5, 14.3±2.5, 23.6±2.8, 27.6±2.2, 27.4±5.5, 33.1±6 and 32±8.7nm respectively and are plotted in Figure 43 as a function of tip radius. The data can be divided into two distinct regions (Region I and Region II) as marked. In Region I, Δh increases linearly with the tip radius. As the indenter tip radius gain over about 700nm, Δh saturates and becomes essentially a constant (Region II)

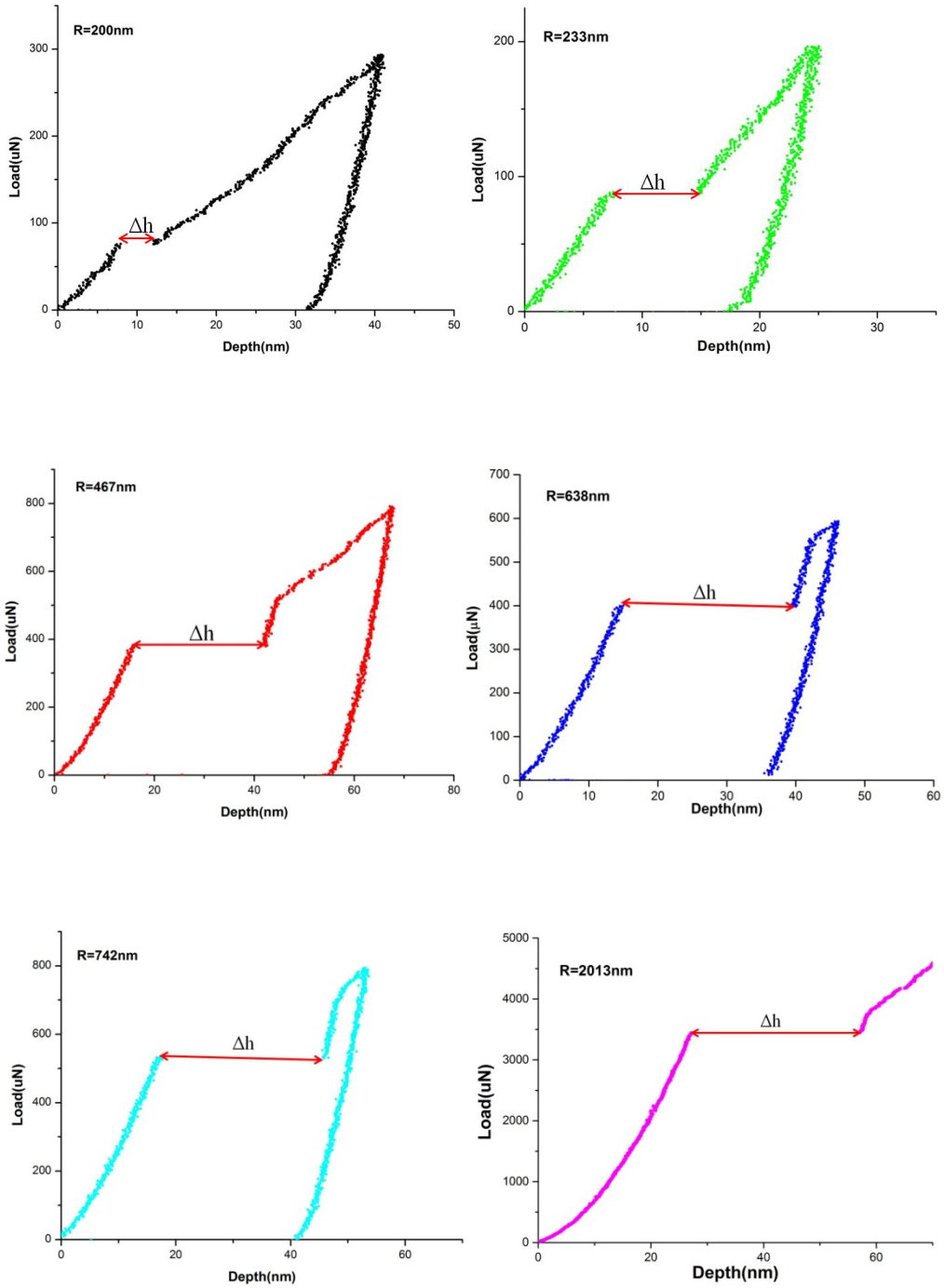

Figure 42 Representative load-displacement curves at (a) R=200nm, (b). R=233nm, (c) R=467nm, (d) R=638nm, (e) R=743nm and (f) R=2013nm

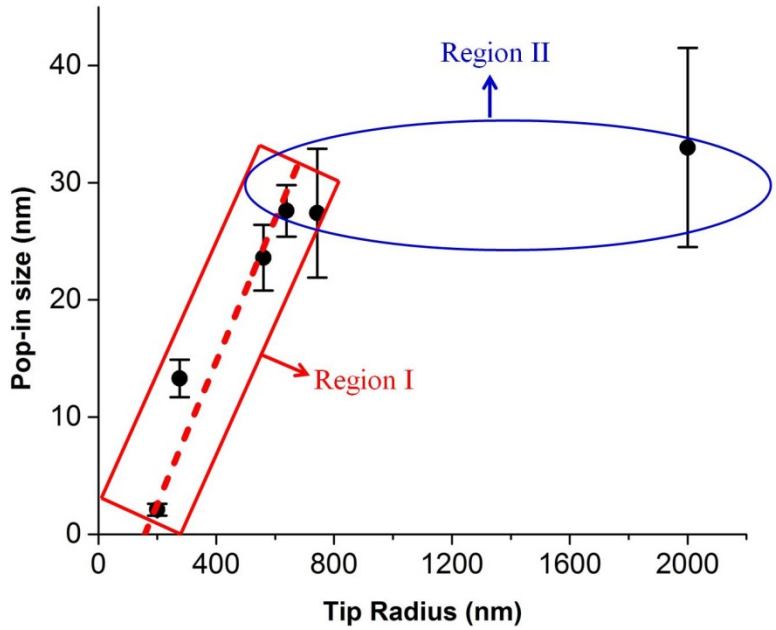

Figure 43 The pop-in size shows two different trending as indicated by Region I and Region II. In Region I, the size increases linearly with tip radius, while in Region II, the size approaches a plateau.

It is also noted that the extrapolation of the linear fitting curve in Region I intercepts the x-axis at a tip radius of about 100nm. This result suggests that, at a tip radius less than 100nm, the pop-in size is expected to vanish, i.e., Δh = 0. To validate this projection, a series of indentations with a 50nm tip were performed on the current FeCoCrNiMn sample and p-h curves are shown in Figure 44. Despite a sharp transition occurring at about 5 nm, the displacement burst no longer appears. However, the initial elastic p-h curve prior to the transition point can still be well fitted by the Hertzian equation $P = \frac{4}{3} E_r R^{1/2} h^{3/2}$, indicating the transition point is indeed a "pop-in" event marking the transition from elasticity to plasticity, only with the absence of a sudden forward displacement.

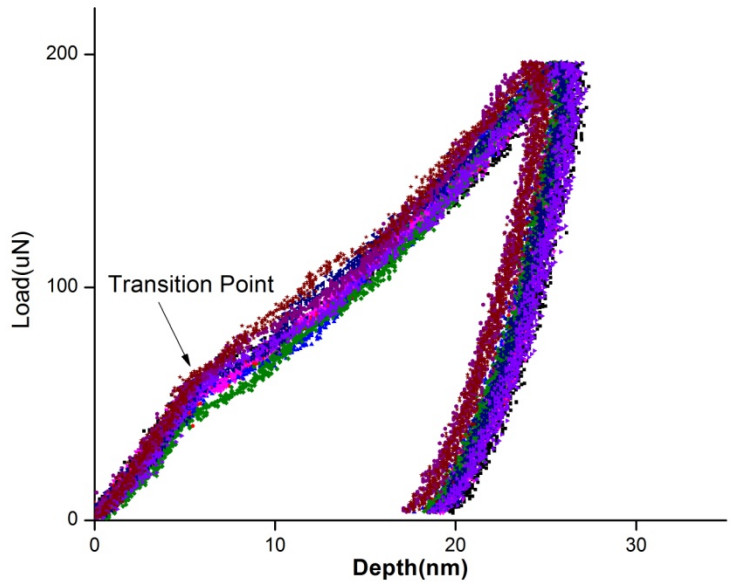

Figure 44 the indentation response under a sharp tip with a nominal radius of 50nm

5.3 Discussion

5.3.1 Pop-in size linearly scaling with tip radius between 200-700nm

According to the transition-state theory[105, 106], the nucleation rate at which a critical event (for example, formation of the critical nucleus) occurs is governed by a stress-biased equation, namely,

$$n_c = n_o v \exp(-\frac{H - \sigma V}{RT}) \tag{5.1}$$

where n_c is the number of critical nucleation nucleus formed per second, n_o is the available nucleation sites in the stressed volume, v the attempting frequency factor on the order of Debye frequency, H is the enthalpy, σ is the applied stress, and V is the activation volume. In previous studies [13, 55], it was found that dislocation nucleation was associated with point-like defects. The number of available vacancy sites, n_o, can be estimated as follows.

The equilibrium vacancy concentration at room temperature is assumed to be 10^{-6}. When a sample is indented, the stress-affected volume underneath the indenter is scaled with the contact radius s by πa^3[55]. Therefore n_o can be expressed as:

$$n_o = 4(\frac{\pi a^3}{a_o^3}) \cdot 10^{-6} \tag{5.2}$$

where a_0 is the lattice constant, 4 represents the number of atoms in a FCC unit cell, and $4(\pi a^3 / a_o^3)$ includes all atom sites in the stressed volume. According to the Hertzian theory[72], the contact radius is correlated with tip radius via

$$a = \sqrt{h \cdot R} \tag{5.3}$$

h is the pop-in depth and R the tip radius. h and R are also related through the well-known Hertzian equation:

$$P = \frac{4}{3} E_r R^{1/2} h^{3/2} \tag{5.4}$$

P is the pop-in load and E_r is the reduced modulus of the indenter and sample. Insert equation (5.3) and (5.4) into equation(5.2), we readily have

$$n_o = 3\pi \cdot 10^{-6} \cdot \frac{P}{E_r a_o^3} \cdot R \tag{5.5}$$

which clearly shows that the available nucleation sites are linearly dependent upon the tip radius R, consistent with the data shown in Figure 43. This strongly suggests that the widening in pop-in gap is associated with the increase in stressed volume under an indenter; a larger tip radius produces a larger stressed volume.

5.3.2 The vanish of pop-in at extremely small radius below 100nm

However equation (5.5) can't justify what we have observed in Figure 44 and if it could the radius must become 0 when there is no visible pop-in which contradicts the observation that the gap disappeared at a radii of 50nm. A possible explanation would be the dislocation nucleation location transitioned from inside the highly stressed zone to

contact surface between indenter and sample as the zone volume is too small to form a critical loop from within as discussed below.

Assume the nucleation is occurring within the region that takes the value above 90% of the maximum shear stress[138], this would result to volume resembling an elliptical region with a major axis of 0.6a and a minor axis of 0.5a (a is the contact radius). For tip radius of 50nm, the contact radius, a, as defined in equation 3 can be calculated with the mean value of the pop-in depth read off from Figure 44 and it is 16nm, so the major axis is 9.6nm long. The zone is schematically shown in

Figure 45. While the critical loop radius, r_c, is related to the maximum shear stress according to the following equation[115]:

$$r_c = \frac{\mu b}{2\tau_{\max}} \tag{5.6}$$

As calculated before, τ_{max} acting on the gliding plane is $\mu/12.5$ (the mean value) and substituting this value into above, the critical loop radius is found to be 6b (b=2.55nm), which is larger than the major axis of zone volume and thus the zone size is insufficient for nucleating a loop with the critical radius.

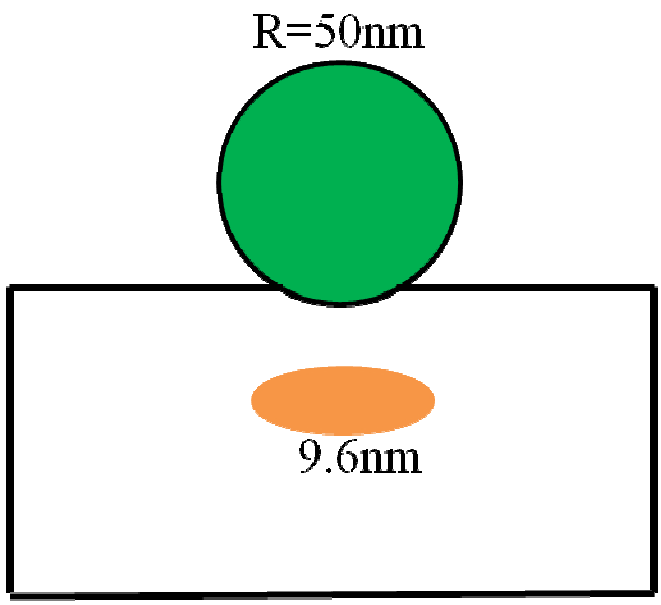

Figure 45 Schematic illustration of the size of the highly stress zone (~90% τ_{max}) for the 50nm tip, which is smaller than the critical radius, r_c(~6b=15nm), corresponding to the maximum shear stress.

On the other hand, as depth at the transition point in Figure 44 located at 5nm which is immediately close to the surface, the dislocation nucleation at the surface may become a likely alternative. There are quite a few reports [139-142] proposing that the surface dislocation nucleation is much easier in opposed to the bulk when the sample is reduced to a certain size such as in micro-pillar. The critical stress and energy barrier is much lower than what would be required within. In addition, temperature facilitates surface nucleation. Zhu T *et al*[142] suggested the nucleation stress drops by 70% as T increases from zero to room temperature.

The out of plane stress at the contact surface under spherical indenter is comparable to the maximum shear stress[143], which is schematically shown below (Figure 46), the stress at the perimeter of the contact (r=a) is about one fourth of the τ_{max} which provides the necessary stress level for dislocation nucleation. Furthermore, slip bands in V shape (Figure 47) around the impression were found when we examined the surface after micro-hardness testing. Their presence in large number indicates the possibility that

dislocation nucleates at the surface, although we don't know yet these slip bands are propagating through inside to the surface or directly nucleated at the surface.

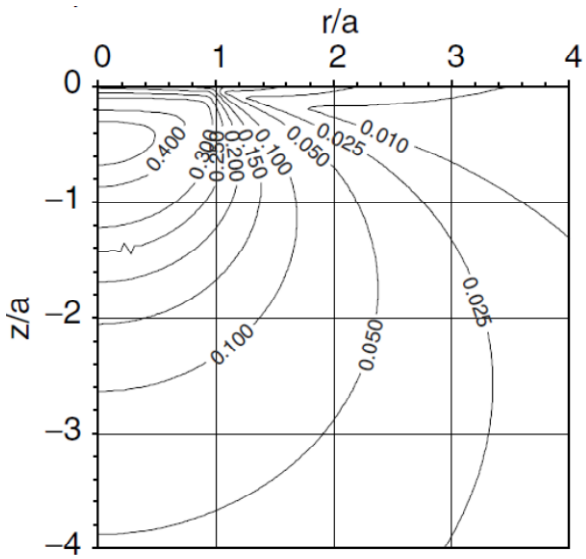

Figure 46 Maximum shear stress (τ_{max}) contours of equal stress for spherical indenter calculated for Poisson's ratio v = 0.26. Distances r and z normalized to the contact radius, a, and stress expressed in terms of the mean contact pressure p_m[143]

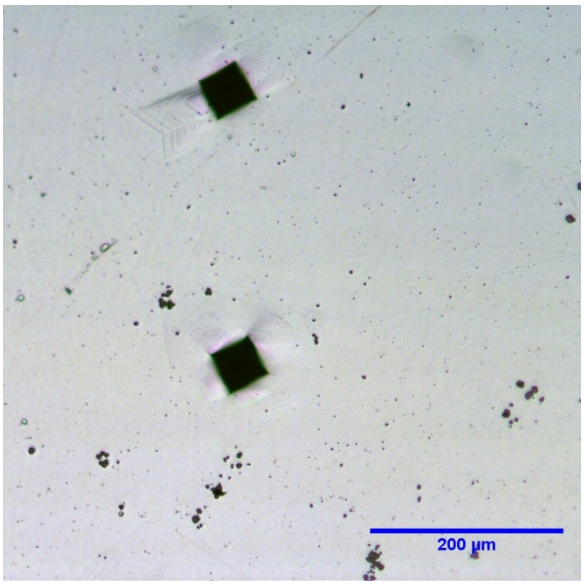

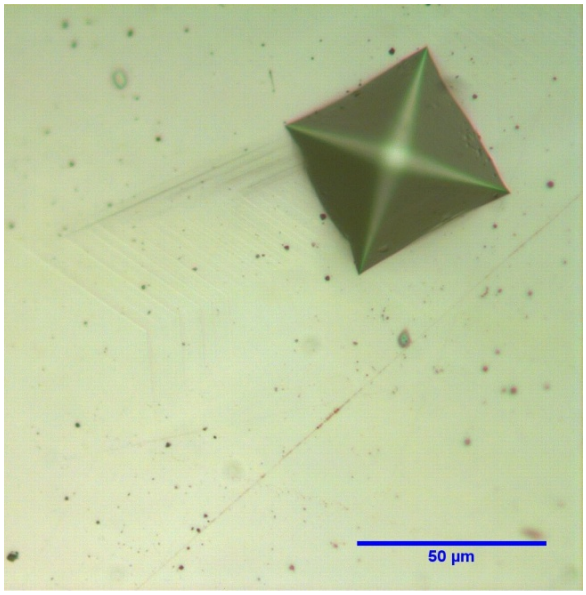

Figure 47(a) The impression of micro-hardness testing for HEA at (a) magnification 100 and (b) magnification 400. The V shape slip bands are clearly seen in both micrographs

5.3.3 Pop-in size saturating for tip radius above 700nm

When the tip radius increases to the order of hundreds of nanometers, the pop-in still occurred at shallow depth (below 20nm) as indicated in Figure 42. Therefore, the image

force becomes vital, which is the pulling force experienced by the dislocation in the near presence of a free surface. The force, for example, exerted on an edge dislocation near the free surface is expressed as [125]

$$F = \frac{\mu b^2}{4\pi(1-v)}\frac{1}{d} \tag{5.7}$$

where μ is the shear modulus, b the burgers vector, v the Poisson ratio and d the distance from the dislocation line to the free surface.

The corresponding stress acting on the dislocation line is, therefore,

$$\tau_{\max} = F / b = \frac{\mu b}{4\pi(1-v)}\frac{1}{d} \tag{5.8}$$

It is known that the stress enable to moving a dislocation within the crystal is usually on the order of $\mu/1000$ or even smaller when there is no other dislocation present[144]. This driving stress can be provided by τ_{image} if the distance, d, is adjacent enough to the surface. By taking τ_{image} equal to $\mu/1000$, we define a working distance of the image force, which is found to be 29nm, of the order of pop-in occurring depth.

So far we have described two terms which show different length scales: the nucleation volume proportional to the tip radius; the working distance of the image force, an intrinsic length scale determined only by material property. Each length scale dominates in different tip radius range, which results to the observation in Figure 43. Figure 48 illustrates how. For the pop-in occurring within the working distance when the tip radius is small, all the dislocations nucleated is able to be drawn out by τ_{image} to the free surface, and thus the size is dominated by and grows with the tip radius, which is characterized by Region I; for the pop-in beneath when the tip radius exceeding a certain size, the cut-off radius, τ_{image} can only aid to set a portion of nucleated dislocations that are within the reach of the working distance to the free surface, as a result the pop-in size forms a plateau, Region II.

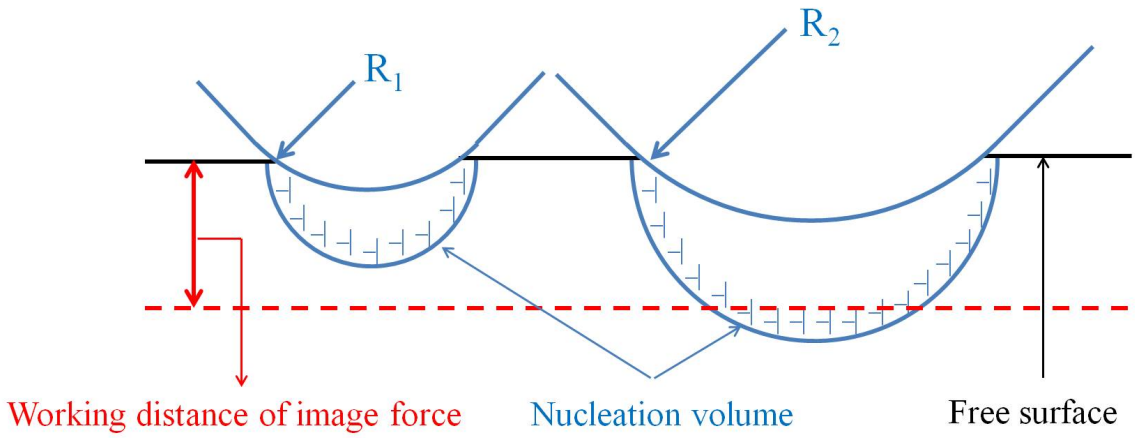

Figure 48 The graphical illustration of comparison between two competing length scales- the working distance of image force versus the nucleating volume proportional to the tip radius

The cut-off radius can be estimated by equating the contact radius, a, with the working distance, d.

$$a = \sqrt{h \cdot R} = d \tag{5.9}$$

So the cut-off radius is derived:

$$R_{cut-off} = \frac{d^2}{h} \tag{5.10}$$

With the knowledge of d and pop-in depth h, the $R_{cut\text{-}off}$ is found to be around 100nm which is much smaller than 700nm, the region transition radius in Figure 43. This indicates the assuming stress to move dislocation μ/1000 is overestimated by a factor of 3 according to equation (5.7) and(5.9).

It is worth noting that this model wouldn't apply when the tip radius is large enough that pre-existing dislocations would be encountered during indentation[61, 138]. In addition, our data show the pop-in size approaches a constant with tip radius over 700nm,

but it doesn't mean, in a strict sense, as the portion of the volume above the working distance also scales with the radius.

5.4 Conclusion

In summary, we have performed nanoindentation on a polycrystalline high entropy alloy FeCoCrNiMn using indentation tips with 7 different radii. The pop-in size dependence of the tip radius has shown two distinct regions. For small tip radii, the pop-in size increase linearly with the radius. When the radius is above about 700 nm, the pop-in size saturates. The rationale behind this observation comes from two competing mechanism-one is image force and the other is nucleating volume- that associated with two different length scaling. The image force has an intrinsic working distance linked with the yield stress of the material; the nucleating volume, on the other hand, is an extrinsic variable proportional to the radius. However, the image force is the driving force for transporting dislocations to the free surface. Therefore, when the nucleating volume is contained within the working distance of image force, the pop-in size will be dominated by the tip radius as the image force in this tip radius range is fully capable of moving the dislocations out. When the tip radius becoming larger than the cut-off radius, the portion of dislocations nucleated beneath the working distance are unable to driven to free surface by the image force and thus the pop-in size reaches a plateau.

6 Deformation mechanism at elevated temperatures investigated using stress relaxation

6.1 Introduction and experimental setup

As a new class of alloy and a promising candidate for structural applications, high-entropy alloys (HEAs), comprised of 5 or more equiatomic metallic elements in contrast to traditional alloys with one or two main elements serving as base, are receiving intensive interest in uncovering its unique mechanical properties coming with this new philosophy of design[12, 33, 145-147]. HEAs have been predicted and reported to have excellent high temperature mechanical properties[8, 33], however, the underlying deformation mechanism has seldom been explored.

As an extension to the investigation of deformation mechanism at small volume (Chapter 3, 4 and 5), in this chapter, we employ the transient testing technique-stress relaxation [75, 77, 148, 149] to study the plastic flow in global deformation. The activation volume and activation energy will be extracted from tests at elevated temperatures, the two parameters that would shed light on the rate-controlling process for thermally-activated deformation [55, 80, 81].

Dog-bone samples were prepared and then annealed and recrystallized at 900C for 2hrs before testing. The final microstructure (Figure 49) was examined in SEM and showed a grain size about 60um as well as a large amount of annealing twins.

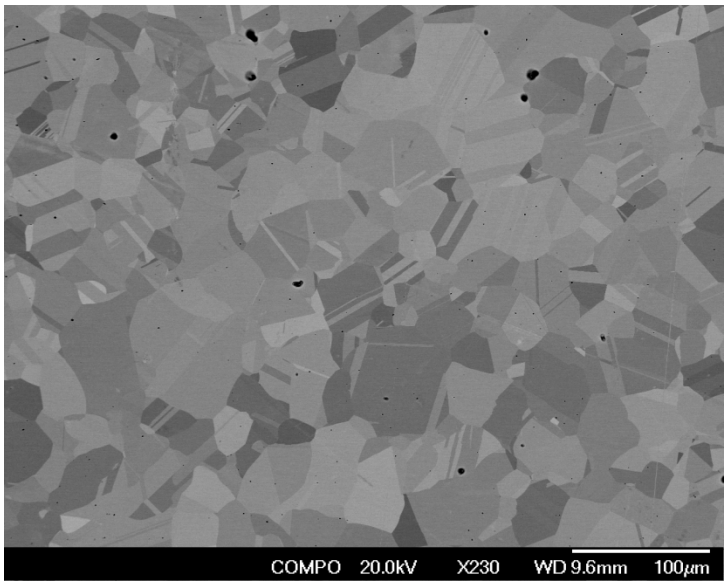

Figure 49 The microstructure annealed at 900C for 2hrs revealed a homogenous and equiaxed structure with grain size around 60μm

The whole frame for high-temperature tests was enclosed within a cylindrical furnace and the temperature was controlled with three digital monitors that connect to three thermocouples located at the upper, middle and lower end of the furnace. Three high temperatures were intended-600, 700 and 800˚C and the RT was also carried out for comparison. The tests were conducted only after the temperature on three monitors equals to the set temperature and was stabilized for 10 minutes. Various strains (0.04, 0.06, 0.08, 0.1 and 0.12) along the plastic deformation were conducted relaxation and the time lasted 240s while the load was recorded.

6.2 Activation volume and activation energy

An overview of the relaxation across tested temperatures is shown in Figure 50 with an engineering stress-strain plot. The higher the temperature, the more stress was relaxed at equal strain; and the reduction at RT is much smaller than that at higher temperatures. There is, however, a universal trending that as the plastic deformation increased the amount of load drop decreased and approached to a constant at large strains. It is also

worth noting at the first stress relaxation at 800˚C, the load was totally relaxed, i.e., the recorded load at the end of the test went to zero.

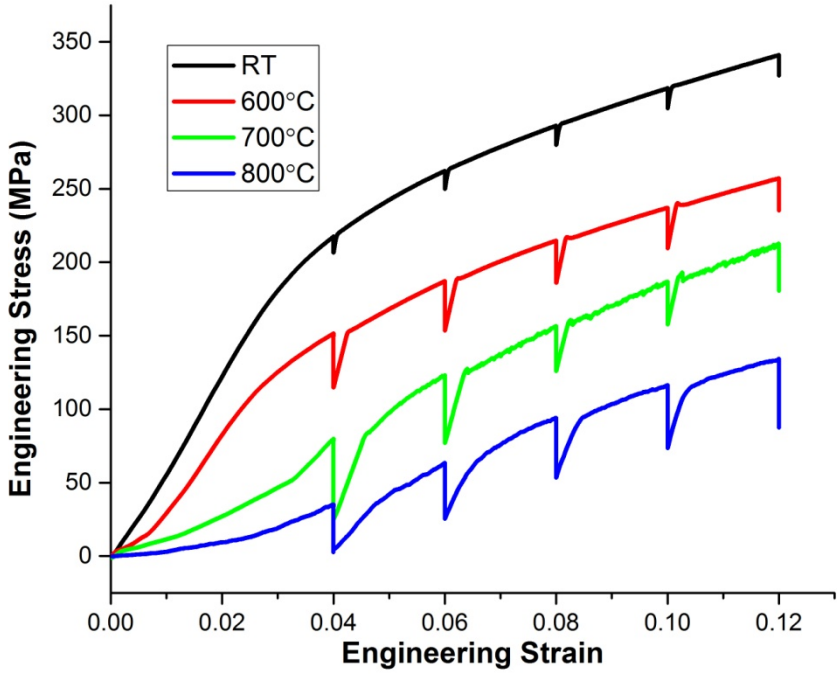

Figure 50 An overview of stress relaxation at different stages of plastic deformation over tested temperatures. The stress reduction increased with temperature and decreased with plastic deformation

The percentage reduction of stress at 0.04 engineering strain as a function of time, which is the ratio of the stress difference between instant and initial stress to the initial stress, is presented in

Figure 51 for four temperatures. All the stress decay curves obey the following logarithmic relationship:

$$\Delta\tau = \frac{kT}{V}\ln(1 + t / C_r) \tag{6.1}$$

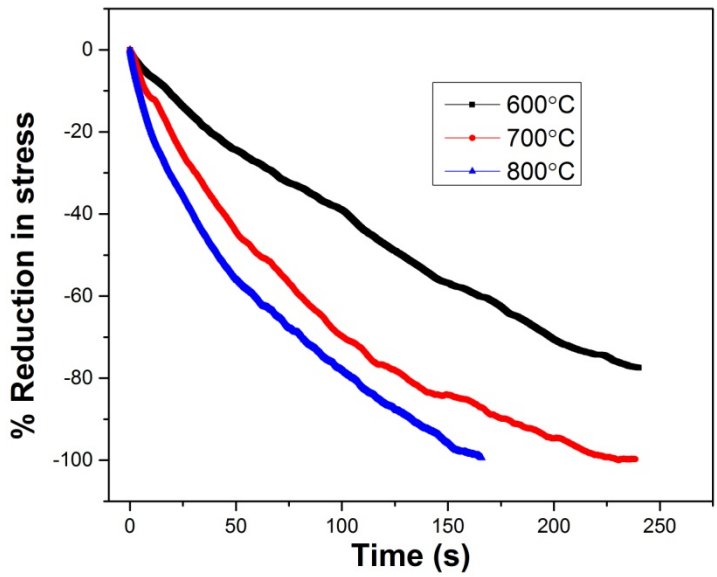

Figure 51 Percentage of reduction in stress as a function of time for 600, 700 and 800˚C

Where t is the time variable, C_r is the time constant, T is the testing temperature, $\Delta\tau$ is the decay of shear stress as a function of time during stress relaxation process and V is the activation volume that can be obtained by fitting to experimental data through equation(6.1). Since normal stress is directly available from experimental data, it would be convenient to relate the $\Delta\tau$ to the normal stress using Von-Mises criterion[115, 144]:

$$\Delta\tau = \Delta\sigma / \sqrt{3} \tag{6.2}$$

So equation (6.1) is rewritten as:

$$\Delta\sigma = \frac{\sqrt{3}kT}{V}\ln(1 + t / C_r) \tag{6.3}$$

However, equation (6.3) poses a problem as the temperature rises. Because the flow stress drops quickly with the temperature in our testing range, the normal stress decay taken as $\sigma-\sigma_0$ (the difference between instant and initial stress), for instance, is higher at 700˚C than is at 800˚C, which opposes the real situation due to the fact that at a 0.04 strain the stress was fully relieved at 800˚C even before the relaxation time was out while there was still stress working on the sample by the time the test was finished. To reflect

the true extent of stress relaxation, we modified equation (6.3) by normalizing it with the initial stress, which gives a new form:

$$\frac{\Delta\sigma}{\sigma_0} = \frac{\sqrt{3}kT}{\sigma_0 V}\ln(1 + t / C_r) \tag{6.4}$$

This new equation is more physically sensible because it clearly shows that the extent to which the stress relaxed depends on the competition between the available thermal energy (kT) and the mechanical work (σV) provided by applied stress as well as the duration (t) of stress relaxation.

The activation volume V by definition is written as:

$$V = \sqrt{3}kT\partial \ln \dot{\varepsilon} / \partial\sigma \tag{6.5}$$

And for stress relaxation at constant strain,

$$\partial \ln \dot{\varepsilon} = d \ln(-d\sigma / dt) \tag{6.6}$$

where $d\sigma / dt$ is the stress decay rate directly available from the stress versus time data.

Therefore, we can derive V for 600, 700 and 800˚C from the plot in Figure 52 in which the excellent linear fits evidence the logarithmic nature of the stress relaxation. The V, calculated by the fitted slope multiplying $\sqrt{3}kT$, were found to be 12, 31 and $62b^3$ where b (=0.255nm) is Burgers Vector of the alloy and therefore increased with the relaxation temperature.

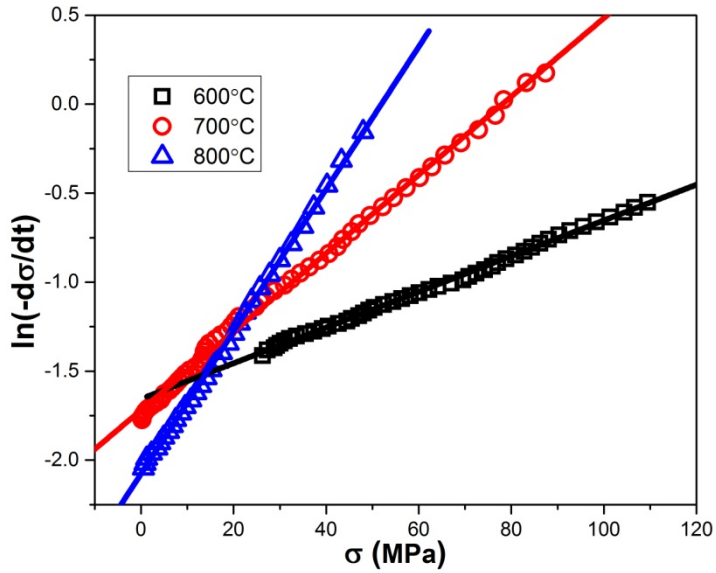

Figure 52 ln(-dσ/dt) versus stress σ plot for the first cycle of relaxation curves at 600, 700 and 800˚C. The excellent linear fits evidenced the logarithmic nature of the relaxation curves. And the increasing fitted slopes also indicate by equation (6.5) an increasing activation volume with rising temperature.

The activation enthalpy, H, can be estimated by the following equation[81]:

$$H = -TV\left(\frac{\partial \tau}{\partial T}\right)_{\dot{\varepsilon}} \tag{6.7}$$

As differential temperature tests were not available, however, the quantity $\left(\frac{\partial \tau}{\partial T}\right)_{\dot{\varepsilon}}$ can be obtained from the slope of the flow stress-temperature plot determined using a different specimen for each temperature[79]. According to the stress-displacement curves, the flow stresses at 0.4mm was 114, 87 and 54MPa for 873, 973 and 1073K, respectively, which gave a slope of -0.3MPa/K. Substituting this value along with V back into equation (6.7) gave the activation enthalpy at three temperatures as 0.18, 0.43 and 0.87eV. Thus, the according activation energy ΔG (=H-τV), by subtracting the work delivered by applied shear stress from H, equals to 0.1, 0.3 and 0.67eV.

6.3 Discussion and conlcusion

Based on the above experimental results, the mechanism of coble creep can be ruled out. For Coble creep[150], the strain rate is proportional to stress which conflicts with the plot of Figure 52 where the logarithmic of strain rate, instead of strain rate, linearly scaled with the applied stress. In addition, as activation volume for all temperatures ($12\sim62b^3$) is much larger than $1b^3$ as would be expected for dislocation climb[151], climb is also implausible. Therefore, the possibility of diffusion-controlled creep as dominant mechanism is eliminated and only dislocation creep are left to consider.

The magnitude of activation volume for conventional dislocation mechanism-intersecting forest dislocations would impose a value on the order of hundreds to thousands of b^3[79, 80]. If it were reduced to the present value, the dislocation spacing would be in the range of several tens of nanometers. The TEM image by F Otto *et al*[12] of the same alloy strained at 873K showed an interspacing many times larger. Another mechanism, cross slip, typically has a comparable activation volume yet was excluded by F Otto *et al*[12] as a possible one for this alloy at the current temperature range.

After scrutinizing through possible mechanisms with commensurate activation parameters, one seems to be a likely candidate, dislocation glide mediated by interaction with impurities (possible be C, O and etc[152]) or so called viscous dislocation glide. It matches the experimental findings in five aspects:

First, the TEM image by F Otto *et al*[12] of the sample deformed at 873K exhibited a large number of parallel (pile-up) or non-intersecting dislocations in the (111) plane within one grain (grain size=155μm). The grain is initially dislocation free and the presence of many a dislocation evidenced the gliding and possibly the emission of dislocations from the impurity-pinned dislocations.

Second, the stress displacement curves clearly showed Portevin-Le Chatelier (PLC) effect (serrated flow) which has been long associated with dynamic strain aging or the repeated pinning and de-pinning between diffusing Cottrell atmosphere (segregation of impurity atoms) and the dislocations[153-155].

Third, there is a critical temperature, 673K as reported, below which the PLC effect is deactivated and above which it is operative (not taking strain rate into account). The existence of such a critical temperature also suggests the existence of impurity atoms in that the temperature serves to stimulate their mobility to a critical level to catch up the dislocation so that the pining and de-pining can repeat[156, 157].

Fourth, the energy needed to break free of impurity atmosphere from dislocation is on the order of 0.1ev to 1eV[158, 159] which is in good agreement with the activation energy here. This strongly indicates a similar physical process is occurring in our system. The positive correlation, between activation energy and temperature and between activation volume and temperature, can also be rationalized by one fact that temperature increases the segregation along the dislocation line, which in turn increases the de-bonding energy and the pinning dislocation length.

Finally, the ductility afflicted by the PLC effect often decreases drastically, which was substantiated by stress-strain curves obtained by F. Otto for this alloy (with a grain size of 155μm) from 77 to 1073K[12]. The elongation to fracture monotonically reduced as the temperature was raised with an engineering strain of 100% to 20% at 1073K.

7 Future perspectives

The deformation behavior of annealed HEA FeCoCrMnNi on the nano-scale or the incipient plasticity is controlled by dislocation nucleation. The activation volume and energy for the nucleation were extracted from a mechanistic model and found comparable to that of point-size defects, i.e., vacancy. This leads to the conclusion that the nucleation process might be controlled by the migration of vacancy, which in turn is taken as the basic assumption for chapter 4 and 5. However, it would be experimentally difficult to validate the assumption and to answer the question as to how these defects cluster and trigger the pop-in event. Molecular dynamic simulation is worthy pursuing to shed lights on atomistic process.

The delayed incipient plasticity has its origin in the time scale introduced by the stress-assisted migration of vacancy. The time awaited to pop-in varies considerably even under an identical loading condition. The possible reasons leading to such a pattern of time distribution has not been decided yet and a proper model (also probably more complex), better be carried out in simulation, needs to be constructed incorporating both the population and distribution of vacancy beneath the indenter and the kinetics of migration.

The incipient plasticity also exhibits stressed-volume dependence, especially interesting at really small volume. With a small tip radius, the pop-in morphs into a transition point on the load-displacement curve instead of the usual burst. The possible reason I proposed is that the preferential nucleation site of dislocation transfers from within the highly stressed zone to the surface. This is because, firstly, the zone is inadequate to offer enough space for a critical nucleus and, secondly, the plasticity occurring depth is approaching to only several nanometers. Although slip bands on the surface of the micro-hardness impression was observed, it is still unsure whether those slip bands were formed by the dislocations nucleated from within and propagating to the surface or just by the dislocations nucleated right at the surface. Again, a molecular dynamic simulation would be highly appropriate to verify if there is such a transition.

As for the global deformation at elevated temperatures, the serration flow and the activation volume and energy suggested the important role of impurity atoms. However, it is still not determined what kind of impurity is at play. Also of significance is their effect on the yielding strength and ductility of the alloy at different temperatures and strain rates, and, specifically, effect on thermal stress (i.e., effective stress) component of yield stress as a function of temperature.

References

[1]Cantor B, *et al.* Materials Science and Engineering: A 2004;375:213.
[2]Tsai MH Entropy 2013;15:5338.
[3]Yeh JW Annales De Chimie-Science Des Materiaux 2006;31:633.
[4]Yeh JW Jom 2013;65:1759.
[5]Yeh JW, *et al.* Advanced Engineering Materials 2004;6:299.
[6]YEH J-W, *et al.* High-entropy alloys : A new era of exploitation. Aedermannsdorf, SUISSE: Trans Tech, 2007.
[7]Zhang Y, *et al.* Prog. Mater. Sci. 2014;61:1.
[8]Senkov ON, *et al.* Intermetallics 2010;18:1758.
[9]Liaw PK, *et al.* Metall. Mater. Trans. A-Phys. Metall. Mater. Sci. 2014;45A:179.
[10]Miracle DB, *et al.* Entropy 2014;16:494.
[11]Gao MC, Alman DE Entropy 2013;15:4504.
[12]Otto F, *et al.* Acta Materialia 2013;61:5743.
[13]Zhu C, *et al.* Acta Materialia 2013;61:2993.
[14]Liu WH, *et al.* Scripta Materialia 2013;68:526.
[15]Wu Z, *et al.* Intermetallics 2014;46:131.
[16]Bhattacharjee PP, *et al.* Journal of Alloys and Compounds 2014;587:544.
[17]Ivchenko MV, *et al.* Physics of Metals and Metallography 2013;114:514.
[18]Ivchenko MV, *et al.* Physics of Metals and Metallography 2013;114:503.
[19]Kuznetsov AV, *et al.* Materials Science and Engineering a-Structural Materials Properties Microstructure and Processing 2012;533:107.
[20]Kuznetsov AV, *et al.* Superplasticity of AlCoCrCuFeNi High Entropy Alloy. In: Bernhart G, editor. Superplasticity in Advanced Materials, vol. 735. 2013. p.146.
[21]Singh S, *et al.* Acta Materialia 2011;59:182.
[22]Welk BA, *et al.* Ultramicroscopy 2013;134:193.
[23]Wen LH, *et al.* Intermetallics 2009;17:266.
[24]Guo S, *et al.* Intermetallics 2013;41:96.
[25]Guo S, Liu C Progress in Natural Science: Materials International 2011;21:433.
[26]Guo S, *et al.* Journal of applied physics 2011;109:103505.
[27]Pi JH, Pan Y Rare Metal Materials and Engineering 2013;42:232.
[28]Yang X, Zhang Y Materials Chemistry and Physics 2012;132:233.
[29]Zhang Y, *et al.* Advanced Engineering Materials 2008;10:534.
[30]Otto F, *et al.* Acta Materialia 2013;61:2628.
[31]Lucas M, *et al.* Applied Physics Letters 2012;100:251907.
[32]Senkov ON, *et al.* Journal of Alloys and Compounds 2011;509:6043.
[33]Senkov O, *et al.* Intermetallics 2011;19:698.
[34]Lin CM, Tsai HL Materials Chemistry and Physics 2011;128:50.
[35]Tsai CW, *et al.* Journal of Alloys and Compounds 2009;486:427.
[36]Zhang KB, *et al.* Journal of Alloys and Compounds 2010;502:295.
[37]Tong CJ, *et al.* Metall. Mater. Trans. A-Phys. Metall. Mater. Sci. 2005;36A:1263.
[38]Tong CJ, *et al.* Metall. Mater. Trans. A-Phys. Metall. Mater. Sci. 2005;36A:881.
[39]He JY, *et al.* Acta Materialia 2014;62:105.
[40]Li BS, *et al.* Materials Science and Engineering a-Structural Materials Properties Microstructure and Processing 2008;498:482.
[41]Tung CC, *et al.* Materials Letters 2007;61:1.
[42]Wang WR, *et al.* Intermetallics 2012;26:44.

[43]Zhang Y, *et al.* Annales De Chimie-Science Des Materiaux 2006;31:699.
[44]Arzt E Acta Materialia 1998;46:5611.
[45]Chokshi A, *et al.* Scripta Metallurgica 1989;23:1679.
[46]Hansen N Scripta Materialia 2004;51:801.
[47]Nieh TG, Wadsworth J Scripta Metallurgica Et Materialia 1991;25:955.
[48]Beck PA, *et al.* Trans. Am. Inst. Min. Metall. Eng 1948;175:372.
[49]Senkov ON, *et al.* Intermetallics 2011;19:698.
[50]Schuh CA Materials Today 2006;9:32.
[51]Lund AC, *et al.* Applied Physics Letters 2004;85:1362.
[52]Minor AM, *et al.* J. Mater. Res. 2004;19:176.
[53]Schuh CA, Lund AC J. Mater. Res. 2004;19:2152.
[54]Tadmor EB, *et al.* J. Mater. Res. 1999;14:2233.
[55]Mason JK, *et al.* Physical Review B 2006;73:054102.
[56]Schuh CA, *et al.* Nature Materials 2005;4:617.
[57]Corcoran S, *et al.* Physical Review B 1997;55:R16057.
[58]Page TF, *et al.* J. Mater. Res. 1992;7:450.
[59]Leipner H, *et al.* Physica B: Condensed Matter 2001;308:446.
[60]Kucheyev S, *et al.* Applied Physics Letters 2002;80:956.
[61]Shim S, *et al.* Scripta Materialia 2008;59:1095.
[62]Kelchner CL, *et al.* Physical Review B 1998;58:11085.
[63]Kiely JD, Houston JE Physical Review B 1998;57:12588.
[64]Lorenz D, *et al.* Physical Review B 2003;67:172101.
[65]Page TF, *et al.* Journal of Materials Research 1992;7:450.
[66]Wang W, *et al.* Acta Materialia 2003;51:6169.
[67]Li J, *et al.* Nature 2002;418:307.
[68]Van Vliet KJ, *et al.* Physical Review B 2003;67:104105.
[69]Li J MRS Bull 2007;32:151.
[70]Minor AM, *et al.* Nature materials 2006;5:697.
[71]Minor A, *et al.* J. Mater. Res. 2004;19:176.
[72]Hertz H. Miscellaneous papers: Macmillan, 1896.
[73]Fischer-Cripps AC. Nanoindentation: Springer, 2011.
[74]Caillard D, Martin JL. Thermally activated mechanisms in crystal plasticity: Elsevier Science, 2003.
[75]Guiu F, Pratt P physica status solidi (b) 1964;6:111.
[76]Gibbs G Philosophical Magazine 1966;13:317.
[77]Lee D, Hart E Metallurgical Transactions 1971;2:1245.
[78]Martin J, *et al.* Materials Science and Engineering: A 2002;322:118.
[79]Evans A, Rawlings R physica status solidi (b) 1969;34:9.
[80]Wei Q, *et al.* Materials Science and Engineering: A 2004;381:71.
[81]Schoeck G physica status solidi (b) 1965;8:499.
[82]Conrad H, Wiedersich H Acta Metallurgica 1960;8:128.
[83]Wang Z, *et al.* Scripta Materialia 2011;65:469.
[84]Schuh CA, Lund AC Journal of Materials Research 2004;19:2152.
[85]Bei H, *et al.* Physical Review Letters 2004;93:125504.
[86]Wang L, *et al.* Scripta Materialia 2011;65:759.
[87]Song SX, *et al.* Intermetallics 2010;18:702.

[88]Hertz H Macmilan, London 1896.
[89]Oliver WC, Pharr GM J. Mater. Res. 1992;7:1564.
[90]Johnson KL. Contact mechanics: Cambridge university press, 1987.
[91]Bahr DF*, et al.* Acta Materialia 1998;46:3605.
[92]Gerberich WW*, et al.* Acta Materialia 1996;44:3585.
[93]Gerberich WW*, et al.* Acta Metallurgica et Materialia 1995;43:1569.
[94]Lilleodden ET*, et al.* Journal of the Mechanics and Physics of Solids 2003;51:901.
[95]Gouldstone A*, et al.* Nature 2001;411:656.
[96]Zhu T*, et al.* Journal of the Mechanics and Physics of Solids 2004;52:691.
[97]Bahr DF*, et al.* J. Mater. Res. 1999;14:2269.
[98]Chiu YL, Ngan AHW Acta Materialia 2002;50:1599.
[99]Michalske TA, Houston JE Acta Materialia 1998;46:391.
[100]Xu G, Argon AS Philosophical Magazine Letters 2000;80:605.
[101]Hirth JP, Lothe J John Wiley and Sons, Inc., 1982 1982:857.
[102]Seitz F Physical Review 1950;79:890.
[103]Davis T, Hirth J Journal of Applied Physics 1966;37:2112.
[104]Jackson K Philosophical Magazine 1962;7:1117.
[105]Vineyard GH Journal of Physics and Chemistry of Solids 1957;3:121.
[106]Hänggi P*, et al.* Reviews of Modern Physics 1990;62:251.
[107]Callister WD, Rethwisch DG. Fundamentals of materials science and engineering: an integrated approach: John Wiley & Sons, 2012.
[108]Balluffi R Journal of Nuclear Materials 1978;69:240.
[109]Yeh J-W*, et al.* Metallurgical and Materials Transactions A 2004;35:2533.
[110]Wo P*, et al.* J. Mater. Res. 2005;20:489.
[111]Bahr D*, et al.* J. Mater. Res. 1999;14:2269.
[112]Zuo L*, et al.* Physical Review Letters 2005;94:095501.
[113]Ngan A, Wo P Philosophical Magazine 2006;86:1287.
[114]Li W, Warren R Acta metallurgica et materialia 1993;41:3065.
[115]Dieter GE, Bacon D. Mechanical metallurgy: McGraw-Hill New York, 1986.
[116]Hirsch P*, et al.* Philosophical Magazine 1958;3:897.
[117]Silcox J, Whelan M Philosophical Magazine 1960;5:1.
[118]Kiritani M Journal of the Physical Society of Japan 1964;19:618.
[119]Makin M*, et al.* Philosophical Magazine 1962;7:285.
[120]Westmacott K*, et al.* Philosophical Magazine 1962;7:2035.
[121]Heald P, Speight M Philosophical Magazine 1974;29:1075.
[122]Kiritani M*, et al.* Journal of the Physical Society of Japan 1975;38:1677.
[123]Northwood D*, et al.* Journal of Nuclear Materials 1976;61:123.
[124]Ward A, Fisher S Journal of Nuclear Materials 1989;166:227.
[125]Hull D, Bacon DJ. Introduction to dislocations: Pergamon Press Oxford, 1984.
[126]Li WB*, et al.* Acta metallurgica et materialia 1991;39:3099.
[127]Syed Asif S, Pethica J Philosophical Magazine A 1997;76:1105.
[128]Chang L, Zhang L Materials Science and Engineering: A 2009;506:125.
[129]Shibutani Y*, et al.* Acta Materialia 2007;55:1813.
[130]Li TL*, et al.* Journal of the Mechanics and Physics of Solids 2011;59:1147.
[131]Wang W*, et al.* Acta materialia 2003;51:6169.
[132]Tsuru T, Shibutani Y Physical Review B 2007;75:035415.

[133]Schuh C, *et al.* Nature Materials 2005;4:617.
[134]Li TL, *et al.* Materials Science and Technology 2012;28:1055.
[135]Morris JR, *et al.* Physical review letters 2011;106:165502.
[136]Suresh S, *et al.* Scripta Materialia 1999;41:951.
[137]Shibutani Y, Tsuru T Key Engineering Materials 2007;340:39.
[138]Barnoush A Acta Materialia 2012;60:1268.
[139]Beltz G, Freund L physica status solidi (b) 1993;180:303.
[140]Shenoy VB, *et al.* Journal of the Mechanics and Physics of Solids 2000;48:649.
[141]Weinberger CR, Cai W Proceedings of the National Academy of Sciences 2008;105:14304.
[142]Zhu T, *et al.* Physical Review Letters 2008;100:025502.
[143]Fischer-Cripps AC, Mustafaev I. Introduction to contact mechanics: Springer, 2000.
[144]Courtney TH. Mechanical behavior of materials: Waveland Press, 2005.
[145]Tong C-J, *et al.* Metallurgical and Materials Transactions A 2005;36:1263.
[146]Zhou Y, *et al.* Applied physics letters 2007;90:181904.
[147]Varalakshmi S, *et al.* Materials Science and Engineering: A 2010;527:1027.
[148]Li JC Canadian Journal of Physics 1967;45:493.
[149]Gupta I, Li J Metallurgical Transactions 1970;1:2323.
[150]Coble R Journal of Applied Physics 1963;34:1679.
[151]Sherby O, *et al.* Journal of Applied Physics 2003;41:3961.
[152]Tang Z. Processing, Microstructures, and Mechanical Behavior of High-Entropy Alloys 2012.
[153]Wilcox B, Smith G Acta Metallurgica 1964;12:371.
[154]McCormigk P Acta Metallurgica 1972;20:351.
[155]Chihab K, *et al.* Scripta Metallurgica 1987;21:203.
[156]Cottrell A, Bilby B Proceedings of the Physical Society. Section A 1949;62:49.
[157]Van den Beukel A Physica status solidi (a) 1975;30:197.
[158]Cottrell A Philosophical Magazine 1953;44:829.
[159]Mukherjee K, *et al.* Journal of Applied Physics 2003;39:5434.

Vita

Chao Zhu was born in a small village in Hubei, China. He entered the department of materials science and engineering at the Huazhong University of Science and Technology in 2002 and received a bachelor degree in engineering in 2006. Upon finishing his undergraduate study, he was then immediately accepted into the master program at the Institute of Metals Research, Chinese Academy of Sciences and graduated in 2009. At the same year, he came to the University of Tennessee Knoxville in pursuit of his PhD study. After five years' struggle he was awarded the PhD degree in 2014.